Epitaxial ferroelectric $Hf_{0.5}Zr_{0.5}O_2$ (HZO):

Growth, Switching & Fatigue behavior

By

Zimeng Zhang

A dissertation submitted in partial satisfaction of the

requirements for the degree of

Doctor of Philosophy

In

Engineering – Materials Science and Engineering

in the

Graduate Division

of the

University of California, Berkeley

Committee in charge:

Professor Ramamoorthy Ramesh
Professor Lane W. Martin
Professor Sayeef Salahuddin

Fall 2023

Abstract

Epitaxial ferroelectric $Hf_{0.5}Zr_{0.5}O_2$ (HZO):

Growth, Switching & Fatigue behavior

By

Zimeng Zhang

Doctor of Philosophy in Engineering - Materials Science & Engineering

University of California, Berkeley

Professor Ramamoorthy Ramesh, Chair

In recent years, the escalating demand for computing has necessitated the discovery of novel materials to power the next generation of logic and memory devices. Among these materials, ferroelectric hafnia (Hafnium Zirconium Oxide or HZO) stands out as a promising candidate. This thesis delves into the multifaceted realm of thin film ferroelectric HZO, spanning from deposition processes to the analysis of switching and fatigue behaviors. The study utilizes two distinct material systems: HZO/pyrochlore for fundamental investigations and HZO/$La_{0.67}Sr_{0.33}MnO_3$ for practical applications, including Ferroelectric Tunnel Junctions (FTJ), enabling a comprehensive exploration.

Chapter 3 focuses on epitaxial HZO with pyrochlore electrodes, revealing strain's role in stabilizing HZO's polar orthorhombic phase. It notes the high switching field in pure epitaxial HZO, hints at an order-disorder phase transition, and introduces a single-crystal ferroelectric epitaxial HZO system. Chapter 4 delves into the fatigue bahavior of hafnia, showing oxygen intercalation and defect chemistry's impact on stabilizing the orthorhombic phase, crucial for endurance behavior. Chapter 5 highlights Tunnel Electro-Resistance effects in HZO-based Ferroelectric Tunnel Junctions and the scale-free property of ferroelectric HZO, promising for high-density memory applications. In summary, this thesis advances HZO-based ferroelectric materials' understanding, laying the groundwork for future research in advanced computing and memory systems.

Acknowledgments

Reflecting on my five-year journey at Berkeley, I am filled with immense gratitude for the steadfast support and encouragement I received, both technically and emotionally, during this challenging yet fulfilling endeavor.

First and foremost, my deepest appreciation goes to my mentor, Professor Ramamoorthy Ramesh. His expertise and guidance have been invaluable. Professor Ramesh's unwavering support and profound insights have been pivotal in navigating the intricacies of my research. His mentorship has profoundly influenced both my academic and professional development, for which I am profoundly thankful. I am also deeply grateful for the guidance and support from Prof. Lane Martin, Prof. Jie Yao, Prof. Junqiao Wu, and Prof. Sayeef Salahuddin, whose contributions have significantly enriched my journey.

My heartfelt thanks also go to my labmates and colleagues: Dr. Sujit Das, Dr. Yen-Lin Huang, Dr. Xiaoxi Huang, Dr. Megha Acharya, Dr. Eric Parsonnet, Dr. Shang-Lin Hsu, Dr. Hongrui Zhang, Dr. Bhagwati Prasad, and Dr. Vishal Thakare. Your camaraderie, collective wisdom, and shared experiences have immensely enhanced my research journey. The technical support, engaging discussions, and shared moments of both breakthroughs and challenges in the lab have been fundamental to the completion of my work.

On a more personal note, I am especially thankful to my beloved corgi, Pika. Her joyful presence and unconditional love have been a source of comfort and stress relief during the most demanding phases of my life.

Lastly, but most importantly, my profound gratitude extends to my family and friends. Your constant emotional support, patience, and faith in me have been my stronghold. Your encouragement during challenging times and celebrations in moments of achievement has been the foundation of my resilience.

This journey has been an intricate tapestry of professional advancement and personal growth, intricately woven by the support of each individual mentioned. I am eternally grateful for your invaluable presence in my life.

Table of Contents

Chapter 1

Introduction to Ferroelectric Materials and Memory Devices

1.1 Motivation: Low-energy devices for logic and memory

Over recent decades, the computing landscape has experienced a profound transformation. This change is characterized by an explosive increase in computational power, advanced data processing capabilities, and groundbreaking technological innovations. Fields like Artificial Intelligence (AI) and the Internet of Things (IoT) have not only revolutionized our daily lives but also significantly influenced sectors like industry, healthcare, and transportation. Alongside these advancements, the computational demands and resource consumption of these systems have escalated markedly. This chapter delves into the critical motivation behind the development of low-energy logic and memory devices in the context of the ever-increasing energy consumption in computing.

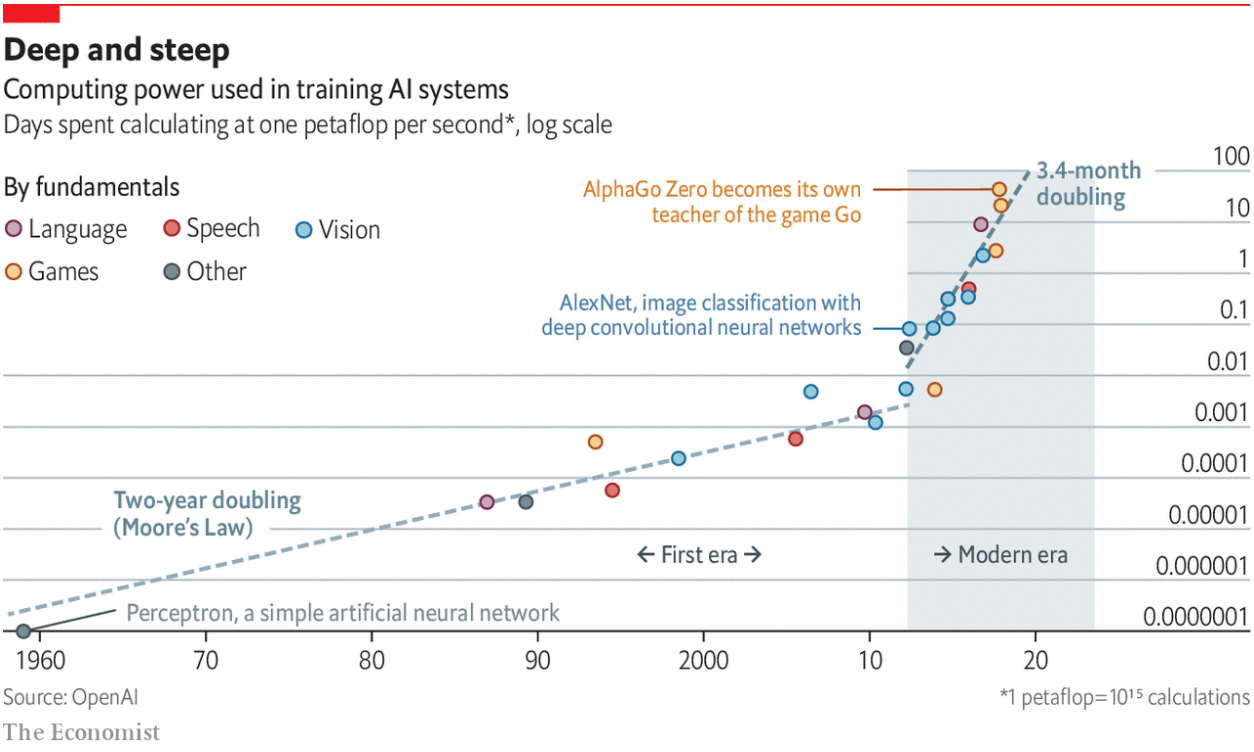

Figure 1.1. Computing power used in training AI systems. [1]

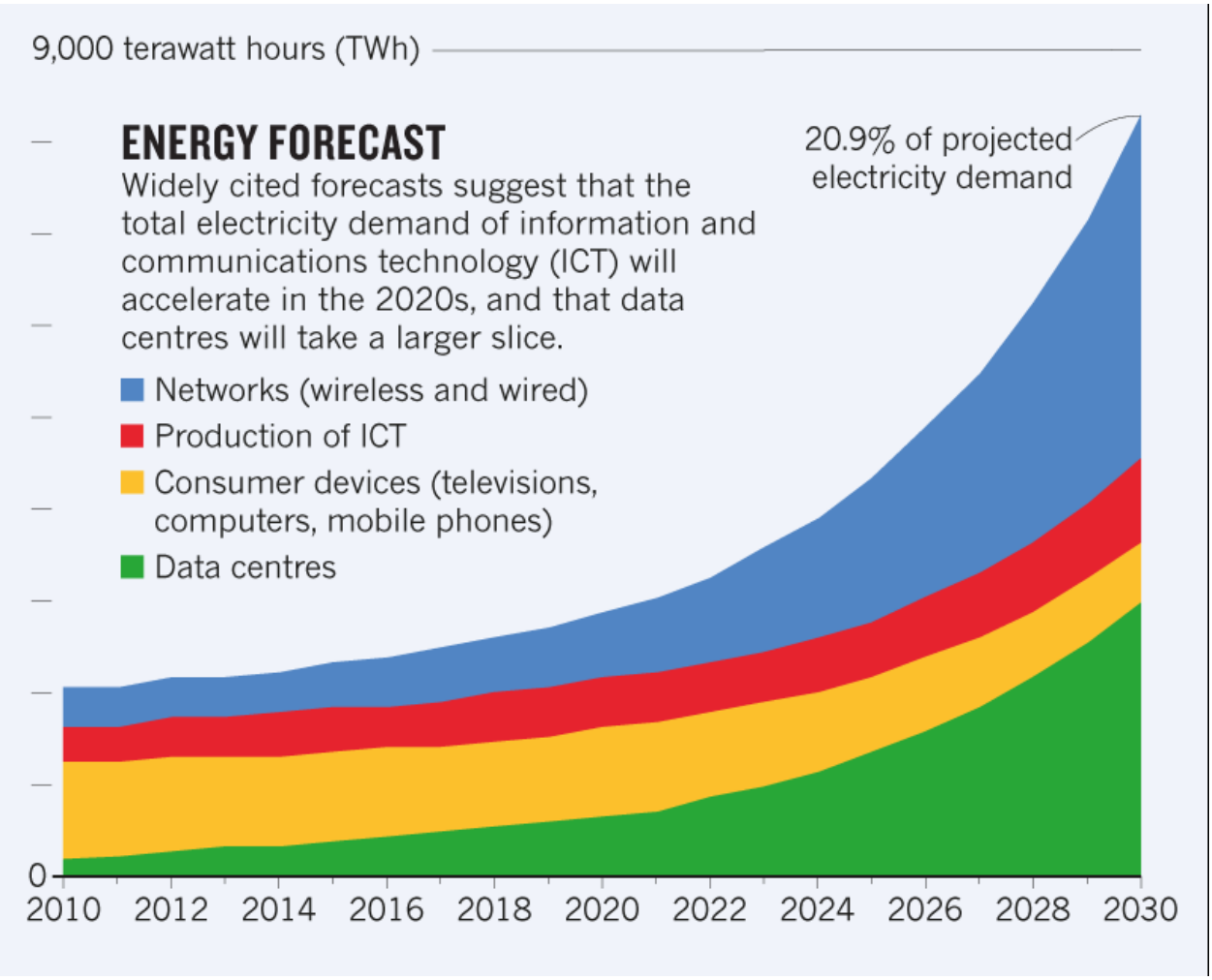

Figure 1.2. Energy consumption forecast in the information and communication technology (ICT) sector. [2]

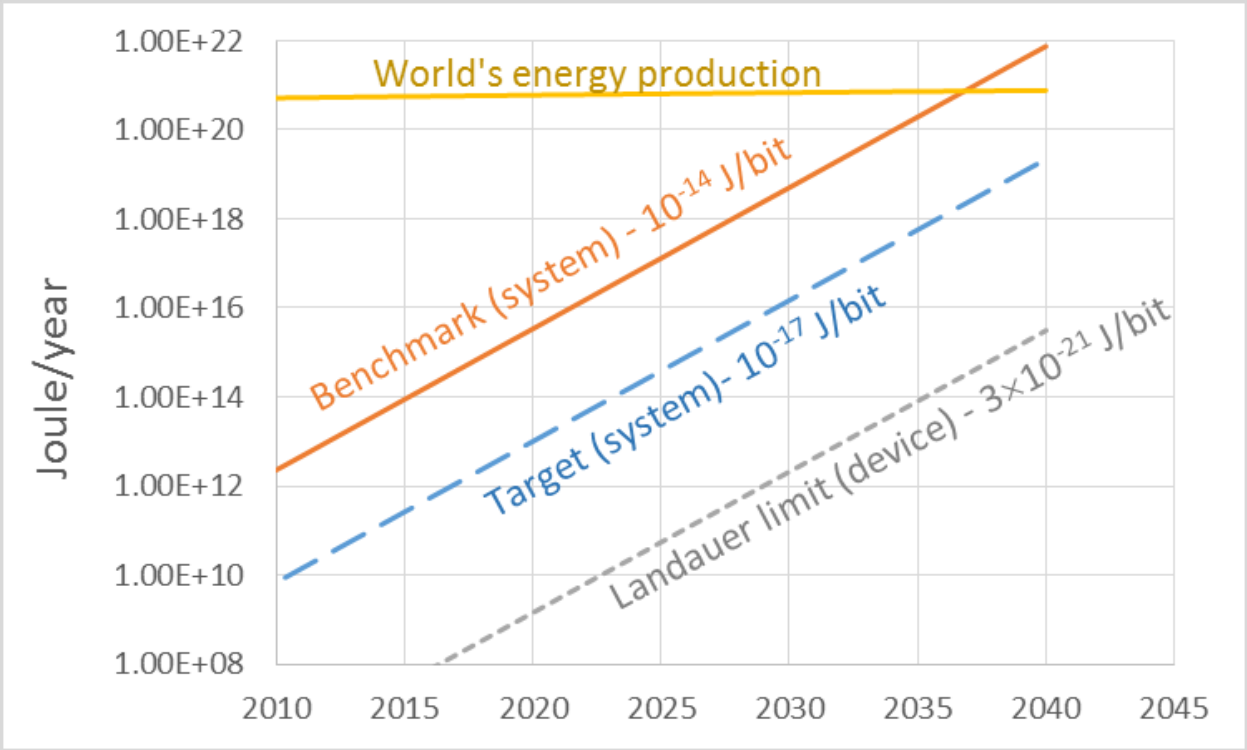

Figure 1.3. Energy consumption forecast on computing. [3]

Figure 1.1 illustrates the rising trend in computational power required for machine learning. This growth, echoing the principles of Moore's Law, is accelerating at a much faster rate, underscoring the immense resource demands for future AI development. Figure 1.2 forecasts the energy consumption in the information and communication technology (ICT) sector, projecting that by 2030, it will account for over 20% of global electricity usage, with data centers being a major contributor to this increase. Furthermore, a 2015 forecast suggested that by around 2040, computing's total energy consumption might rival the world's entire energy production (Figure 1.3).

These escalating market demands highlight the urgent need for fundamental improvements in computing systems. As Moore's Law approaches its limits due to quantum and thermal noise at the atomic level, finding alternative strategies to optimize the power-performance-area-cost (PPAC) metrics of chip systems becomes crucial. This need drives the search for new materials and technological breakthroughs to sustain growth in the semiconductor industry and the burgeoning demands for data processing.[3]

Non-volatile memory devices, exemplified by ferroelectric RAM (FeRAM) and other emerging technologies, store data even when powered off. These devices require significantly less energy than traditional dynamic random-access memory (DRAM), which constantly refreshes data. Moreover, the enduring properties of non-volatile memory are ideal for applications requiring fast, energy-efficient data access, such as mobile devices and IoT (Internet of Things) gadgets. Complementary to low-energy memory devices, low-energy logic components can revolutionize

computation. By designing processors and integrated circuits that operate at reduced voltages and exhibit minimal energy leakage, it is possible to enhance the energy efficiency of computing systems. These advancements can lead to longer battery life, reduced energy bills, and a smaller carbon footprint.

Ferroelectric materials are among the promising solutions being explored. This chapter introduces ferroelectric materials and devices, focusing particularly on hafnium oxide, a highly promising candidate. The investigation of hafnium oxide in this thesis is intended to contribute to the development of next-generation computing systems that are both energy-efficient and offer high performance.

1.2 Ferroelectric memory devices: history and mechanisms

1.2.1 Basic concepts of ferroelectrics and traditional ferroelectric materials

Ferroelectric materials are characterized by their spontaneous non-zero polarization states in the absence of an external electric field. These materials can transition between two opposite polarization states by applying a sufficiently strong external electric field. Additionally, ferroelectrics exhibit piezoelectric and pyroelectric properties, along with the ability to reverse their polarization. The polarization of ferroelectrics relies not only on the applied field but also on their history. Similar to ferromagnetic materials, the behavior of ferroelectrics can be studied using a hysteresis loop (Figure 1.4), which plots the polarization value (P) or displacement value (D) against the external electric field (E). The coercive field, also known as the switching field, refers to the electric field at which the total effective polarization value becomes zero. The remnant polarization of a ferroelectric material arises from the separation of positive and negative charge centers in the lattice, often caused by the displacement of specific ions from their charge-neutral positions. Consequently, ferroelectric materials exhibit a non-centrosymmetric nature. Out of the 230 point group symmetries available, 10 meet the criteria for ferroelectricity.

The inherent presence of spontaneous opposite polarization states can be naturally linked to binary states, 0 and 1. Thus, the proposal of implementing ferroelectric materials into logic/memory devices has been pursued since the 1950s. [4]

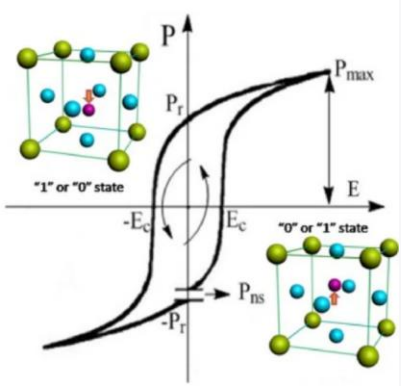

Figure 1.4. Schematics of ferroelectric hysteresis loop and the binary states

When applying ferroelectrics to memory cells, different readout mechanisms determine the types of memories. In a destructive way, or capacitor-based readout scheme, the current during the switching and non-switching process is used as the output when applying a large electric field to the memory cell. If the applied state is in line with the applied state, there will be reduced charge flow going through the circuit; however, when an opposite electric field is applied, the polarization state is switched, generating a large charge flow through the capacitor. It is important to note that this switching process also results in the destruction of the original polarization state of the memory unit. This scheme is usually used in ferroelectric random-access memories (FeRAMs)

Another readout scheme used is the non-destructive approach, which finds applications in the proposals of ferroelectric field effect transistors (FeFETs) and ferroelectric tunnel junctions (FTJs). In FeFETs, the ferroelectric materials function as the gate dielectric of the usual transistor structure. The polarization state of the ferroelectric induces a shift in the current-voltage (I-V) curve of the transistor, resulting in distinct output currents corresponding to different polarization states. In FTJs, the structure is much simplified to a capacitor. The ferroelectric material serves as the thin tunneling layer, working in conjunction with the asymmetric screening properties of the two electrodes to generate different potential barrier profiles under two polarization states. This arrangement enables the direct readout of the polarization state from the magnitude of the flowing current through the capacitor.

Among these various ferroelectric memory devices, FeRAMs have undergone extensive research and development, ultimately leading to their successful integration into real-world products available in the market. FeFETs and FTJs are relatively emerging technologies that have gained considerable interest and are currently the focus of ongoing investigations and advancements in the field of ferroelectric memory.

1.2.2 Ferroelectric random access memory (FeRAM) [5]

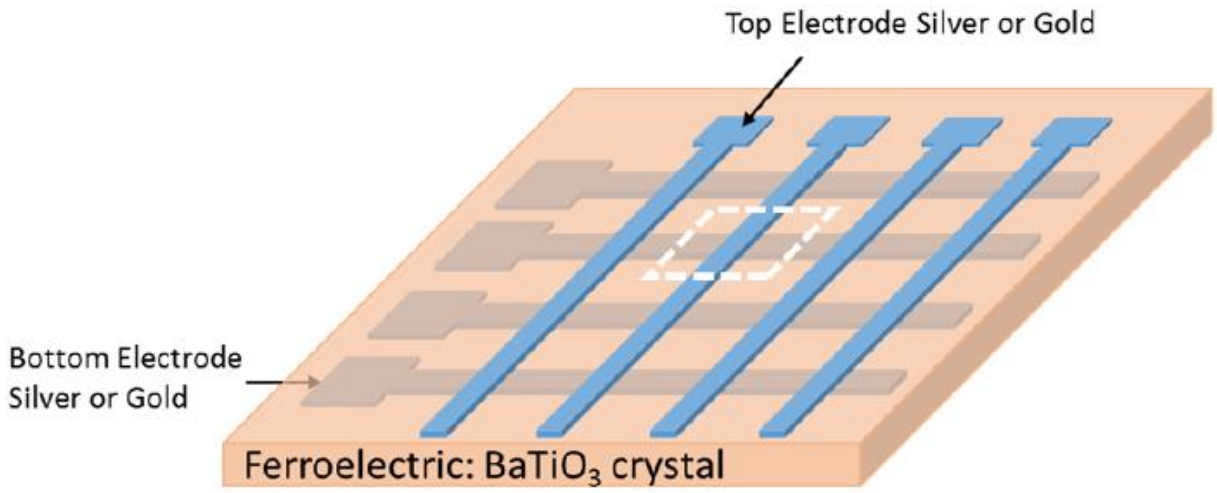

Figure 1.5. The first version of ferroelectric memory cells. [5]

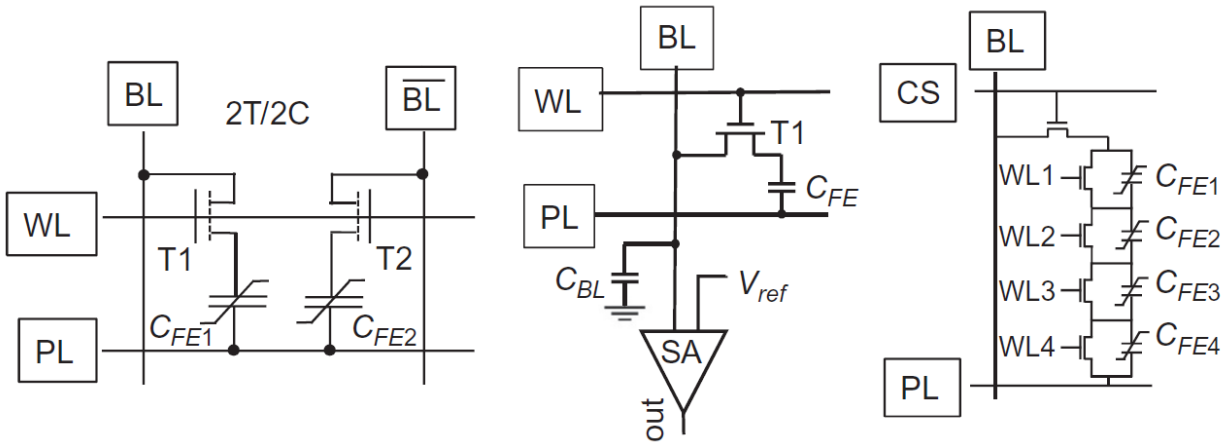

Figure1.6. FeRAM circuits of 2T/2C, 1T/1C, and FE NAND. [5]

The capacitor readout scheme using ferroelectric materials was first proposed in the 1950s. This first version of the memory cell has cross-point architecture and barium titanate (BTO) as the ferroelectric layer. However, this version of memory cells suffered from disturb issues arising from the cross-point design. Later on in the 1980s, to avoid these disturb issues, metal-oxide-semiconductor (MOS) transistors were integrated in line with the capacitors working as select devices. The new device is a ferroelectric random access memory (FeRAM). The memory cell is similar to the structure of the dynamic random access memory (DRAM).

Many kinds of perovskite ferroelectrics were then tried in this architecture, such as bismuth titanate (BTO) and strontium bismuth tantalate (SBT), but they are not the best fit for FeRAMs because of the limitation in scaling and compatibility with CMOS. In the 1990s, lead zirconium titanate (PZT) based FeRAMs were commercialized.

The memory cell, similar to the DRAM, comprises of one transistor and one capacitor (1T/1C) or 2T/2C. The former is preferred for high-density applications, but the latter has enhanced signal and reliability. The main difference between the operation of DRAM and FeRAM is the potential of the bit line (BL) and the plate line (PL). In DRAMs, the PL is grounded, and the BL is precharged to half of the supply voltage. When the word line (WL) is charged, the transistor is turned on (connecting the capacitor with BL), then a transient current will discharge the capacitor. The transient current has opposite directions corresponding to the “0” and “1” states stored in the capacitor. While in FeRAMs, BL is set to 0V, WL and PL are supplied with electric pulses when reading/writing. The pulses from PL can either maintain the original polarization state or flip it, so the non-switching and switching current can be collected through BL.

The FeRAM has another architecture similar to the NAND Flash, multiple groups of parallel transistor and capacitor can be connected in series between BL and PL. To access a single unit, the other capacitors can be short-circuited through their respective WLs. In this case, less connection to PL can reduce the circuit capacitance thus fastening the speed.

Among all the nonvolatile memories, the FeRAM has a comparably low energy consumption in writing (~1fJ/bit), fast speed, and nonvolatility. However, the complicated crystal structure of perovskite ferroelectrics sets challenges in the integration process. Meanwhile, the requirement for thin ferroelectric layers in 3-D architecture increases the difficulty in developing FeRAMs.

1.2.3 Ferroelectric field effect transistor (FeFET) [6]

The FeFET is constructed by substituting the conventional gate oxide in MOSFET with a ferroelectric layer. In this way, the readout of the memory unit becomes nondestructive. The integration of the structure is much easier compared to the FeRAM because 3-D architecture is no longer required.

The operation mechanism of FeFET is shown in Figure 1.7.

When applying a voltage Vg to the gate, the voltage across the whole stack is

$$V_g = \Psi_s + \Psi_I + \Psi_{FE} + \phi_{MS}$$

Where Ψ_s represents the surface potential of the semiconductor, Ψ_I and Ψ_{FE} represent the voltage drop across the insulator layer and the ferroelectric layer respectively. ϕ_{MS} is the work function difference between the gate metal and the semiconductor in the channel.

Ψ_I and Ψ_{FE} can be described by the surface charge Q_s, the polarization P, the material permittivity, and the layer thickness.

$$\Psi_I = Q_S \frac{t_I}{\varepsilon_0 \varepsilon_I}$$

$$\Psi_{FE} = (Q_S - P) \frac{t_{FE}}{\varepsilon_0 \varepsilon_{FE}}$$

The voltage dependence of the polarization P is described by a hysteresis loop. With the above complete set of equations, the relation of the surface potential and the total gate voltage V_g can be determined and is displayed in Figure 1.7 below. The blue curve shows the behavior of a conventional MOSFET, while the red curve adds the remanent polarization of the ferroelectric layer into consideration. The threshold voltage V_t of the transistor is when the surface potential reaches two times the fermi potential. In FeFET, the threshold voltage is split into two values because of the two remnant polarization states. This shift of the threshold voltage is the memory window of the FeFET, which is around two times the switching voltage of the ferroelectric material.

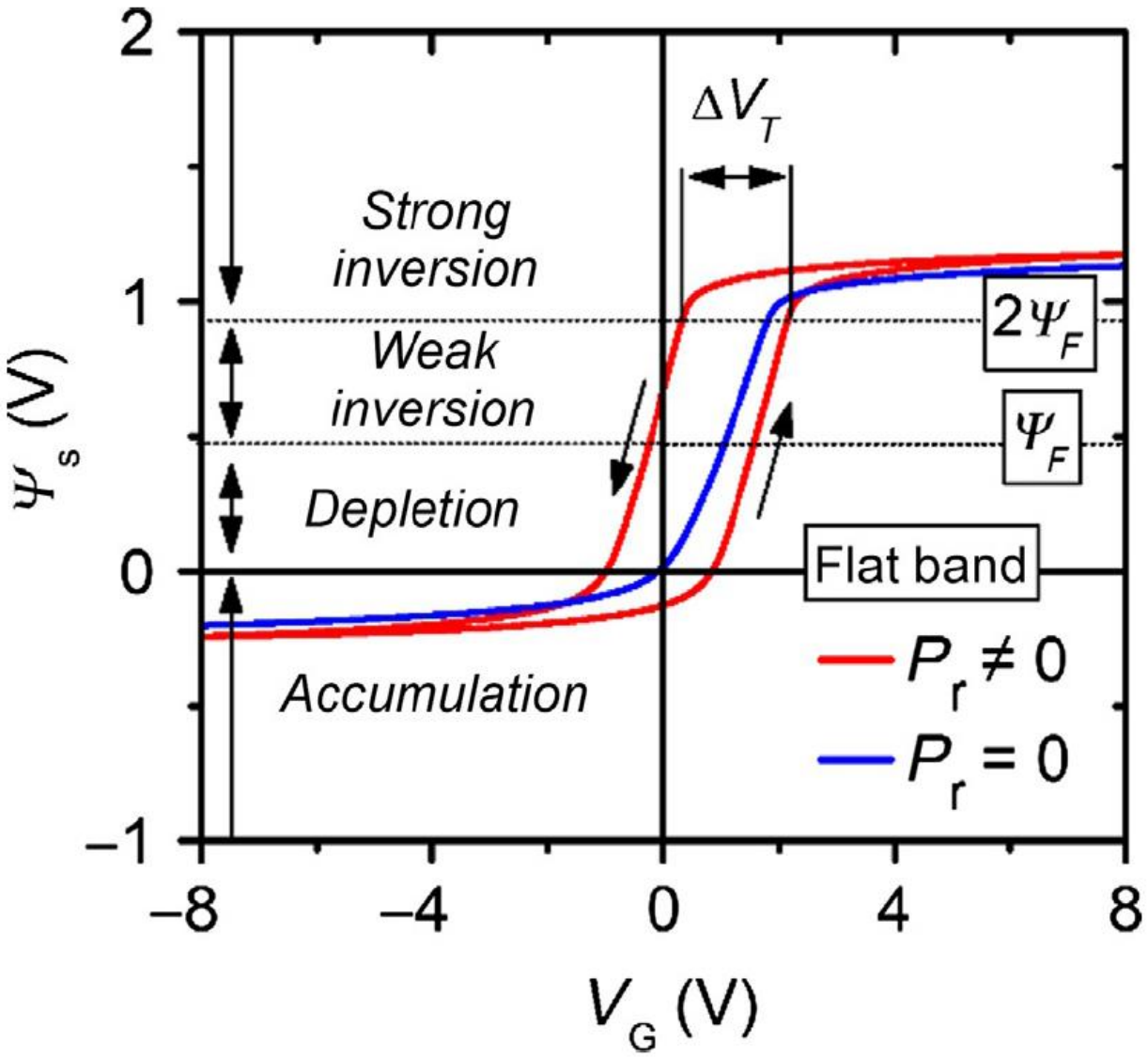

Figure 1.7. Channel surface potential of FeFET(red) and conventional MISFET(blue) versus the applied gate voltage. [6]

Realizing Ferroelectric Field-Effect Transistors (FeFETs) poses significant challenges, primarily due to interface imperfections in the metal-ferroelectric-semiconductor structure, low retention arising from large depolarization fields, and endurance issues. The interface quality is crucial for device performance, with impurities or defects impacting electrical characteristics. Addressing retention involves mitigating the depolarization field's effects, possibly by optimizing ferroelectric layer thickness or using better electrode materials. Endurance, a measure of the device's longevity under repeated switching, requires an understanding of fatigue mechanisms and exploration of more durable materials. Overcoming these obstacles is essential for harnessing FeFETs' potential in advanced electronic and memory devices, where their high speed, low power, and non-volatility are particularly advantageous.

1.2.4 Ferroelectric tunnel junction (FTJ) [7]

A ferroelectric tunnel junction has simpler structure compared to the devices above. It's a two-terminal device composed of a thin ferroelectric layer sandwiched by electrodes. The screening ability of the two electrode materials is different, so the potential barrier profile is not symmetric at opposite polarization states. The difference in the shape and height of the potential barrier could significantly alter the tunneling current across the junction. Therefore, the polarization status can be detected by the tunneling current. The mechanism of the tunneling is named as tunneling electroresistance (TER) effect and has been studied from a few important factors: the asymmetric screening length, the strain effect, and composite barriers. Among them, the FTJ with composite barriers leads to larger modulation of the potential profile, thus a larger TER effect.

The proposal of FTJ was first carried out in the 1970s, but the experimental attempt started in the 2000s. The first successful demonstration of FTJ was in 2009 with $BaTiO_3$. The difficulty lies in the fabrication of an ultrathin ferroelectric layer. Electron tunneling requires film thickness down to several nanometers. However, in traditional ferroelectrics, ferroelectric polarization is a collective behavior of massive unit cells, and the establishment of the ferroelectricity encounters difficulty from the high depolarization field.

The development of FTJ has become promising since ferroelectric hafnia was discovered. This ferroelectric material shows robust polarization in ultrathin films down to 1nm thick layer. We'll introduce our work about hafnia FTJ devices in Chapter 5.

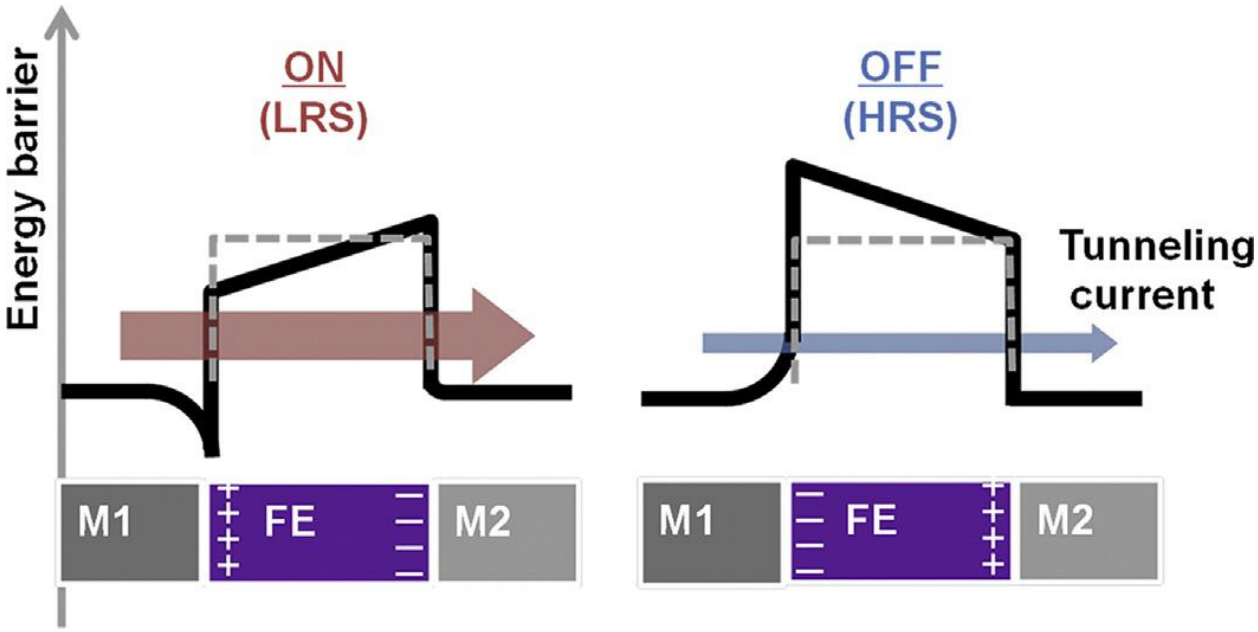

Figure 1.8. Schematic of FTJ tunneling energy barriers at ON and OFF states. [7]

1.3 Hafnium oxide thin films: progress and problems

Hafnia has long been a favored material for high-k gate oxides in CMOS technology due to its excellent compatibility with silicon. However, in 2011, a pivotal discovery was made by Böscke *et al*., who observed a non-linear response in hafnia capacitors, leading to the identification of a new polar phase of hafnia.[8] The stable bulk phase of hafnia at room temperature is traditionally the non-polar monoclinic phase (space group $P2_1/c$, as illustrated in Figure 1.9 left). In contrast, the polar phase is a metastable orthorhombic phase (space group $Pca2_1$, shown in Figure 1.9 right).[9] The polarization in hafnia arises from the displacement of oxygen ions. This polar phase can be stabilized in thin films through various methods, including strain and doping. It has been found that thinner films are more effective in maintaining the strain necessary to stabilize the ferroelectric phase, thereby exhibiting stronger ferroelectric properties. In the realm of hafnia thin films, robust polarization has been successfully achieved in films as thin as 1nm.[10] Notably, the mechanism of ferroelectricity in hafnia differs fundamentally from that of traditional perovskite ferroelectrics, which rely on the collective behavior of unit cells and exhibit a scaling effect not applicable to hafnia.

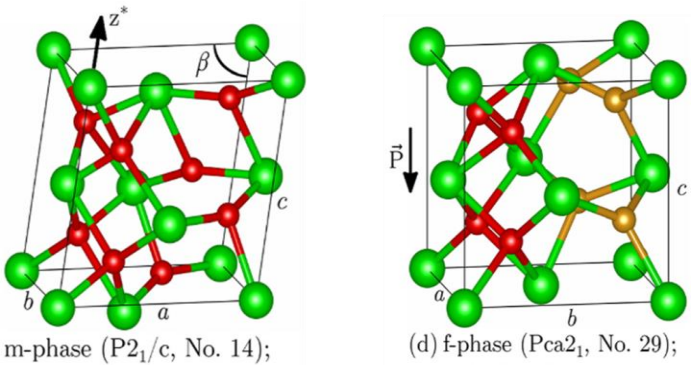

Figure 1.9. Ground phase of hafnia at room temperature (left) and ferroelectric phase of hafnia (right). The green balls represent hafnia ions, and the red(yellow) ones represent oxygen ions.[9]

These unique properties of hafnia have garnered increased attention for its potential in novel ferroelectric devices, particularly in ferroelectric tunnel junctions (FTJs) that require ultrathin ferroelectric layers for electron tunneling.

The following chapters of this thesis focus on this novel ferroelectric thin film material, with the aim of enriching the understanding and exploring the application of this material. Despite the burgeoning research aimed at overcoming challenges in hafnia ferroelectric device implementation, several critical questions remain unanswered.[11] A primary concern is understanding why the coercive field required for ferroelectric hafnia switching is so high, typically around ~1MV/cm, which is significantly greater than that of typical perovskite ferroelectrics. While this high coercive

field enhances non-volatile memory applications, it also increases the energy required for switching. Addressing this issue necessitates a deeper comprehension of hafnia's structure and switching pathways, prompting a need for single-crystal ferroelectric hafnia systems. Our efforts in fabricating cleaner structured ferroelectric hafnia thin films are detailed in Chapter 3, where we introduce pyrochlore metal as the electrode and deposition template. Epitaxial ferroelectric hafnia thin film is achieved, and the switching behavior is investigated in this epitaxial system.

Another crucial area of inquiry pertains to the mechanism behind the polarization fatigue of ferroelectric hafnia and ways to improve its endurance behavior. For ferroelectric random-access memory (FeRAM) devices to be commercially viable, they must withstand approximately 10^{15} electric field cycling cycles. However, hafnia ferroelectrics typically exhibit significant fatigue before reaching 10^{8} cycles, posing another challenge for their application.[11] Our study investigating the fatigue behavior of ferroelectric hafnia is presented in Chapter 4. We found that domain pinning and phase transformation from polar to non-polar phase are the root causes of the fatigue behavior and certain concentration of oxygen vacancies in ferroelectric hafnia is crucial to maintaining the ferroelectric phase for better endurance.

Furthermore, to gain insight into the future application, Chapter 5 discusses a prototype FTJ with high Tunneling Electro-Resistance (TER) and experimental evidence supporting the scale-free property of hafnia, providing crucial insights into the potential applications of hafnia in advanced ferroelectric technologies.

References

[1] The Economist, “The cost of training machines is becoming a problem”, https://www.economist.com/technology-quarterly/2020/06/11/the-cost-of-training-machines-is-becoming-a-problem, 2020

[2] Clarissa Garcia, “The Real Amount of Energy A Data Center Uses”, https://www.akcp.com/blog/the-real-amount-of-energy-a-data-center-use/, 2022

[3] Semiconductor Industry Association and others, “Rebooting the IT revolution: A call to action,” [Online] https://www.src.org/newsroom/rebooting-the-it-revolution.pdf, 2015.

[4] Liu, X., Liu, Y., Chen, W. *et al*. Ferroelectric memory based on nanostructures. Nanoscale Res Lett 7, 285 (2012). https://doi.org/10.1186/1556-276X-7-285

[5] Milan Pei, Uwe Schroeder, Thomas Mikolajick, Ferroelectric One Transistor/One Capacitor Memory Cell, Ferroelectricity in Doped Hafnium Oxide: Materials, Properties and Devices, 10.1016/b978-0-08-102430-0.00019-x, 2019

[6] Johannes Mueller, Stefan Slesazeck, Thomas Mikolajick, Ferroelectric Field Effect Transistor, Ferroelectricity in Doped Hafnium Oxide: Materials, Properties and Devices, 10.1016/b978-0-08-102430-0.00022-x, 2019

[7] Shosuke Fujii, Masumi Saitoh, Ferroelectric Tunnel Junction, Ferroelectricity in Doped Hafnium Oxide: Materials, Properties and Devices, 10.1016/b978-0-08-102430-0.00021-8, 2019

[8] T. S. Böscke, J. Müller, D. Bräuhaus, U. Schröder, U. Böttger, Ferroelectricity in hafnium oxide thin films, Applied Physics Letters 2011, 99, 102903.

[9] Lee, S.K., Bark, C.W. Crystallographic structure and ferroelectricity of epitaxial hafnium oxide thin films. J. Korean Ceram. Soc. 59, 25–43 (2022). https://doi.org/10.1007/s43207-021-00171-z

[10] Cheema, S. S., Kwon, D., Shanker, N., Dos Reis, R., Hsu, S. L., Xiao, J., ... & Salahuddin, S. (2020). Enhanced ferroelectricity in ultrathin films grown directly on silicon. Nature, 580(7804), 478-482.

[11] U. Schroeder, C. S. Hwang, H. Funakubo, Ferroelectricity in doped hafnium oxide: materials, properties and devices, Woodhead Publishing, 2019.

Chapter 2

Research Method and Design (Synthesis, Processing, and Characterization of Ferroelectric $Hf_{0.5}Zr_{0.5}O_2$)

2.1 Epitaxial deposition using Pulsed Laser Deposition (PLD)

Pulsed Laser Deposition (PLD), a technique pioneered in 1965, employs intense laser pulses to vaporize material from a target, creating a plasma that crystallizes onto a heated substrate. The method gained significant traction in the research community in 1987, following demonstrations at Bellcore of its efficacy in depositing high-quality epitaxial films of high-temperature superconductors. PLD is renowned for its ability to grow epitaxial thin films with precise stoichiometric transfer from the target to the film, making it a preferred method for creating high-quality epitaxial layers.[1]

The setup of the PLD apparatus is illustrated in Figure 2.1. The system utilizes a pulsed excimer (KrF) laser with a wavelength of 248nm. The laser beam first passes through an aperture, filtering out to select the most homogeneous part of the beam. This is followed by a convex lens, which concentrates the beam's energy. The resulting laser spot, an exact replica of the aperture, typically spans several square millimeters. This setup focuses tens of milli-Joules of energy onto a small area of the ceramic target, achieving a high energy density of ~ J/cm^2. When the laser pulse strikes the ceramic target, which possesses the same composition as the desired film, it ablates the material into a plasma state. This plasma (plume), a mixture of individual ions, atoms, and molecules, is then deposited onto the substrate. The highly reactive species in the plasma adhere to the substrate's surface, where they crystallize in an oxygen-rich environment.

The density of the target plays a crucial role in the PLD process. If the target material is not sufficiently dense, it becomes more susceptible to ablation. This leads to a higher likelihood of clusters and particles from the target material being present in the plasma, potentially affecting the quality of the deposited film. Therefore, careful consideration of target material density is essential in PLD to ensure the desired film quality and composition.

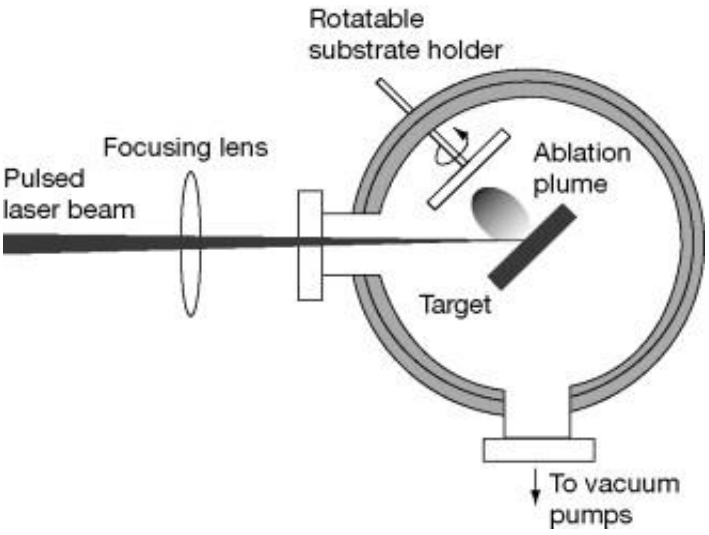

Figure 2.1. Schematic diagram of PLD. From https://bristoldynamics.com/research/optical-emission-spectroscopy/

PLD stands out as a distinctive method for producing epitaxial and nearly single-crystal thin films of complex oxides. This technique is highly versatile, enabling the deposition of a wide array of materials, including high-temperature superconductors, metals, ferroelectrics, ferromagnets, dielectrics, and various types of heterogeneous oxide layers. The key to the versatility of PLD lies in its ability to deposit these materials onto specifically chosen substrates, allowing for the creation of epitaxial thin films that are tailored to the desired application. This capability makes PLD an invaluable tool in the fabrication of advanced materials for a range of technological applications

The crystalline order of films deposited through PLD is significantly influenced by the choice of substrate, primarily due to the lattice matching at the interface between the two materials. For successful epitaxial growth, a certain degree of mismatch, typically small, is essential. This mismatch is quantified using a criterion defined as

f<0.1, where f is the lattice mismatch factor given by: [2]

$$f = \frac{2(a_f - a_s)}{(a_f + a_s)} \approx \frac{a_f - a_s}{a_s}$$

Here, *af* and *as* represent the atomic spacings of the film and substrate crystals, respectively, along the same in-plane direction.

Epitaxial growth via PLD is particularly adept at providing various types of strain required in thin-film engineering, a critical factor in manipulating film properties. A significant portion of materials grown by PLD are perovskites, which leads to the frequent use of certain lattice-matched substrates for deposition. These substrates typically include $SrTiO_3$, $LaAlO_3$, MgO, ZrO_2, and sapphire, all of which are common in PLD processes. The subsequent figure illustrates the lattice parameter relationships between commonly used perovskite substrates and traditional perovskite ferroelectrics. These single-crystal materials can be precisely cut along [100], [110], or [111]

orientations to impart the desired strain on the deposited film, a critical aspect in tailoring the material's properties for specific applications. This strategic manipulation of strain through substrate selection underscores the versatility and precision of PLD in thin film fabrication.

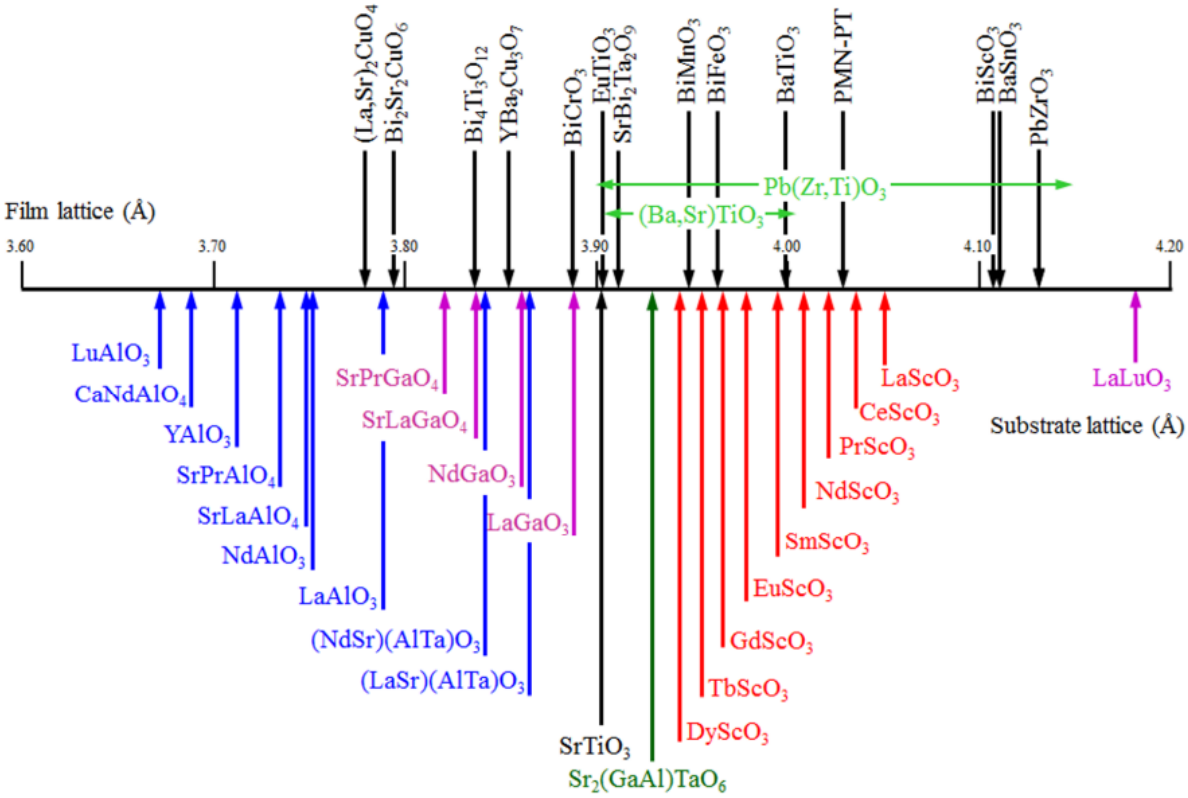

Figure 2.2. Lattice parameters of perovskite structures for surface strain engineering. [3]

In our experimental setup, we employed two distinct stack configurations for the epitaxial deposition of Hafnium Zirconium Oxide (HZO). The first configuration utilized substrates of Yttrium Stabilized Zirconia (YSZ) paired with electrodes having pyrochlore structures, such as $Pb_2Ir_2O_7$. The primary benefit of this stack lies in its high lattice match, which ensures better structural alignment between the layers. This approach, aimed at optimizing the deposition process and enhancing the quality of the HZO films, is comprehensively detailed in Chapter 3 of this study.

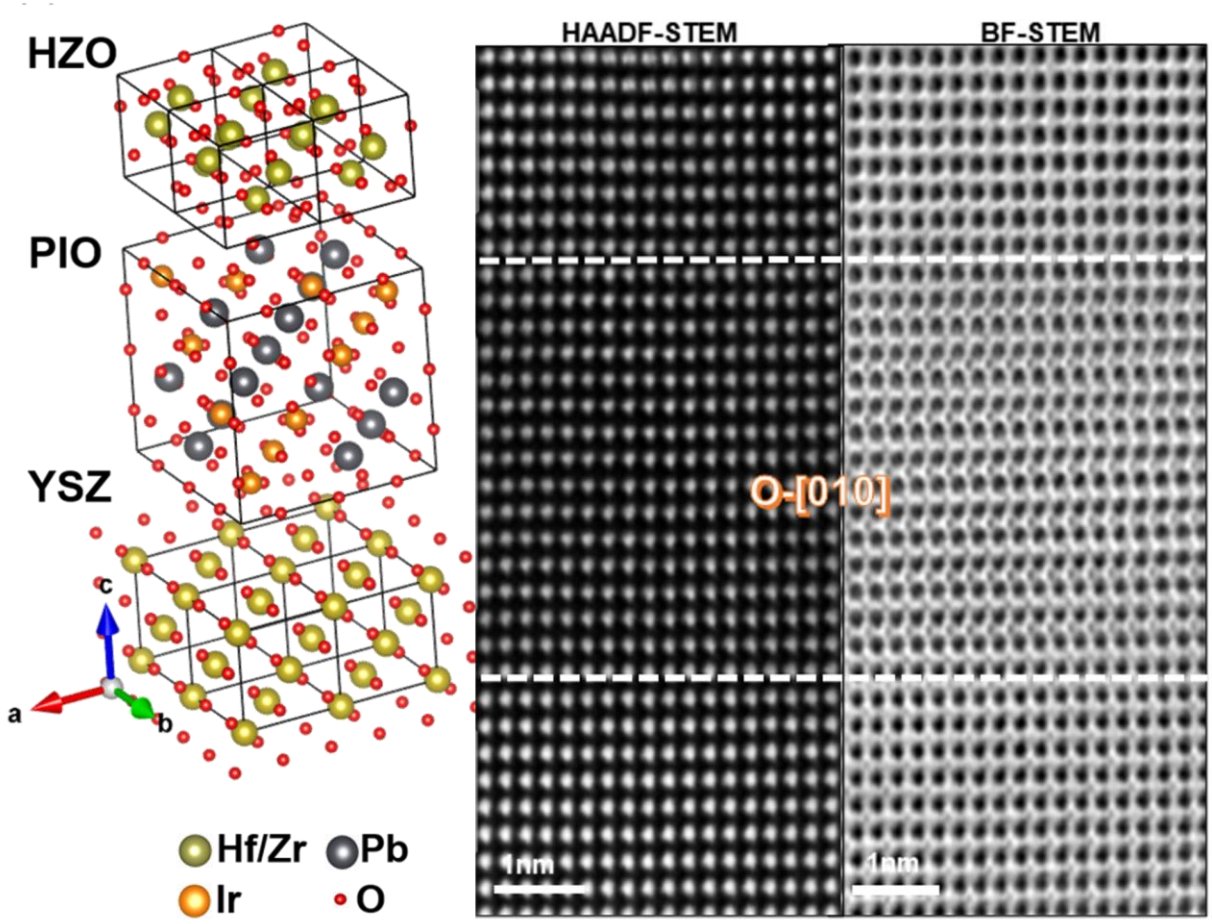

Figure 2.3. Schematic of the HZO/PIO/YSZ stack (left) and real STEM data of PIO/HZO/PIO stack (right)

The second approach in our experiments involved depositing Hafnium Zirconium Oxide (HZO) on a combination of $La_{0.67}Sr_{0.33}MnO_3$ (LSMO) perovskite electrodes and $SrTiO_3$ substrates. While the HZO films grown on this material system do not exhibit the same level of epitaxial quality as those in the first approach, they possess a (111) orientation with a highly textured structure. This particular configuration, despite its less epitaxial nature, has yielded a wealth of electrical properties that are of significant interest. The detailed exploration of these properties, along with the nuances of this material system, will be elaborated upon in Chapters 4 and 5 of this study.

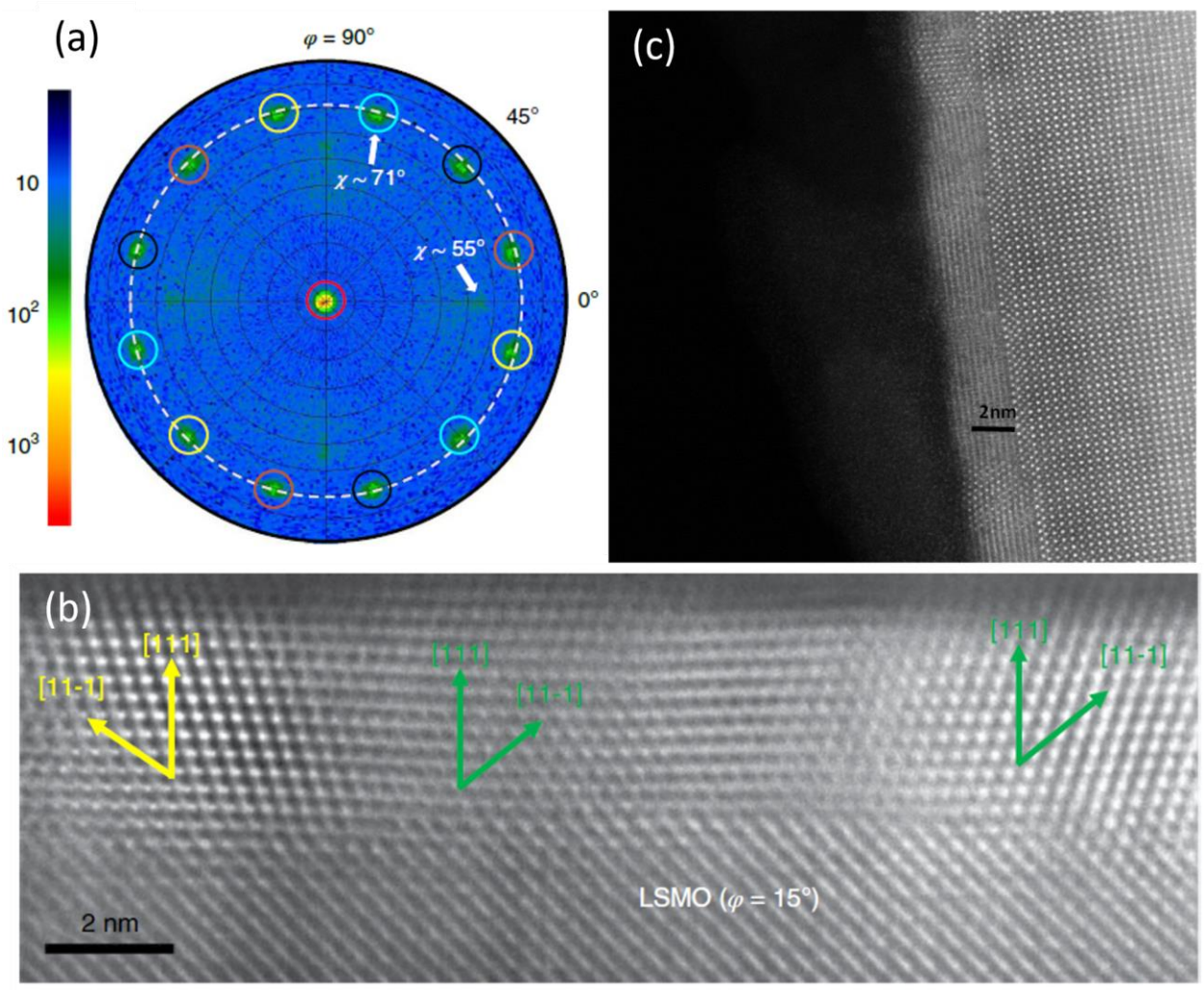

Figure 2.4. Highly textured HZO film on LSMO electrode and STO substrate. (a) X-ray pole figure from literature [4] showing 12 [111] peaks, indicating 4 orientations of HZO crystals. (b) STEM image of the textured film from literature [4]. (C) STEM image of our ultrathin textured HZO film on LSMO electrode.

2.2 Structural characterization of epitaxial ferroelectric hafnia thin films

2.2.1 X-ray diffraction (XRD)

An X-ray diffractometer is a vital instrument widely used for structural characterization in both research and industrial settings. In our project, X-ray Diffraction (XRD) plays a crucial role in determining the crystal structure of deposited thin films and assessing their crystallization quality. This technique is integral for understanding the material properties and guiding further development in thin film applications.

The underlying mechanism of XRD is depicted in Figure 2.5. [5] Here, an X-ray beam with a wavelength λ impinges on a series of atomic planes at an angle θ. The spacing between these crystalline planes, denoted as d, induces a relative phase shift between the X-rays scattered from different planes. This phase shift results in an optical path difference between adjacent planes, represented by $2d_{hkl}\sin\theta$ (marked in orange color in the figure). Based on simple geometric derivation, constructive interference occurs at specific angles, known as the Bragg angles (θ_B). This phenomenon is encapsulated in the Bragg Equation

$$n\lambda = 2d_{hkl}sin\theta_B$$

which links the incident angle, plane spacing, and wavelength. The Miller indices (hkl) in this equation represent the orientation of the crystalline planes, while N is an integer denoting the order of diffraction. The Bragg Equation is instrumental in determining the characteristic diffraction peak angles for various crystalline structures, providing insights into the material's atomic arrangement.

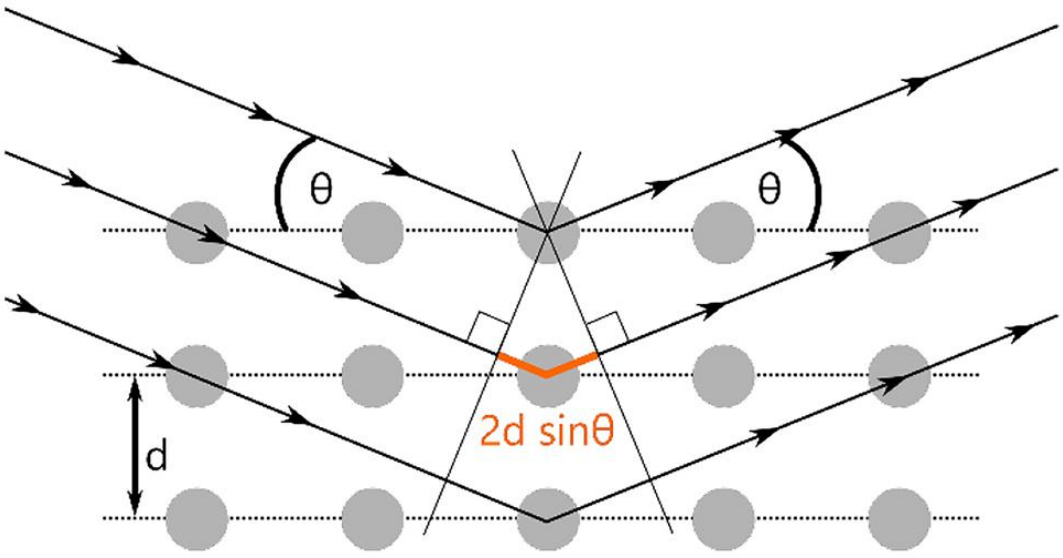

Figure 2.5. Schematic representation of Bragg's Equation. [5]

Figure 2.6 illustrates the fundamental setup of a 4-axis diffractometer, commonly used for thin film XRD measurements.[5] The sample is mounted onto a central stage, and the system's primary adjustments include the angle between the incident X-ray beam and the detector (2θ) and the angle between the incident beam and the sample surface (ω). To enable comprehensive analysis, including the assessment of in-plane texture and the generation of 2D pole figures or Reciprocal Space Mapping (RSM), two additional degrees of freedom are incorporated. These are the tilting angle (ψ or χ) and the azimuth angle (φ). These extra degrees of freedom allow for a more detailed exploration of the crystallographic texture and orientation distribution within the thin films, providing a richer understanding of the material's structural characteristics.

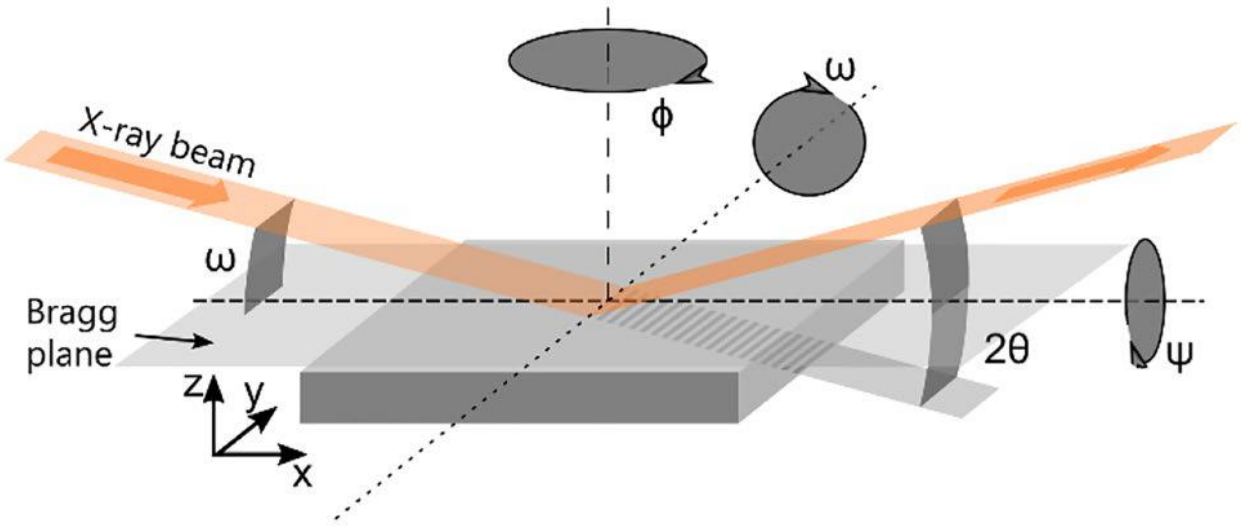

Figure 2.6. Schematic of a typical 4-axis diffractometer used for thin film XRD. [5]

XRD's ability to precisely analyze crystal structure and orientation makes it an indispensable tool in materials science, particularly for thin film research. It enables scientists to correlate structural properties with functional characteristics, paving the way for advancements in various applications ranging from electronics to energy materials. The versatility and precision of XRD in thin film characterization underscore its importance in both academic research and industrial material development.

2.2.2 Scanning transmission electron microscopy (STEM)

Scanning Transmission Electron Microscopy (STEM), an advanced development in the field of transmission electron microscopy (TEM), represents a significant integration of TEM with scanning capabilities. This technique is primarily characterized by the incorporation of a field emission electron gun, which enables the creation of a STEM. [6] STEM uniquely combines the principles and characteristics of both scanning and conventional transmission electron analysis. Its spatial resolution, capable of reaching sub-angstrom levels, is adept at characterizing and analyzing material microstructures as well as the fine chemical components at nanometer and

atomic scales. This high-resolution capability renders STEM an invaluable tool in diverse fields such as metallurgy, materials science, environmental science, and biology.

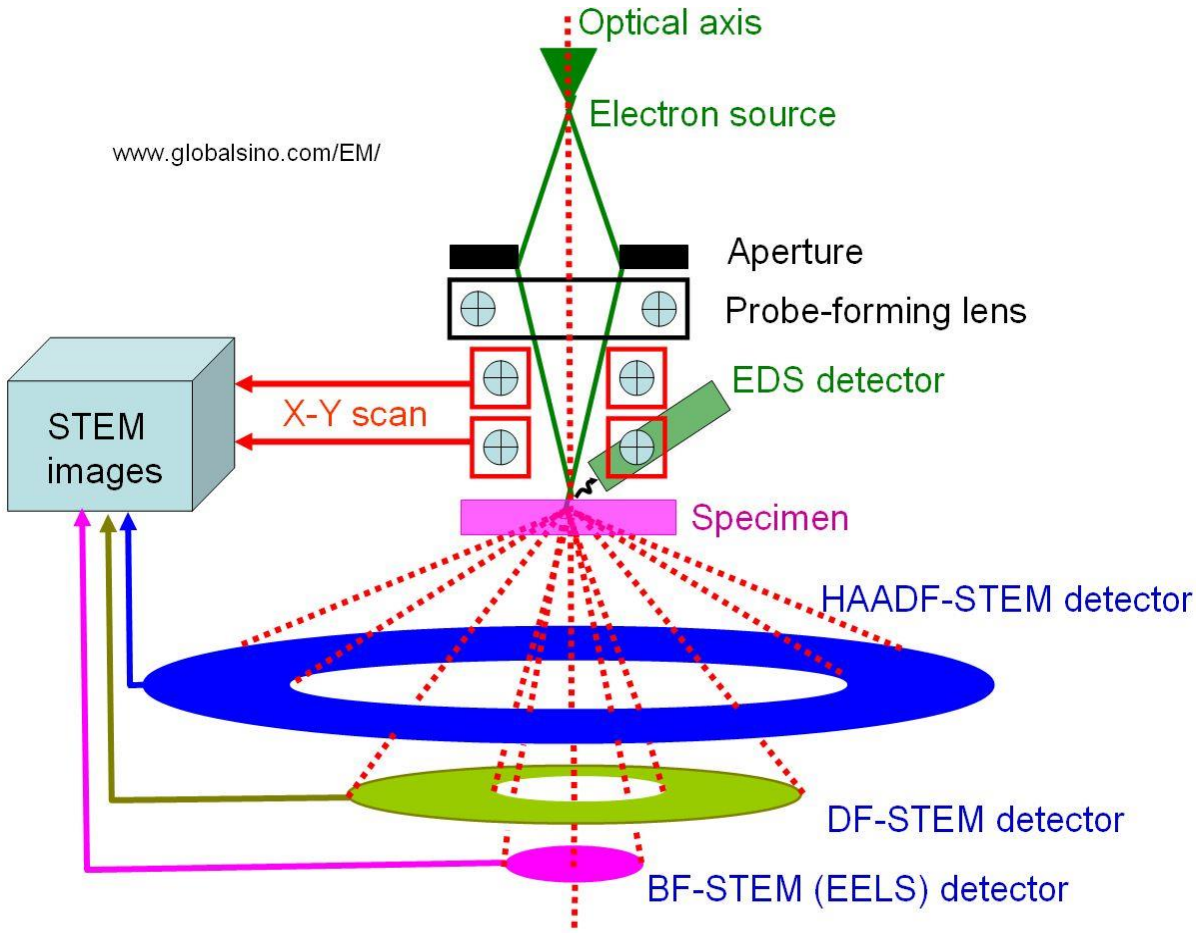

Figure 2.7. Schematic representation of STEM components and imaging modes. Taken from www.globalsino.com/EM.

In STEM, the electron beam generated by the field emission electron gun is concentrated into an atomic-scale electron beam spot through an intricate optical system. This focused electron probe scans the sample in a point-by-point raster pattern, controlled by a scanning coil. This meticulous scanning process allows for detailed analysis at an extremely fine scale.

STEM imaging distinguishes itself from parallel electron beam TEM by utilizing a concentrated electron beam to methodically scan across the sample. This approach differs from Scanning Electron Microscopy (SEM) in its detection methodology. In STEM, the detector is strategically positioned beneath the specimen, capturing either a transmitted electron beam stream or an elastically scattered electron beam stream. These captured signals are then amplified and displayed on a fluorescent screen, creating detailed bright-field and dark-field images.

The versatility of STEM is further enhanced by its various imaging modes, which collect scattered signals at different reception angles. This capability allows for the generation of multiple images from the same sample location, each providing distinct information about the material. Examples

of these imaging modes include annular bright-field imaging (ABF), annular dark-field imaging (ADF), and high-angle annular dark-field imaging (HAADF).

Structurally, the STEM can be viewed as a hybrid of scanning imaging and transmission analysis, effectively merging the functionalities of SEM and TEM. It comprises components such as an electron gun, an electron optical system, a sample chamber, annular detectors, and an imaging device (Figure 2.7). The primary distinction of STEM from TEM lies in the addition of scanning accessories, while its difference from SEM is evident in the placement of the detector beneath the sample, enabling a unique perspective and depth of analysis not achievable with other electron microscopy techniques. This advanced microscopy method is pivotal in pushing the boundaries of material characterization, allowing researchers to delve deeper into the micro and nano worlds. More STEM-involved experiments in our studies are introduced in Chapter 3.

2.3 Fabrication of test structures

In our study, various patterning techniques have been employed to fabricate capacitors, including photolithography, ion milling, wet etching, and electron beam lithography.

Photolithography is a widely used process in semiconductor fabrication, involving the transfer of geometric patterns from an optical mask onto a photoresist layer applied to thin film materials. This process can utilize different types of light, such as ultraviolet (UV), deep UV, extreme UV, or X-ray. The feature size of the lithography is determined by the wavelength of the UV light used. The photoresist (PR), available in positive and negative types, reacts to light exposure by either breaking down or hardening. Subsequently, a solvent or developer is used to remove the softened portion of the photoresist, remaining the PR mask for the following etching.[7] In this project, we employed OCG 825 35CS, a positive photoresist that responds to light in the 320-436nm wavelength range, with Microposit 351 as the developer. The process involved uniformly applying a micrometer-thick photoresist layer onto the thin film stacks, followed by baking and UV exposure through a photomask. The development stage then removes the exposed photoresist, leaving behind a patterned protective layer on the thin film surface.

Wet etching and ion milling are the primary etching techniques used post-development. Wet etching, which utilizes liquid chemicals, is a chemical reaction-based process that removes film materials, producing soluble byproducts. This isotropic etching method is faster than dry etching but is less suitable for directional etchings or nanoscale dimensions. However, its high selectivity makes it an ideal choice for certain applications.[8] In our project, a dilute NaIO4 solution is used in wet etching to remove $SrRuO_3$ electrode material.

Ion milling, on the other hand, is a physical sputtering process where a high-energy ion gun bombards the sample surface. This interaction with surface atoms facilitates the etching of top electrode materials. While ion milling is versatile and applicable to various materials, it can potentially damage the sample surface or sublayers.[9] In our study, ion milling is employed in the fabrication of Pt/LSMO/HZO/LSMO capacitors.

Electron beam lithography represents a more advanced mask-less patterning technique. Evolved from scanning electron microscopy, it is particularly suited for sub-10 nm device fabrication. This technique boasts the ability to accurately address small features, produces low defect densities, and can directly generate patterns from design data. However, this technique has low throughput, limiting its usage to photomask fabrication, low-volume production of semiconductor devices, and research and development.[10] In our experiments, as discussed in Chapter 5.2, capacitors down to 50nm in diameter are patterned using electron beam lithography at Western Digital. This method's precision and direct patterning capability from design data make it especially valuable for creating intricate nano-scale devices.

2.4 Atomic force microscopy (AFM) and piezoelectric force microscopy (PFM)

Atomic Force Microscopy (AFM), also referred to as Scanning Force Microscopy (SFM), represents a groundbreaking advancement in the realm of microscopy. It offers the unique capability to achieve nanometer-scale, high-resolution imaging, surpassing the optical diffraction limit by a factor of 1000. The pioneers of AFM, Gerd Binnen, Calvin Quate, and Gerber not only introduced a revolutionary instrument but also paved the way for exploring non-conductive materials at the atomic level. Their invention in 1986 marked the beginning of a new era in microscopy, eventually leading to the commercialization of the first AFM in 1989. [11]

AFM stands as a cornerstone in the manipulation, imaging, and measurement of materials at the nanoscale, enabling researchers to gather information through microcantilever sensing. This information is acquired by the microcantilever as it "feels" the surface via a sharp, thin probe, with the ability to detect forces at atomic-level resolution. Notably, AFM bridges the gap left by scanning tunneling microscopy, as it accommodates both conductive and non-conductive materials.

While AFM and STM share common goals of characterizing surfaces at the atomic scale, they employ fundamentally different principles. Where STM relies on the electron tunneling effect, AFM detects interactions such as atomic bonding, van der Waals forces, or the Casimir effect to map the sample surface.

The heart of AFM is the microscopic cantilever, adorned with a nanoscale probe at its tip, used to scan the sample surface. Typically constructed from materials like silicon or silicon nitride, the cantilever's probe tip boasts a radius of curvature at the nanometer scale. As the probe approaches the sample surface, it adheres to Hooke's law, resulting in the deflection of the cantilever. This deflection occurs due to a range of forces acting upon the sample surface, including mechanical contact forces, van der Waals forces, and chemical bonding. A laser beam is reflected from the microcantilever onto a photodiode array to detect this cantilever deflection.

Given the potential for probe-sample collision when scanning at a constant height, it’s important to implement a feedback system. Traditionally, the sample is placed on a piezoelectric tube, allowing adjustments in the z-direction to maintain a constant probe-sample distance, and in the x- and y-directions to facilitate scanning. Furthermore, alternative techniques, like the "tripod" approach, are detailed. This approach scans in three directions, partially mitigating the distorting

effects of piezo scanning. Recent designs employing a vertical piezoelectric scanner for the probe and additional piezoelectric junctions for sample scanning are also introduced. The result of these scans is the topography of the sample, represented as $z = f(x, y)$.

AFM has a few different operational modes. The primary modes of operation are static mode, also known as contact mode and dynamic mode. Static Mode entails the cantilever traversing the sample surface, directly revealing surface topography through cantilever deflection. Dynamic Mode, however, introduces cantilever vibration at or near its fundamental or harmonic frequency, with amplitude, phase, and resonance measurements providing insights into probe-sample forces.[11]

The Contact Mode keeps the physical interaction between the probe and the sample surface. The selection of a low-stiffness cantilever is crucial for Contact Mode to ensure a large enough deflection signal while maintaining low interaction forces. This mode is suitable for harder samples like metals and semiconductors but incompatible with soft and fragile biological specimens.

The non-contact mode does not make physical contact with the sample surface. Instead, the probe vibrates with a frequency slightly higher than its resonant frequency, and the amplitude is kept within a few nanometers. The interaction forces, including Van der Waals forces, reduce the vibration frequency of the cantilever as it approaches the sample surface. By controlling the average distance between the probe and the sample, the frequency is reduced using a feedback loop, facilitating surface topography reconstruction.

Tapping Mode, also known as intermittent contact mode, is a solution to the challenges posed by liquid layers on sample surfaces. The cantilever oscillates at an amplitude substantially larger than 10 nanometers. As the probe approaches the sample surface, van der Waals, dipole-dipole, and electrostatic forces cause the amplitude to diminish. An automated servo mechanism is responsible for maintaining the preset amplitude of the cantilever during scanning, thus yielding the AFM tapping mode image. Tapping mode is effective in avoiding lateral friction and minimizing wear and tear on probes and samples.

Piezoelectric Force Microscopy (PFM) is an advanced microscopic technique that extends the capabilities of Atomic Force Microscopy (AFM) by focusing on the electrically induced deformation of samples under an excitation voltage. This technique is particularly adept at harnessing the PFM signal through the use of a fixed-frequency excitation signal, which is typically set at a frequency significantly lower than the probe's resonance frequency. The PFM signal is then precisely extracted using a lock-in amplifier.

The mechanism of contrast and detection in PFM hinges on the piezoelectric nature of ferroelectric materials. For instance, when the polarization and the applied electric field are parallel (as shown in Figure 2.7a), the material undergoes positive deformation (expansion), resulting in a piezoresponse signal that is in phase with the applied voltage. Conversely, if the electric field is antiparallel to the spontaneous polarization, the material contracts, causing the cantilever to lower (illustrated in Figure 2.7b), leading to a phase shift of 180° between the electric field and the piezoresponse signal.[12]

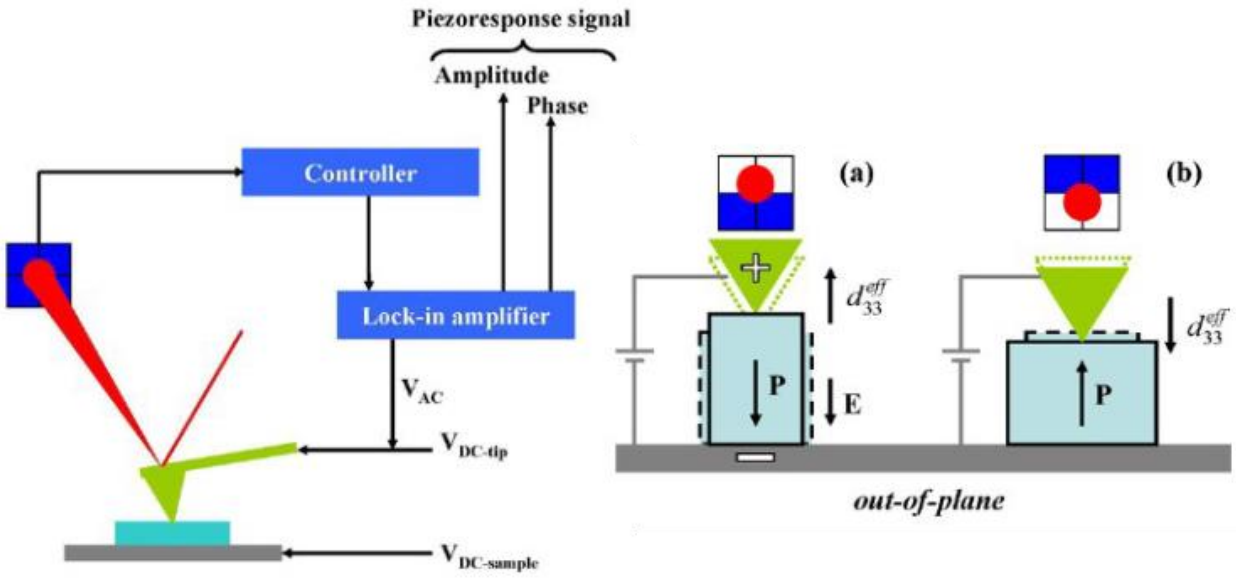

Figure 2.7. Working mechanism of PFM. [12]

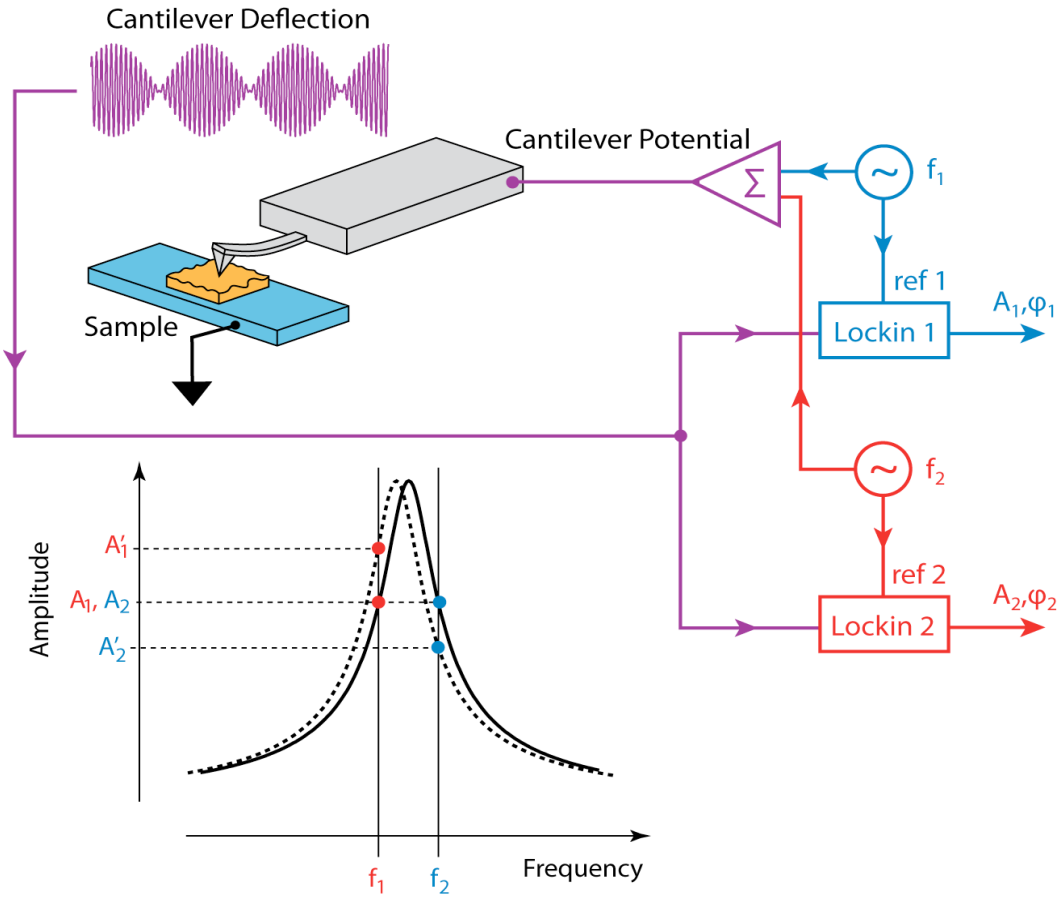

Figure 2.8. DART operation mechanism. [13]

A significant advancement in PFM is the Dual AC Resonance Tracking (DART) technique. This method effectively minimizes crosstalk arising from shifts in resonant frequency by continuously tracking the contact resonant frequency. It employs a feedback loop that adjusts the drive frequency of the cantilever to match the resonance. Unlike traditional methods that use phase for frequency feedback, DART utilizes the difference between two amplitude signals. Figure 2.8 depicts a schematic of this approach, showing how the amplitudes (A1' and A2') change as the resonant frequency shifts. This change in the A2-A1 signal prompts the feedback loop to adjust the drive frequency until the differential signal is neutralized. [13]

PFM is instrumental in gaining comprehensive insights into ferroelectric materials, including: 1. Static domain structure, which is the visualization and characterization of the static domain structure within ferroelectric materials. 2. Domain Inversion Behavior: Analysis of domain inversion behavior, providing clarity on dynamic processes within these materials. 3. Slow Relaxation Process: Ability to capture slow relaxation processes in ferroelectric samples, enhancing understanding of their temporal behavior. 4. Micro-Region Hysteresis Line: Delineation of micro-region hysteresis lines, offering insights into the intricate behavior of ferroelectric materials at a microscale.

The applications and studies involving both AFM and PFM, along with their implications in ferroelectric material research, will be further discussed and elaborated in Chapters 3 and 4 of this study.

2.5 Electrical characterization of epitaxial ferroelectric hafnia thin films

2.5.1 Hysteretic response

In the realm of ferroelectric research, the Polarization-Electric Field (P-E) loop is a fundamental characterization tool, graphically representing the relationship between the polarization (P) developed in a device and the electric field (E) applied to it, typically observed at a specific frequency. The following examples are a few typical responses from different types of electrical devices.[14]

For an ideal linear capacitor, the P-E loop manifests as a straight line, as depicted in Figure 2.9a. The gradient of this line is directly proportional to the capacitor's capacitance. This linear relationship stems from the fact that in an ideal capacitor, the current leads the voltage by 90 degrees. Consequently, the charge (which is the integral of current over time) is in phase with the voltage.

In contrast, for an ideal resistor, where the current and voltage are in phase, the resulting P-E loop forms an ellipse centered at the origin, as shown in Figure 2.9b. This pattern reflects the phase lag between current and voltage in resistive elements.

When these two components – the capacitor and resistor – are combined in parallel, the P-E loop takes the shape illustrated in Figure 2.9c. This configuration represents a lossy capacitor, where

the loop's enclosed area is proportional to the device's loss tangent, and its slope relates to the capacitance.

However, when examining less ideal, nonlinear devices such as ferroelectric materials, the P-E loop exhibits a markedly different shape, as seen in Figure 2.9d. In ferroelectric materials, the P-E loop deviates significantly from the linear and circular patterns of ideal capacitors and resistors. This deviation is due to the inherent nonlinearity and hysteresis effects present in ferroelectric materials. The shape and characteristics of the P-E loop in ferroelectric materials provide critical insights into their unique dielectric and ferroelectric properties.

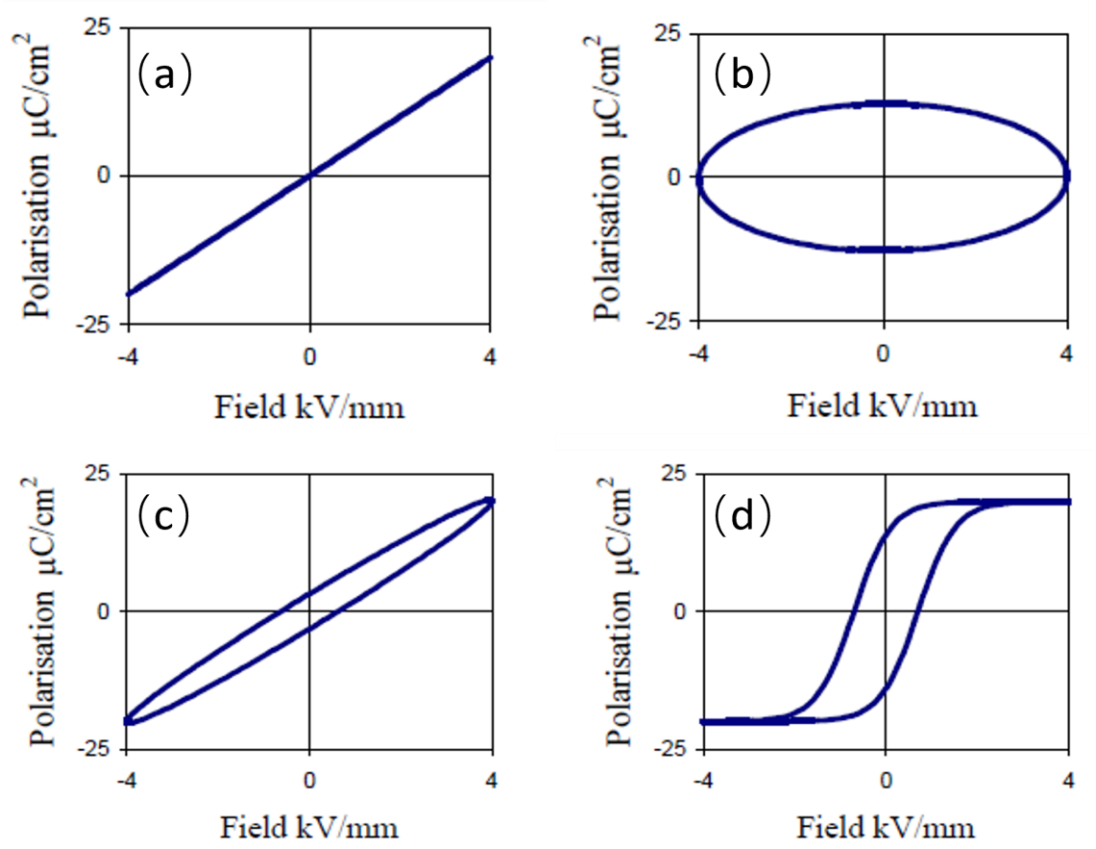

Figure 2.9. P-E response of a few typical devices: (a) Ideal linear capacitor. (b) Ideal resistor. (c) Lossy capacitor. (d) Ferroelectrics

Understanding these P-E loops is crucial for the analysis of ferroelectric materials in various technological applications. They not only reveal the material's fundamental electrical characteristics but also guide the optimization and design of ferroelectric devices for specific purposes.

2.5.2 Positive-Up-Negative-Down (PUND)

In the study of ferroelectric materials, a key parameter of interest is the remnant polarization. This term refers to the net polarization of a material in a zero-field steady state. However, directly

measuring remnant polarization presents challenges due to the presence of other factors, such as dielectric and leakage contributions, as well as the potential for parts of the material to relax or revert to their original state during switching.

Therefore, researchers commonly employ the Positive-Up-Negative-Down (PUND) technique for the indirect measurement of remnant polarization. This method involves a sequence of electrical pulses (Figure 2.10a). Initially, the ferroelectric capacitor is preconditioned to a negative polarization state. Subsequently, a switching pulse is applied, which reverses the polarization from negative to positive. This is followed by a non-switching pulse, where the capacitor maintains its positive polarization. Then two identical negative pulses are followed, basically doing the same thing again in the opposite direction.

By integrating the current during each pulse, it is possible to obtain two key values (Figure 2.10b): the switched polarization value (P*) and the non-switched polarization change (P^). The difference between these two values, denoted as delta P (P* - P^), is effectively twice the value of the remnant polarization commonly discussed in ferroelectric studies. Within this context, the P^ value comprises two main components: the integral of dielectric signal and leakage currents.

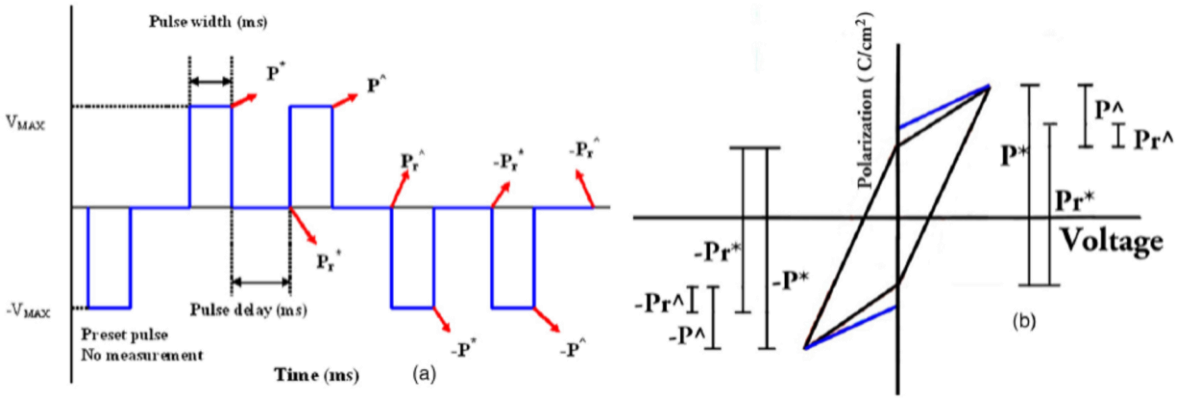

Figure 2.10. PUND measurement. (a) Electrical pulses. (b) The corresponding hysteresis loop From

This PUND technique provides a reliable method for gauging the remnant polarization in ferroelectric materials, offering valuable insights into their electrical behavior and potential applications. The precision and reliability of the PUND method make it a critical tool in the field of ferroelectric research, particularly for applications where accurate measurement of polarization characteristics is essential. Here in our project, the PUND measurement is frequently used to collect the polarization value during field cycling tests (Chapter 4).

References

[1] Pulsed Laser Deposition of Thin Films, edited by Douglas B. Chrisey and Graham K. Hubler, John Wiley & Sons, 1994 ISBN 0-471-59218-8

[2] Thin-Film Deposition Principles & Practice, Donald L. Smith, McGraw-Hill, 1995 ISBN 0-07-058502-4

[3] Reinhard Uecker, Rainer Bertram, Mario Brützam, Zbigniew Galazka, Thorsten M. Gesing, Christo Guguschev, Detlef Klimm, Michael Klupsch, Albert Kwasniewski, Darrell G. Schlom,

Large-lattice-parameter perovskite single-crystal substrates, Journal of Crystal Growth, Volume 457, 2017, P137-142, ISSN 0022-0248

[4] Y. Wei, P. Nukala, M. Salverda, S. Matzen, H. J. Zhao, J. Momand, A. S. Everhardt, G. Agnus, G. R. Blake, P. Lecoeur, B. J. Kooi, J. Iniguez, B. Dkhil, B. Noheda, Nat Mater 2018, 17, 1095.

[5] Harrington, G.F., Santiso, J. Back-to-Basics tutorial: X-ray diffraction of thin films. J Electroceram 47, 141–163 (2021). https://doi.org/10.1007/s10832-021-00263-6

[6] Scanning transmission electron microscopy, Wikipedia, https://en.wikipedia.org/wiki/Scanning_transmission_electron_microscopy

[7] Levinson, Harry J. (2005). Principles of Lithography. SPIE Press. ISBN 9780819456601.

[8] Jaeger, Richard C. (2002). "Lithography". Introduction to Microelectronic Fabrication (2nd ed.). Upper Saddle River: Prentice Hall. ISBN 978-0-201-44494-0.

[9] Howitt, D.G. (1984), Ion milling of materials science specimens for electron microscopy: A review. J. Elec. Microsc. Tech., 1: 405-414. https://doi.org/10.1002/jemt.1060010409.

[10] McCord, M. A.; M. J. Rooks (2000). "2". SPIE Handbook of Microlithography, Micromachining and Microfabrication.

[11] Binnig, G.; Quate, C. F.; Gerber, Ch. (1986). "Atomic Force Microscope". Physical Review Letters. 56 (9): 930–933. Bibcode:1986PhRvL..56..930B. doi:10.1103/PhysRevLett.56.930. ISSN 0031-9007. PMID 10033323.

[12] NT-MDT, Piezoresponse Force Microscopy (PFM) Introduction, Principles and Instrumental Aspects of Piezoresponse Force Microscopy by NTMDT, 2015

[13] Asylum Research, Piezo Force Microscopy using Dual AC Resonance-Tracking, Tech note 13, v3, 2010

[14] M. Stewart, M. G. Cain, D. A. Hall, Ferroelectric Hysteresis Measurement & Analysis, NPL Report CMMT(A) 152

Chapter 3

Highly Epitaxial HZO Thin Films on Pyrochlore Electrodes

3.1 Introduction

As previously discussed in Chapter 1, hafnia-based ferroelectrics have robust ferroelectricity at the nanoscale thickness and compatibility with silicon-based microelectronics. These advantages make them promising candidates for non-volatile memory and logic [1-4]. Although multiple groups have studied hafnia since its polar orthorhombic phase (space group $Pca2_1$) was first discovered in 2011 [5], the formation mechanism of the polar phase in thin films and the switching pathway are still under debate [4, 8]. In the bulk, the polymorph of HfO_2 (and ZrO_2) that is stable at room temperature is the non-polar phase with the monoclinic space group, $P2_1/c$. Its high-temperature and high-pressure polymorphs have tetragonal ($P4_2/nmc$) or cubic ($Fm\bar{3}m$) symmetry [9]. While the polar O-phase is a metastable phase in room temperature. Theoretical calculations show that the O-phase [10] is stable under hydrostatic pressure (3-4 GPa) and has been stabilized via doping [11] and strain [6]. An aspect of interest is the nature of the interfaces between the polar/non-polar phases, which will tell us about the nature of the phase transition from the O-phase to the M-phase. In this regard, Grimley *et al*. [12] have studied the atomic structure of complex mixture of polar domains, non-polar domains, and interface boundaries in Gd-HfO_2 using high-resolution electron microscopy. Park *et al*. [13] revealed the formation of polar and non-polar phases with different strain effects using different doping compositions. Among all the dopants, Zr is one with the best performance since the same valance state and ion radius as Hf. Within the (Hf, Zr)O_2 (HZO) system, $Hf_{0.5}Zr_{0.5}O_2$ has the largest remnant polarization [14]. Thus, we chose the same composition in our studies.

In previous studies on HZO, most samples were grown by ALD and were (111)-textured polycrystalline films [6]. Although the grain boundaries are thought to assist in the stabilization of the metastable O-phase, polycrystalline samples do not provide a simple model system to reveal the intrinsic material properties. In this context, there have been attempts to create epitaxial films of the desired O-phase [2, 3, 15-19]. For example, Wei *et al*. [3] demonstrated the growth of epitaxial (111)-oriented polar HZO films using a (110)-oriented $La_{1-x}Sr_xMnO_3$ layer as the bottom electrode to seed the growth of the HZO layer. Also, epitaxial growth of orthorhombic HZO on (001) Si, (111) Si, and (001) yttria-stabilized zirconia (YSZ) substrates has been demonstrated [15, 17-19]. With this as the background, we set out to study pathways to stabilize the polar O-phase, its stability as a function of thickness, and most importantly how the polarization switching evolves as a function of film thickness.

3.2 Lattice matching and strain

Recognizing that improved epitaxial growth (i.e., full in-plane orientational locking) of the HZO layer requires seeding it with a bottom electrode that presents a suitable structural and chemical template, we first sought out conducting oxide electrodes that would provide an ideal structural and chemical template to seed the growth of epitaxial HZO layers. Within the large number of conducting oxides [20], we have identified that the family of conducting oxide pyrochlores, exemplified by (PIO) and (BRO) (both with $Fd\bar{3}m$ symmetry and lattice parameters of 10.28 Å and 10.30 Å, respectively) [21, 22], are ideal metallic bottom electrodes for the synthesis of epitaxial HZO layers. A key to our selection of such pyrochlores as the bottom electrode lies in the fact that the crystal chemistry of pyrochlores bears similarity to that of the HZO system; the formal unit cell of the pyrochlores contains 8 fundamental building blocks and thus there is an approximately 2:1 matching of the unit cell of the pyrochlores with that of HZO. Such pyrochlore iridates and ruthenates also exhibit excellent metallic conductivity with typical room-temperature resistivity < 10−3Ω·cm [21, 22] and are also of interest for electrocatalysis [23, 24]. The presence of two heavy element cations (Pb^{+2} and Ir^{+4}) also provides an opportunity for studying the effects of the large inherent spin-orbit coupling on the electronic structure [25]. Finally, it is noteworthy that pyrochlore bismuth ruthenate is extensively used as a contact electrode in multilayer capacitors [26, 27].

The metallic pyrochlore layers are grown on (001)-oriented YSZ substrates. YSZ has a cubic-fluorite structure and its in-plane lattice constant is 5.12 Å. Thus, there is a ~2:1 mapping of the crystallographic dimensions of the YSZ to the pyrochlore. Similarly, there is a ~1:2 mapping of the crystallographic dimensions of the pyrochlore electrode to the HZO phase, as illustrated schematically in Figure 3.1(a). In this orientation, the pyrochlore layer forms an ideal structural and chemical template to seed the growth of [001] oriented layers in the HZO. For HZO, the different phases share similar lattice parameters (Table 3.1) [28]. With this as the basis, epitaxial heterostructures were synthesized using pulsed-laser deposition。

	a **(Å)**	***b*** **(Å)**	***c*** **(Å)**
monoclinic phase (β = 100.09°)	5.11	5.18	5.28
orthorhombic phase	5.23	5.03	5.05

Table 3.1. HZO lattice constant from literature [28]

3.3 Structural change of HZO versus film thickness

3.3.1 XRD evidence

A high-resolution X-ray diffractometer (Panalytical, X'Pert3MRD) was used to perform Bragg line scans. Copper K-alpha radiation was used for the X-ray diffraction measurements. All the XRD curves were calibrated by the substrate peak (5.12 Å,35.02°).

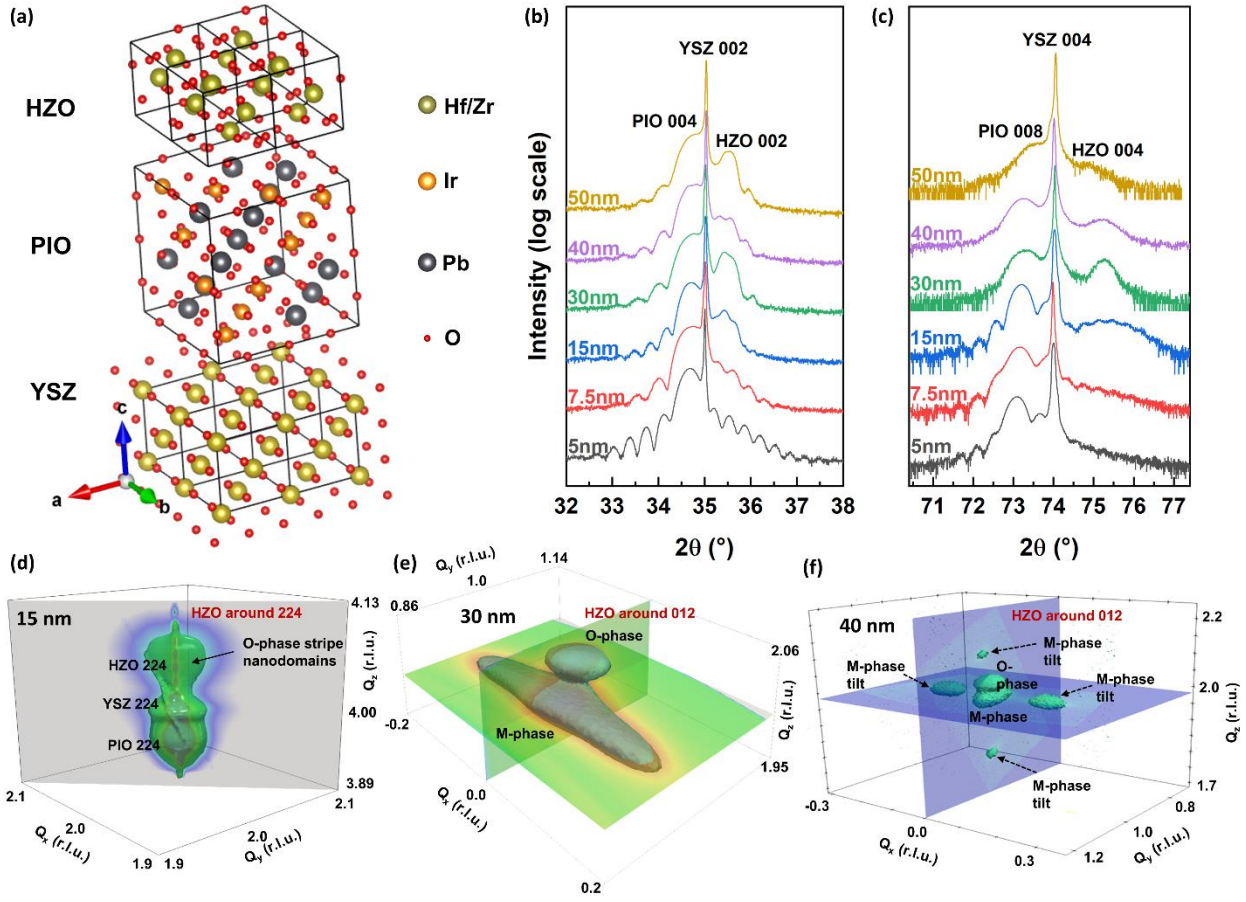

Figure 3.1. Thickness-dependent structural characterization using XRD & RSM. (a) Schematic of the lattice matching between the pyrochlore electrode, the substrate YSZ, and the HZO layer; (b) X-ray diffraction line scan about the (002) HZO peak for 5-50 nm HZO/ 20 nm PIO heterostructures; (c) is the corresponding scan around the (004) HZO peak; (d) Hard X-Ray reciprocal space mapping about the (224) YSZ peak for 15 nm HZO on 20 nm PIO; (e) Hard X-Ray reciprocal space mapping about the (012) HZO peak for 30 nm HZO on 20 nm PIO; (f) Hard X-Ray reciprocal space mapping about the (012) HZO peak for 40 nm HZO on 20 nm PIO.

X-ray diffraction Bragg scans from films where the HZO thickness varies from 5-50 nm (Figure 3.1 b,c) reveals a few important features. First, only 00l-type diffraction conditions are observed for both the electrode and HZO layers, with the latter exhibiting an out-of-plane lattice parameter of ~5.05 Å. If we only consider the phase formation from lattice mismatch minimization, the

orthorhombic phase (a,b, and c=5.23,5.03, and 5.05 Å in bulk) will tend to have its b or c axis oriented along the surface normal direction with an anisotropic strain from the substrate (2.1% compressive strain on a axis, 1.79% or 1.39% tensile strain on b or c axis); thus the out-of-plane c or b lattice parameter will expand by 0.1% and 0.3% to 5.055 Å and 5.045 Å, respectively, if the Poisson's ratio is taken to be 0.3 [31]. This assumption is validated by the X-ray diffraction data that yields an out-of-plane lattice parameter of 5.05 Å (Figure 3.1 b,c). Similarly, if the bulk monoclinic phase (a, b, and c=5.11, 5.18, and 5.28 Å; β=100.09°) were to form, it would tend to have its orthogonal a and b axes oriented in the plane of the film with only a uniaxial 1.16% compressive strain. We did not, however, distinctly observe the corresponding peak (which should appear at ~34.3°) in the X-ray diffraction patterns. That suggests the monoclinic phase is unlikely to be formed as the dominant phase in the orientation described above. However, given the similarity in the structure of the O-phase and the M-phase (with small differences in oxygen and Hf/Zr positions), the presence or absence of either phase cannot be uniquely identified by just Bragg scans, particularly for HZO film thicknesses of ~ 5nm.

We performed hard X-ray reciprocal space mapping (RSM) for the 15 nm, 30 nm, and 40 nm HZO samples (Figure3.1d, e, f) using the 20keV synchrotron X-ray source from Argonne National Laboratory 33-ID-B beamline. RSMs were obtained about several zone axes to obtain converging structural information. The reconstructed 3D reciprocal space data was generated using rsMap3D, while cuts along different directions are presented in the following Figures 3.2, 3.3, and 3.4 for 15nm, 30nm, and 40nm thick samples in detail.

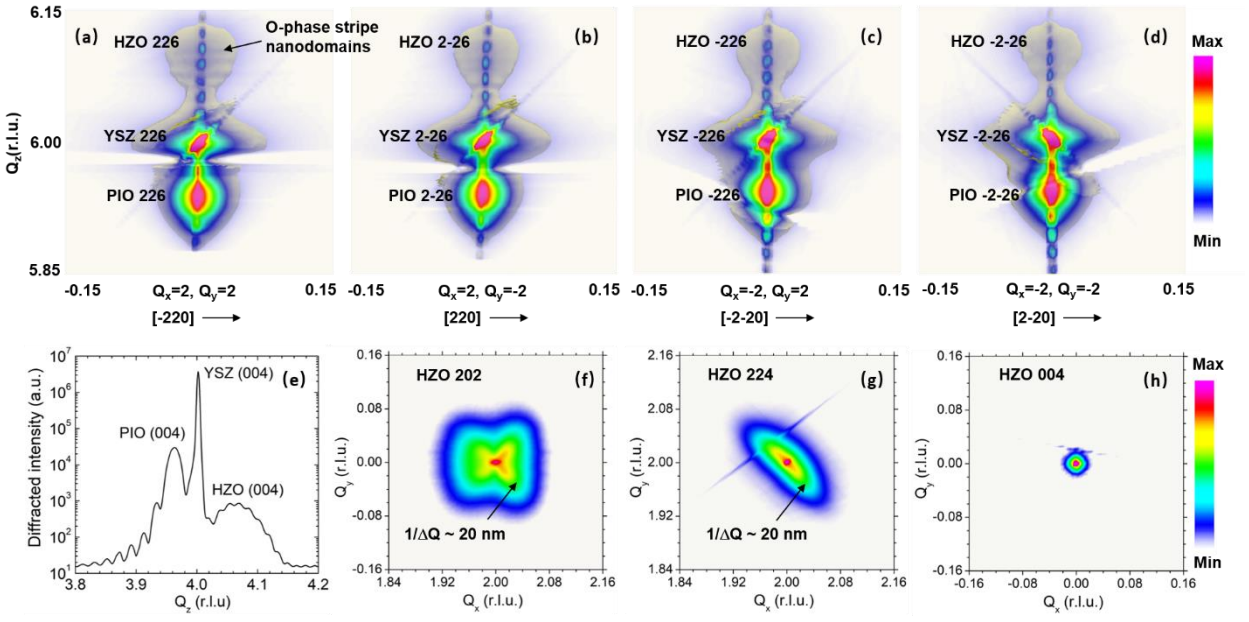

Figure 3.2. Hard X-ray reciprocal space mapping and Bragg scan of the 15 nm sample. (a)(b)(c)(d) are the 3D RSM images around the 226 YSZ peak for 15 nm HZO on 20 nm PIO. The multi-peaks of the o-phase indicate there are stripe nanodomains of o-phase in the 15 nm HZO film. (e) is the Bragg scan around the 004YSZ peak. (f)(g)(h) are the 2D RSM images around the 202HZO peak, the 224HZO peak and the 004HZO peaks respectively, showing the in-plane lattice information of HZO. The labeled nanodomain

scattering (with a periodicity of around 20nm) indicates o-phase domains with walls along in-plane [110] directions of the substrate.

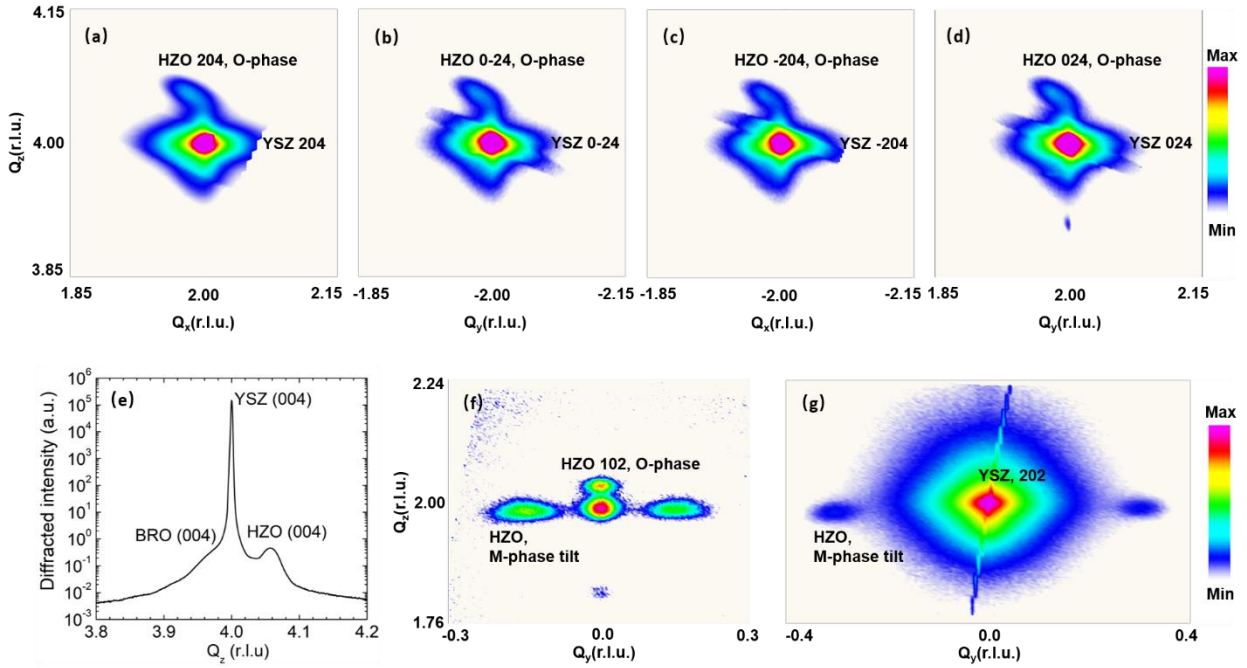

Figure 3.3. Hard X-ray reciprocal space mapping and Bragg scan of the 40 nm sample. (a)(b)(c)(d) are the 2D RSM images around the 204 YSZ peak for 40 nm HZO on 20 nm PIO. (f)(g) are 2D RSM around the 102HZO and the 202YSZ peaks respectively. Qx & Qy illustrate the in-plane structural information, in the meantime, Qz shows the out-of-plane information. The intensity of the o-phase peak near the YSZ peak decreases compared with that in the 15 nm sample. In contrast, separated peaks of m-phase show up. (e) Bragg scan also indicates the quality degradation in thicker films.

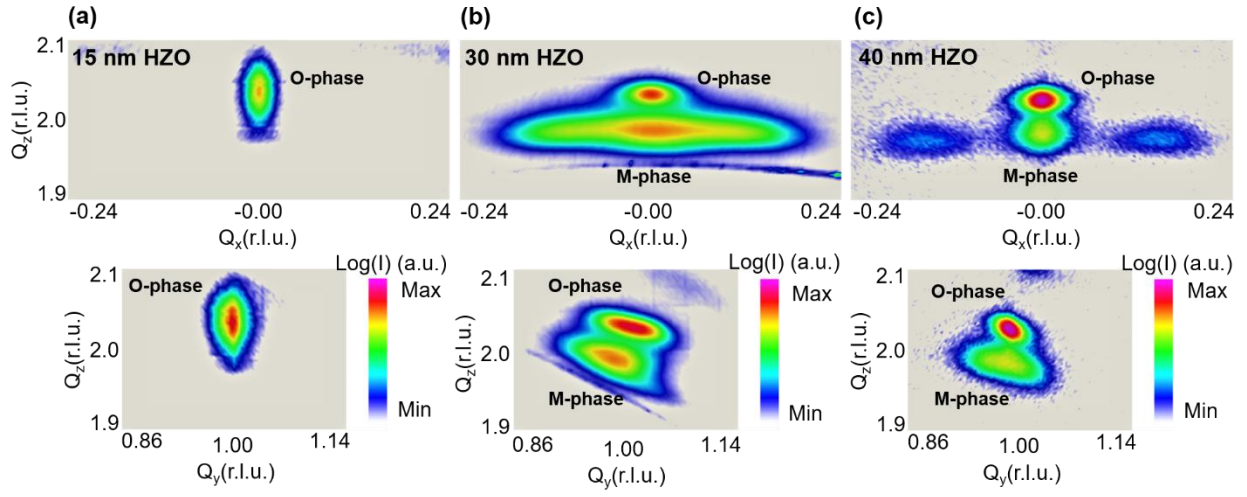

Figure 3.4. Hard X-ray 2D reciprocal space mapping around the 012 HZO peak for 15, 30 and 40 nm samples

3.3.2 TEM evidence

Atomic resolution dark field and bright field scanning transmission electron microscopy (STEM) images indeed confirm that the model structure of the tri-layer structure, shown schematically in Figure 3.5a, is indeed valid, illustrating the in-plane lattice matching between the PIO and HZO with a ~1:2 ratio. To understand the microscopic details of the phase stability in the HZO layer as a function of thickness [32], we carried out high-angle annular dark-field scanning transmission electron microscopy (HAADF-STEM) and bright-field STEM (BF-STEM) imaging in conjunction with detailed atomic-scale simulations for the PIO/HZO/PIO and SRO/HZO/PIO heterostructures with 5- and 30-nm-thick HZO layers.

For an HZO film thickness of 5 nm (Figure 3.5b), HAADF-STEM imaging reveals the epitaxy of the HZO layer sandwiched by the top and bottom PIO layers with sharp interfaces and demonstrates that the cation sublattice is fully epitaxial on top of the PIO layer. Nevertheless, unique identification of the crystal phase using only the cation sublattice can lead to ambiguity since there are other crystal structures that show a similar cation sublattice arrangement (such as the non-polar-orthorhombic Pbcm and monoclinic $P2_1/c$ phases, as illustrated in Figure 3.6). For example, although the monoclinic $P2_1/c$ phase has a different cation sublattice arrangement when compared to the orthorhombic $Pca2_1$ phase, the main difference within the similar cation sublattice arrangement between $Pca2_1$ and Pbcm phases is the oxygen ratio and location (as illustrated in Figure 3.6a-i, and Figure 3.6j-r). Here, due to the Z-contrast sensitivity, heavy atoms such as hafnium, zirconium, lead, and iridium can be easily imaged by HAADF-STEM, in contrast to light atoms such as oxygen.

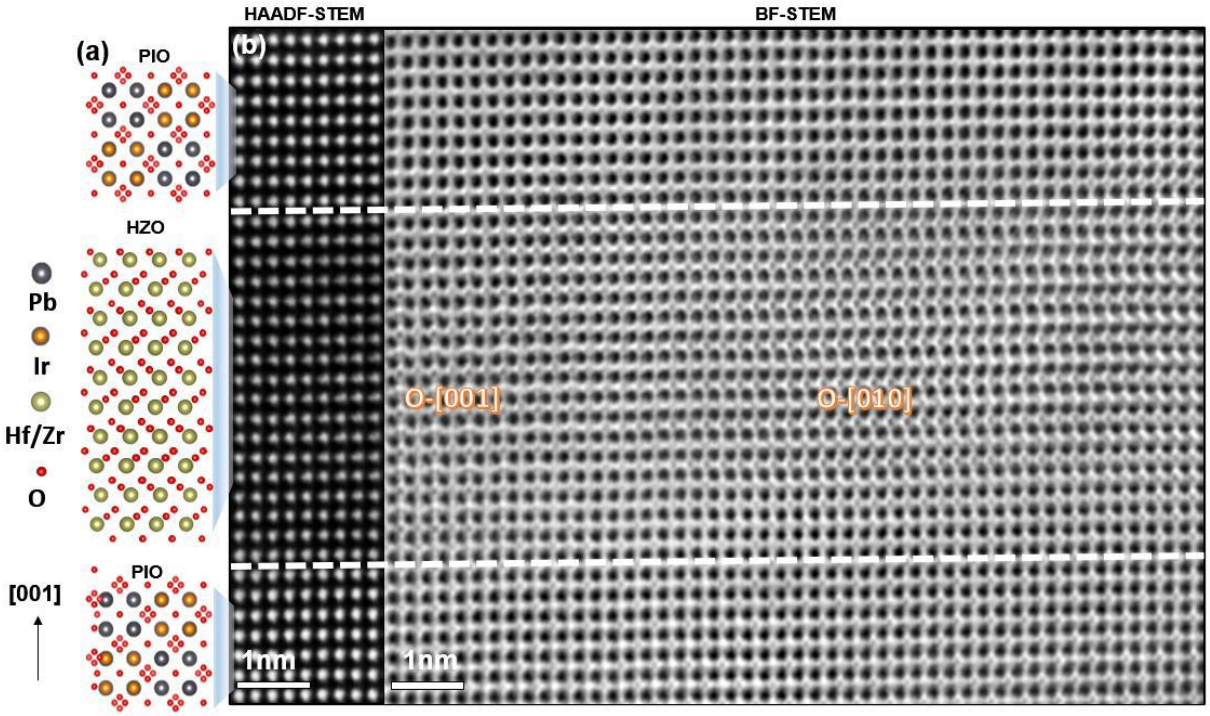

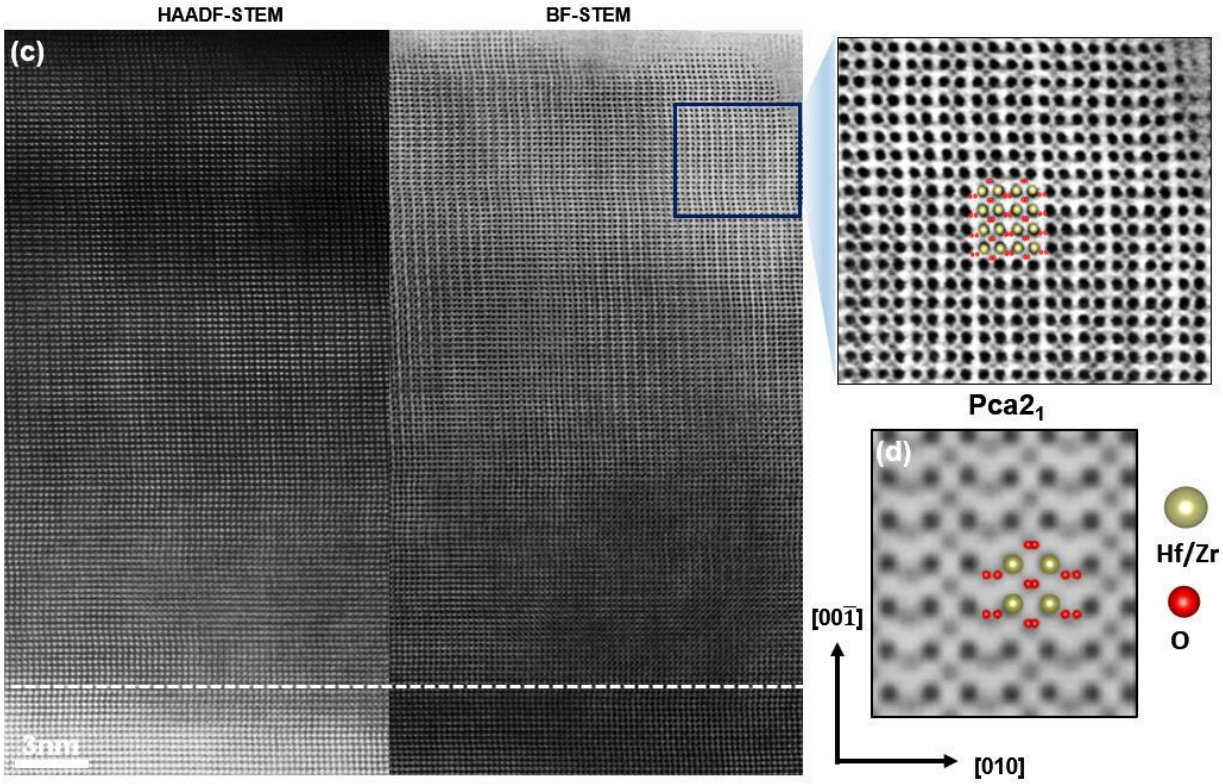
HAADF-STEM
BF-STEM
(c)
5nm
Pca2$_1$
(d)
Hf/Zr
O
[00$\bar{1}$]
[010]

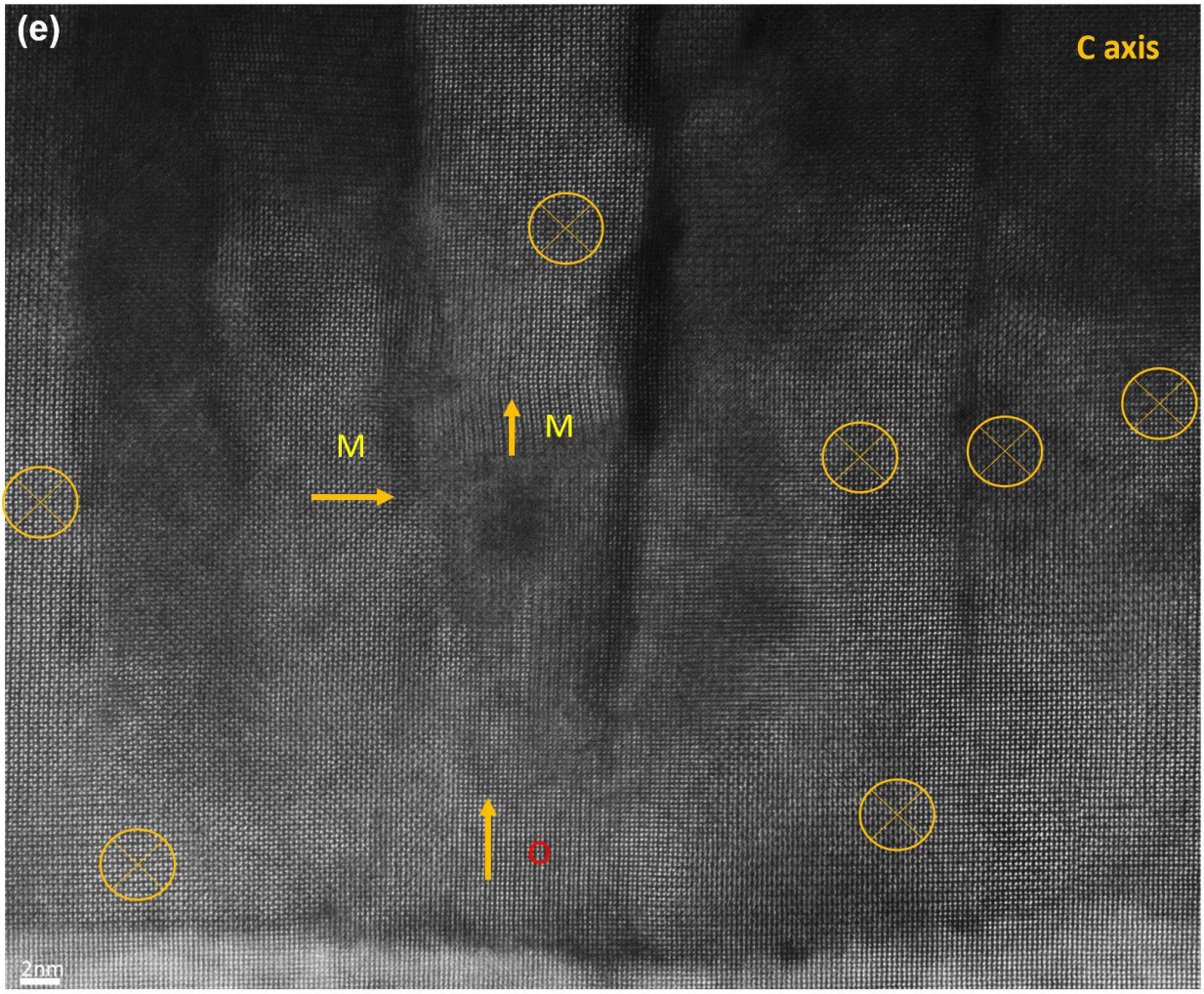

Figure 3.5. Direct imaging of polar structure using STEM. Schematic of the atomic structure (a) of the PIO/HZO/PIO heterostructure. Using HAADF/BF-STEM imaging, the ferroelectric phase in (b) epitaxial PIO/ HZO(5nm)/ PIO heterostructures and in (c) epitaxial SRO/ HZO (30 nm)/ PIO with high magnification of BF-STEM (d) Simulated STEM image of orthorhombic phase with space group symmetry of $Pca2_1$. (e) A HAADF -STEM image of the 50nm HZO sample showing the formation of monoclinic domains in the "finger" -like top portions of the film, while the regions near the electrode interface start off as the orthorhombic phase. Orange notation refers to the c-axis of HZO.

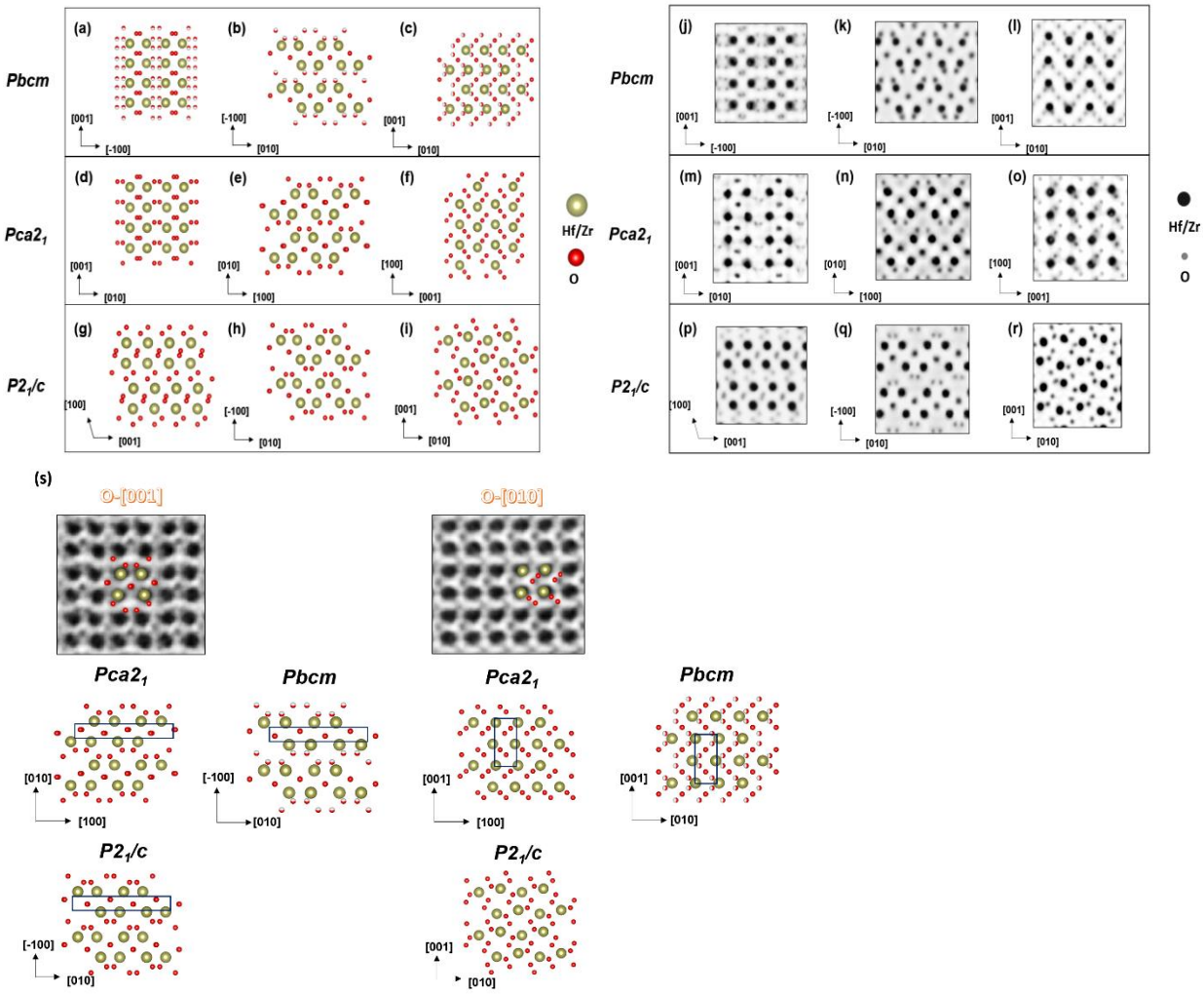

Figure 3.6. Comparison between the centrosymmetric Pbcm, non-centrosymmetric $Pca2_1$, and monoclinic $P2_1/c$ phases. Different orientations of the crystal structure of HZO in Pbcm, $Pca2_1$, and $P2_1/c$ HZO symmetry (a)-(i) corresponding to multislice simulation (j)-(r) showing the similar hafnium/zirconium sublattices and the differences of oxygen ratios and locations in (a)(d)(j)(m), (b)(e)(h)(k)(n)(q), and (c)(f)(l)(o). For example, double oxygens of horizontal zig-zag arrays in (e) compared to single oxygen in (b) and distinct oxygen positions in (a)(d) and (c)(f) can help identify the Pbcm or $Pca2_1$ phase with their similar hafnium/zirconium sublattices. Phase comparison between $Pca2_1$, Pbcm, and $P2_1/c$ in (s) to identify O- [001] and O- [010].

Therefore, to distinguish the non-centrosymmetric phase from other structurally similar centrosymmetric phases, BF-STEM imaging, in conjunction with image simulations, was employed to further resolve the oxygen anion positions and thus identify the symmetry accurately. As shown in Figure 3.5b (right), the oxygen sublattice of HZO demonstrates two regions (O- [001] and O- [010]) of the polar $Pca2_1$ phase and double oxygens in O- [001] and zig-zag oxygen arrays in O- [010] do not match with the non-polar Pbcm phase (Figure 3.6s). The image contrast for the

hafnium/zirconium and oxygen sublattices are in good agreement with the atomic model of the ferroelectric $Pca2_1$ phase, validated with image simulations (Figure 3.7). Besides, the experimental results do not match with the simulated image of the monoclinic $P2_1/c$ phase, because only M-[001] shows similar hafnium/zirconium sublattices with Pbcm and $Pca2_1$ phases. However, subtle differences such as a smaller spacing of zig-zag oxygen dumbbells and single oxygen of zig-zag array can be observed (Figure 3.6d-h).

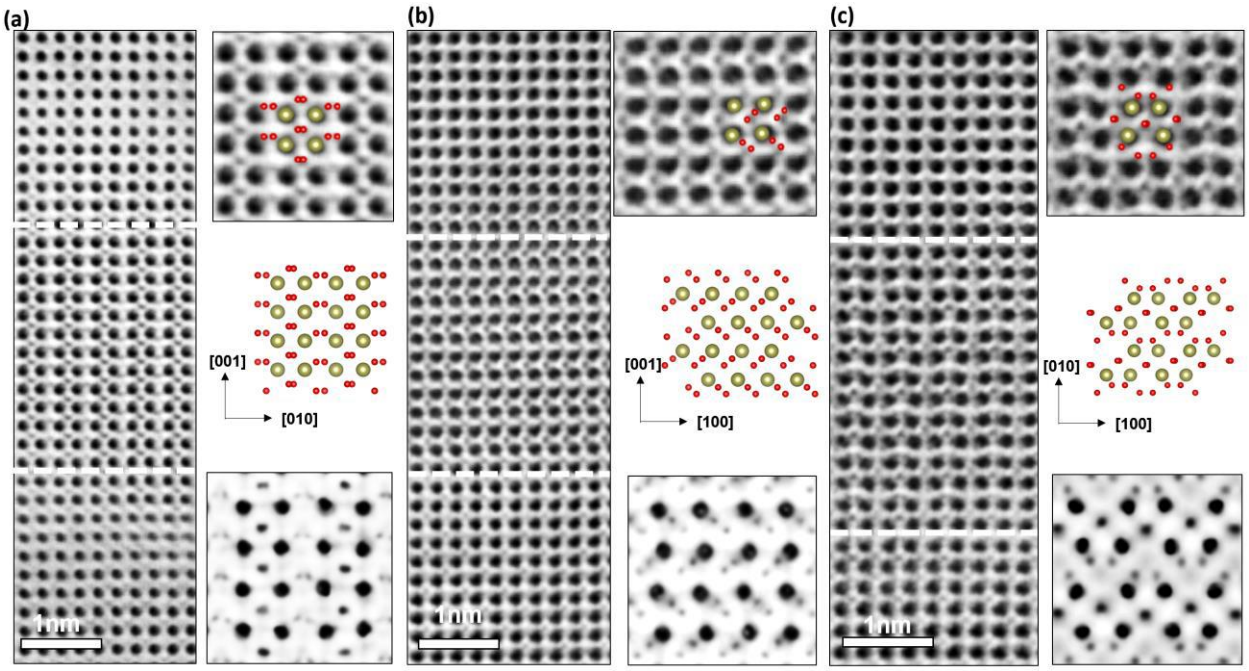

Figure 3.7. Ferroelectric O-phase with three variants in the 5 nm PIO/HZO/PIO heterostructure

Atomic scale HAADF- STEM imaging of HZO heterostructures demonstrates the co-existence of all three structural variants in the O-phase (Pca21 phase) with the electron beam along the (a) [100], (b) [010], and (c) [001] zone axes of the HZO film, respectively. Each zoom-in imaging of (a), (b), and (c) corresponds to their crystal structure and multislice simulation. This shows the formation of nanoscale polar domains in the HZO layer. According to Figure 3.6 comparison, these three zone axes of the HZO film are not $P2_1/c$ phase because hafnium/zirconium sublattices in Figure 3.6 d,g and f,i are totally different and subtle differences in Figure 3.6e,h such as double oxygens of horizontal zig-zag arrays and larger spacing of zig-zag oxygen dumbbells in Pca21 phase.

For the 30nm HZO film (Figure 3.7c), the HAADF-STEM image reveals that the hafnium/zirconium sublattices maintain the same orthorhombic structure as the 5 nm-thick HZO films. A minor fraction of the monoclinic $P2_1/c$ phase was also identified, and it coexists with the orthorhombic $Pca2_1$ phase in films of such thickness (Figure 3.8c); indeed, this appears to be very close to a critical thickness for the transition from the O-phase to the M-phase. The BF-STEM images reveal that the hafnium and oxygen sublattices are matched with the $Pca2_1$ phase atomic model. Importantly, STEM simulations (Figure 3.5d) using the Prismatic code [33, 34] compute the exact positions of hafnium and oxygen ions for the $Pca2_1$ phase along the [100] zone axis under

BF-STEM experimental conditions. The result matches closely with the HAADF and BF-STEM images. Perhaps the most interesting aspect of films of such thickness is the appearance of "finger-like" features near the electrode-HZO interface, which appears to be an indicator of the impending structural phase transition for thickness higher than ~30nm.

With a further increase in thickness to ~50 nm, the top portion of the HZO layer clearly shows the formation of "finger-like" features; these "finger-like" features can be identified as the monoclinic phase, which is now the dominant phase, identified through the atomic resolution images in Figure 3.5e, and elaborated in Figure 3.8a, b. Hence, the ferroelectric $Pca2_1$ phase, that can be stabilized through epitaxy, progressively converts into the monoclinic phase as the HZO layer thickness is increased.

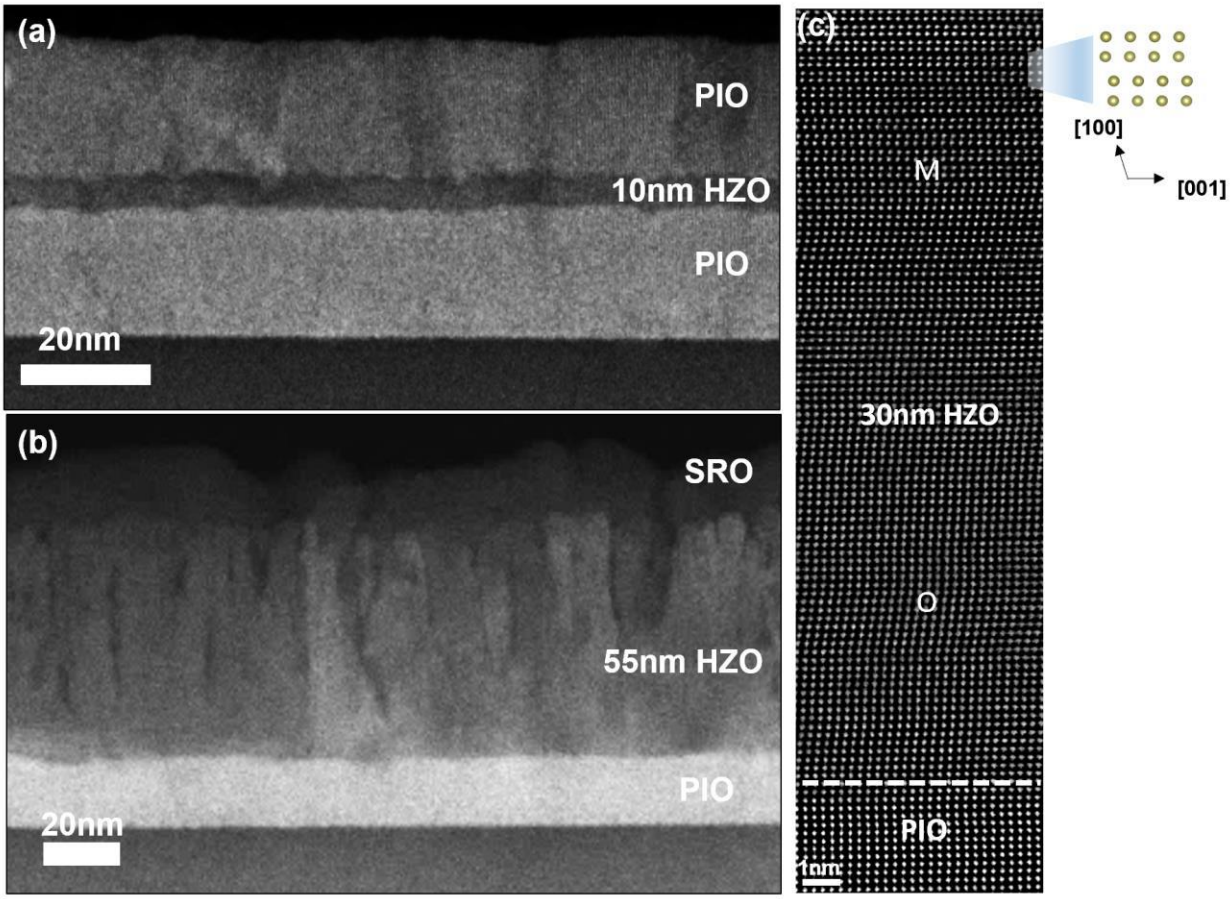

Figure 3.8. Thickness dependence of HZO morphology and two-phase coexistence in epitaxial HZO heterostructures cross-section TEM images of the 10 nm HZO heterostructure compared to that with ~55 nm HZO thickness: (a) 10 nm, showing a relatively smooth HZO interface, although the early stages of surface rumpling are already evident in this image; (b) 55 nm HZO film, where the "finger-like" features in the HZO layer is very clear. A monoclinic P21/c crystal structure can be identified using the HRSTEM images of the hafnium/zirconium sublattices; (c) shows the coexistence of the O-phase with the M-phase; the O-phase is predominantly observed at the electrode-HZO interface, suggesting that the initial stages of nucleation occur as the O-phase, which subsequently changes such as uneven tilting over to the M-phase, which likely nucleates at the surface. The dotted line is an approximate location of the interface.

3.3.3 Theoretical calculations

To understand why the polar-orthorhombic phase is stable in our epitaxial films, especially the thinner films, we analyzed the phase stability and coexistence of the non-polar-monoclinic and polar-orthorhombic phases of HZO using a simple thermodynamic model. Three energy contributions were considered towards the total Gibbs free energy: the Helmholtz free energy $U-TS$ (where U is the enthalpy, T is the absolute temperature, and S is the entropy), the surface energy (γ), and the elastic-strain energy ($1/2\Sigma_{\sigma i \varepsilon ii}$) as:

$$G = U - TS + \mathrm{A}\,\gamma + \frac{1}{2}V \cdot \sum_i \sigma_i \varepsilon_i$$

We set the Helmholtz free energy of the M-phase at 300K to 0, and the O-phase is 48 meV/f.u. [28] The surface energy, and the lattice parameters of the polar-orthorhombic and non-polar-monoclinic phases were obtained from published values (Refer to Table 3.2, 3.3 and below sections for details).

The elastic strain energy

In thin films, the source of stress is from the in-plane elastic strain that the substrate applies to the thin film layer, while the out-of-plane direction is free. For a film structure with orthogonal in-plane axis for all layers, we can only consider the three normal stresses σ_x, σ_y, σ_z, which can be calculated by:

$$\sigma_i = \frac{E}{(1-2\nu)(1+\nu)}[(1-\nu)\varepsilon_i + \nu(\varepsilon_j + \varepsilon_k)]$$

Where $\varepsilon i,j,k$ is the lattice mismatch between the substrate and film layer in three directions, ν and E are Poisson's ratio and Young's modulus of the film material. Here we set the z direction as the out-of-plane direction, εx and εy are two in-plane mismatch ratios that can be obtained directly from the lattice parameters. Because σ_z=0, we can get ε_z, then σ_x and σ_y. The ν and E values we used are from the materials project [31] The lattice parameter of the cubic YSZ substrate is 5.12 Å, while that of the HZO m- and O-phase are summarized below in Table 3.2 from different computational and experimental results in the literature for the hafnia/zirconia system.

	a (Å)	b (Å)	c (Å)	Ref.
M-phase	5.11	5.18	5.28	[28]
	5.11	5.16	5.28	[28]
	4.95	5.06	5.08	[44]
	5.14	5.20	5.31	[45]
	5.12	5.19	5.28	[46]
	5.11	5.20	5.28	[28]
	5.09	5.20	5.24	[44]
	5.142	5.195	5.326	[31]
	5.234	5.268	5.418	[31]
O-phase	5.23	5.03	5.05	[28]
	5.22	5.04	5.05	[28]
	5.07	4.88	4.89	[44]
	5.29	5.01	5.08	[45]
	5.11	4.90	4.92	[46]
	5.24	5.04	5.05	[28]
	5.22	5.02	5.04	[44]
	5.269	5.04	5.074	[31]
	5.349	5.132	5.159	[31]

Table 3.2. Lattice constants of HZO m- and O-phase from various sources

The role of surface energy

The surface energy plays an important role in the total Gibbs free energy. Here we only count the interface of the HZO/top electrode or HZO/air in our thin film system. Thus, the surface energy per unit volume $A\gamma V=\gamma/h$ is inversely proportional to the film thickness. We searched the reported surface energy for both m- and O-phase in the chart below.

	γ (J/m^2)	Ref.		γ (J/m^2)	Ref.
M-phase	3.2	[28]	O-phase	2.575	[28]
	3.4	[28]		3.15	[28]
	3.0	[28]		2.0	[28]
	3.7	[47]		1.03	[48]
	2.8	[47]		1.23	[48]
	3.45	[48]		2.1	[49]
	2.86	[48]			
	6.4	[49]			

Table 3.3. Surface energies of HZO m- and O-phase from various sources

Since there is a diversity of such values, we considered all possible combinations of lattice parameters and surface energies, which give rise to the free-energy bands for the monoclinic and orthorhombic phases. Figure 3.9a shows the Gibbs free energy per unit volume of the non-polar-

monoclinic and polar-orthorhombic phases versus film thickness and gives an intuitive impression of the phase stability as a function of film thickness. The first important conclusion is that the polar-orthorhombic phase is more stable in thinner films since the surface energy of the orthorhombic phase is lower than that of the monoclinic phase. When the film gets thicker, the monoclinic phase gets more stable, primarily as a consequence of the strain-energy contribution increasing and the surface-energy contribution decreasing with film thickness. This is consistent with the experimental data, i.e., thinner samples have pure orthorhombic structure, while the monoclinic phase starts to grow in fraction as the sample gets thicker. In ~50-nm-thick films, we barely observe any orthorhombic phase, and what little is observed is found at the electrode-HZO interface.

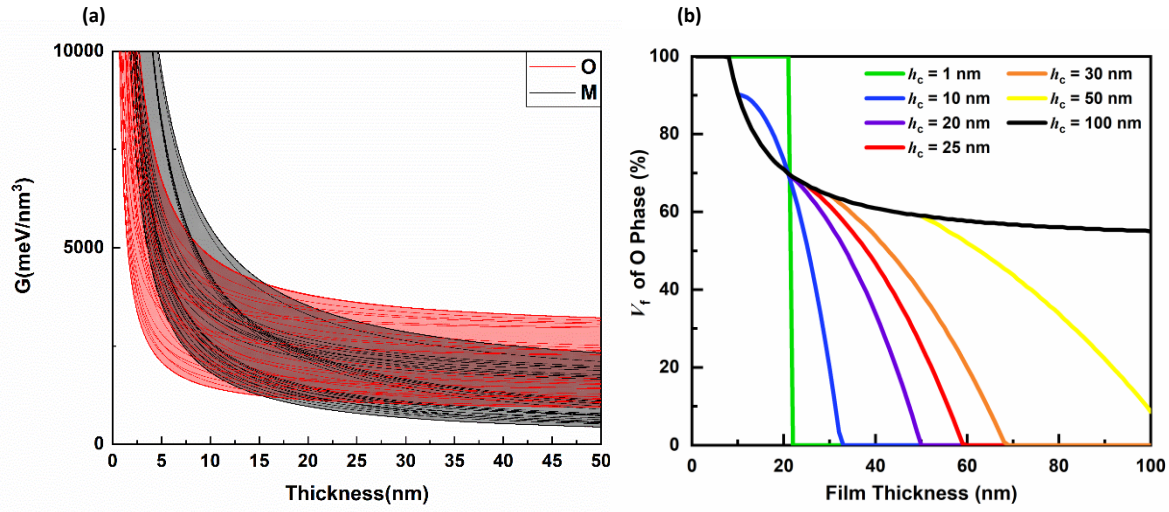

Figure 3.9. Thermodynamic calculations of thickness-dependent stability of m- and polar O-phases. (a) Gibbs free energy bands of m- and polar O-phase as a function of film thickness at room temperature for epitaxial HZO films calculated based on all possible parameters from the literature. (b) Simulation of the volume fraction of the polar O-phase as a function of film thickness at room temperature with different strain relaxation critical thicknesses.

Realizing that the film thickness is a key parameter, we further computed the energetics of a coexistence state of the monoclinic and orthorhombic phases as a function of thickness (Figure 3.9b). Both the RSM and STEM data reveal that the strain from the substrate gets relaxed in thicker films. Thus, we considered the strain relaxation because of the dislocations in the calculation of Figure 3.9b. The effective misfit strain as a function of thickness is evaluated using the Matthews-Blakeslee criterion:

$$\varepsilon(h) = 1 - \frac{1-\varepsilon_0}{1-\varepsilon_0\left(1-\frac{h_c}{h}\right)}$$

where h is the film thickness and h_c is the Matthews–Blakeslee (MB) critical thickness for dislocation formation [30]. These calculations were performed as a function of h_c, the critical

thickness, as shown in Figure 3.9b, to estimate the volume fraction of the orthorhombic phase as a function of thickness and to illustrate the effects of strain relaxation on the relative stability of the two phases. When h_c=1 nm, i.e., the strain was relaxed by dislocation formation at this thickness, the vertical line shows that the orthorhombic phase and monoclinic phase cannot coexist in the sample. The polar orthorhombic phase disappears in thicker samples. On the contrary, in the scenario of h_c=100 nm, i.e., the film is coherently strained until this thickness, the orthorhombic phase volume fraction asymptotically drops to ~60% at this limit but is still stable. For critical thicknesses in between, the orthorhombic phase volume fraction will drop to zero at a thickness that is directly related to the critical thickness. Relating this to our experimental results, the critical thickness h_c is estimated to be ~25 nm. Increasing the critical thickness by eliminating the dislocations in samples will help the polar orthorhombic exist in thicker films.

3.4 Piezoelectric and ferroelectric behavior

When probing the polar order in ultra-thin films such as those being studied in this study, it is critical to ensure that the effects of leakage are accounted for and eliminated. Therefore, we used a combination of voltage-dependent piezoelectric susceptibility measurements in a capacitor geometry (which should be less susceptible to leakage effects) coupled with piezoresponse force microscopy (PFM) of the exposed HZO followed by conventional polarization-voltage measurements. Portions of the exposed HZO surface were poled with opposite polarity voltages and imaged using PFM, an example of which is shown (Figure 3.10a, b) for a 10 nm-thick HZO film. The amplitude image (Figure 3.10a) shows a strong piezoelectric response, while the corresponding phase image (Figure 3.10b) shows a 180° change in the phase of the output signal, indicating that the polarization state has been switched by a corresponding angle by the opposite polarity voltage. These PFM images are stable for well over 24 hours, indicating the ferroelectric origin of the image contrast.

In order to probe the switching behavior quantitatively, we applied a DC voltage to 12.5μm-diameter, 30 nm $SrRuO_3$ (SRO) / 5, 10, 15, and 30 nm HZO / 20 nm PIO capacitors in the PFM and obtained piezoelectric phase/amplitude versus DC field loops for samples with different thicknesses. Circular top electrodes (diameter 12.5μm) were fabricated using a wet etching method. Due to the ease of a simple wet etch process, for these measurements we used a $SrRuO_3$ (SRO) top electrode. First, the photoresist was patterned on the as-grown heterostructures using photolithography, which only covers the circular electrode regions. The rest region of the top SRO was etched away within 1 min under ~0.02 mol/L $NaIO_4$, leaving circular SRO contacts covered by the photoresist. Subsequently, the photoresist was removed by an acetone rinse.

Piezoelectric hysteresis loops (both phase and amplitude as a function of applied DC voltage) were obtained both for the capacitor geometry as well as for the bi-layer structure (i.e., no top electrode). The piezoelectric response [35] was measured using a standard test protocol, at room temperature using a scanning probe microscope (Asylum MFP-3D), in which an ac-voltage signal is fed onto the cantilever and induces a piezoelectric response from the ferroelectric surface which is then picked up using a lock-in technique. A square wave DC bias was applied with a pulse width varying from 0.01s to 1s that steps up/down in magnitude with time (schematically illustrated in Figure

3.10c). It is noteworthy that the effective frequency of this triangular-shaped pulse profile is of the order of a few Hz, as illustrated in Figure 3.10b. Piezoelectric responses were measured both at the top of the DC pulse (ON-state) as well as at the bottom of the DC pulse (OFF-state).

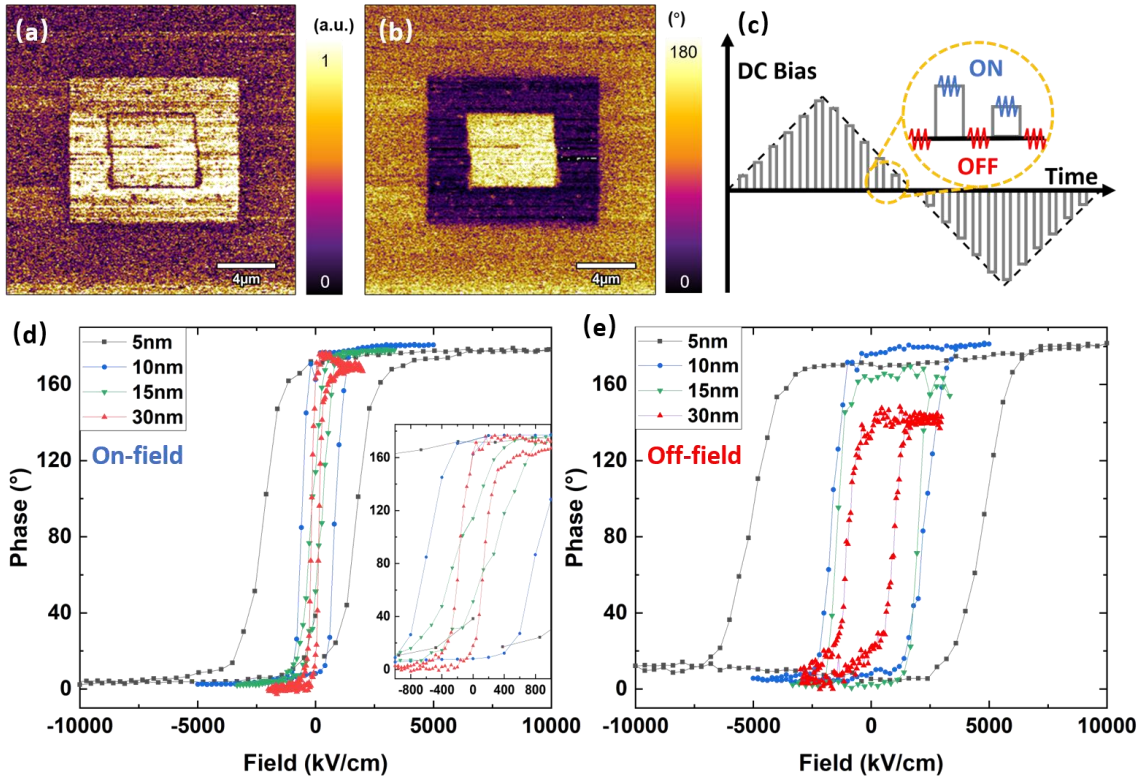

Figure 3.10. Piezoresponse force microscopy measurements. Piezoresponse force microscopy image written by an AFM tip on 10 nm HZO/ 20 nm PIO heterostructure, (a) amplitude signal and (b) the corresponding phase signal; Piezoresponse loops measured on 30 nm SRO/ (5,10,15,30) nm HZO/ 20 nm PIO heterostructure capacitors, (c) Schematic illustration of the DC pulses and the ON/OFF measuring modes (d) measured at the top of DC bias pulse (ON) (e) measured at the bottom of the DC bias pulses (OFF).

Figure 3.10d&e summarize the piezoelectric phase vs. DC field plots for films of varying thickness in both ON- and OFF-field modes. We do observe a decrease in the coercive field as the HZO thickness increases, which is generally consistent with the expected dependence of EC on thickness (d) [36, 37]; however, since the thickness range is quite limited, we are able to draw only qualitative conclusions about such scaling. However, an intriguing observation is the marked difference in coercive field between the ON-state and OFF-state measurements. The coercive field in the OFF-state measurement is still much higher (~1 MV/cm) than what is well-known for perovskite-based ferroelectrics [38] and is consistent with prior reports for HZO [3]. However, the coercive field in the ON-state measurement is ~3-5 times smaller for the same capacitor; specifically, the 30nm thick film shows an ON-state coercive field of about 200kV/cm.

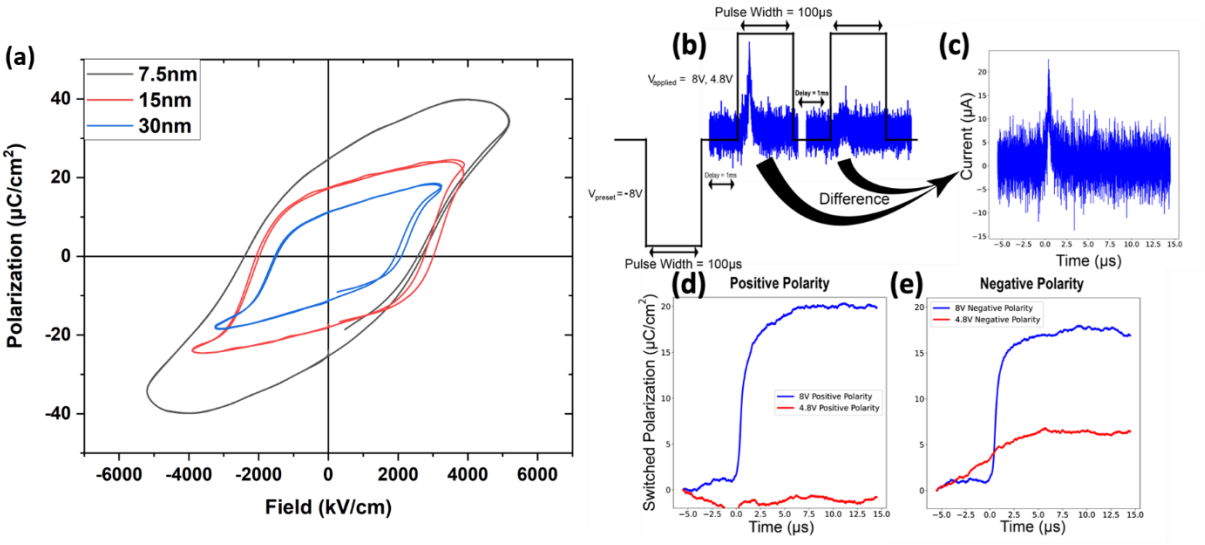

Figure 3.11. Ferroelectric measurements on SRO/HZO/PIO capacitors. (a) The polarization vs. field hysteresis loops measured at a test frequency of 100kHz on 30 nm SRO/ (7.5,15,30) nm HZO/ 20 nm PIO heterostructure capacitors with 12.5μm diameter; (b) Test voltage profile (Black) and current response (Blue) measuring the polarization of the test capacitors; (c) A typical switching current vs. time response, calculated as the difference in current response between the switching and non-switching pulses (first and second "up" pulses, respectively, in (b)); (d) 30 nm SRO/ 30 nm HZO/ 20 nm PIO heterostructure capacitor switched polarization vs. time (integration of switching current) at 4.8V and 8V applied, measured in both positive and negative polarity; (e) Switched polarization vs. time at 4.8V and 8V in the negative polarity. The polarity refers to the pulse sequence being applied to either the top or bottom electrode.

To probe the remnant polarization (P_r) we carried out polarization (P)-electric field (E) hysteresis loop and pulsed polarization measurements on the same set of capacitors (Figure 3.11a-e). The measurements were completed at room temperature using a Precision Multiferroic Tester (Radiant Technologies). As we expected, measurements below a thickness of 7.5 nm were compounded with leakage due to the macroscopic size of the capacitors; for the same reason, polarization hysteresis loops were measured at 100kHz to minimize resistive leakage. The remnant polarization of the 7.5-nm-thick film reaches a value of ~30 μC/cm^2. The theoretical P_r of the (001)-oriented orthorhombic phase of hafnia could be as large as 51-53 μC/cm^2.[6] For a 30 nm HZO film, we observe a measurable ferroelectric state (consistent with the TEM studies) with a P_r≈10 μC/cm^2. Beyond this thickness, we observe a progressive conversion into the M-phase, again consistent with the STEM observations, Figure 3.5e. This result can be put into context with published results for HZO on commonly used electrodes; for example, P_r was nearly zero for TiN/HZO/TiN thicker than ~20-25 nm.[14, 29] The coercive voltage measured at this frequency of 100kHz is higher than what is observed in the piezoelectric phase loops for the same capacitor (Figure 3.10d, e), illustrating the frequency dispersion in the switching voltage. The polarization switching response was measured under pulsed probing conditions, which is schematically illustrated in Figure 3.11b. A preset pulse polarizes the material into a uniform polarization state, whereafter two sequential, identical probe pulses, first switch the polarization and then measure directly the non-switching (dielectric) response of the material. Thus, we are able to determine the displacement current

contribution from polarization switching alone by subtracting the non-switching response from the switching response. This so-called switching current transient is illustrated in Figure 3.11c. Upon integrating this switching current transient, one obtains the switched polarization as a function of time, for two different nominal voltages of 8V and 4.8V, and for both positive and negative polarities. These pulsed switching studies show a robust switched polarization for films up to 30nm in thickness.

Field cycling performance of 30nm-thick HZO devices

Since the electrical current leakage of HZO/PIO devices cannot be eliminated, the field cycling data of this system is difficult to obtain. Figure 3.12 shows the field cycling data of the 30nm-thick samples below. We applied a triangular wave with 10V as the peak voltage at 1MHz to cycle on 5um-in-diameter devices. The device shown in Figure 3.12 was shorted and damaged after 10^7 voltage cycles. Thus, as the data indicated, the epitaxial HZO thin films deposited on the PIO electrode don't have obvious polarization fatigue behavior up to 10^7 cycles.

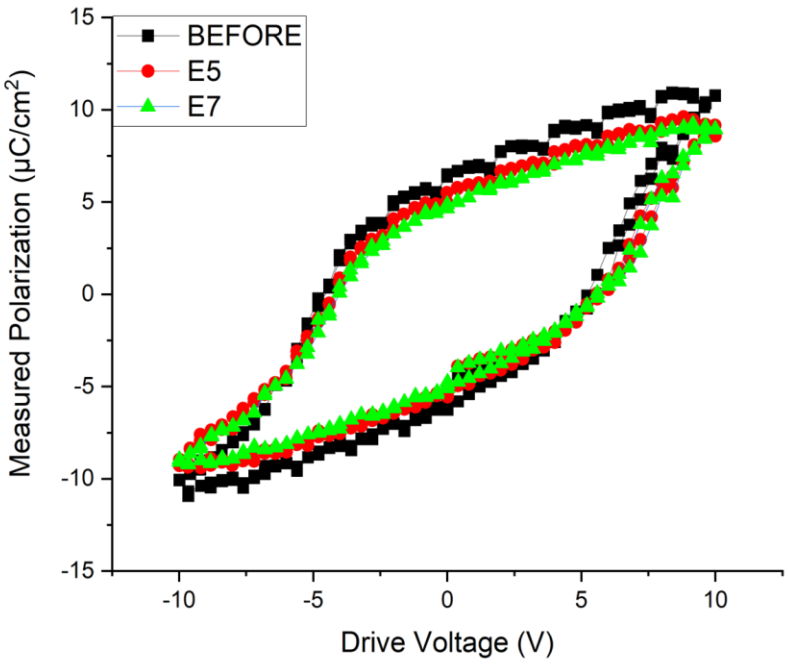

Figure 3.12. Bipolar Field cycling behavior of SRO/30nm HZO/PIO capacitors

3.5 limitations of PLD-grown pyrochlore electrodes

The HZO/PIO devices experience significant leakage issues primarily due to the high surface roughness of PIO. This roughness stems from the PIO target's lower density and hardness compared to typical PLD oxide targets. When the PIO target is ablated by a high-energy laser beam, it tends to eject small particles, adversely affecting deposition and surface quality. Figure 3.13a demonstrates the PIO film's surface topology on YSZ substrates, where the roughness can span several nanometers due to particle ejection during deposition. The substantial roughness, evident in Figure 3.13c's depiction of a wavy interface with up to 5nm local height variations, poses a significant risk. Considering the HZO layer's thinness (~10nm), the film is highly susceptible to breakdown at these rough spots, especially under several volts of applied voltage. In larger scales, capacitors with a 5um diameter may encounter hundreds of such particles, substantially increasing short-circuit risks.

Figure 3.13b provides additional insights into PIO's deposition mode, through a Reflected High Energy Electron Diffraction (RHEED) diffraction pattern captured during PLD deposition of PIO. Ideally, a 2D deposition mode would result in stripe patterns, but the observed dot pattern here suggests a 3D/island growth mode, indicating that deposition is not occurring in the preferred layer-by-layer manner.

Another challenge comes from thermal budget. The best deposition temperature for pyrochlore films on PLD should be around 550 ~600°C while the temperature for best HZO quality is over 700°C. Both sides need compromise to get better overall quality for the whole stack. The higher deposition temperature can further degrade the PIO crystallization and interface quality.

Given that pyrochlore's softness is ill-suited for laser ablation and the inconsistency of suited deposition environment, alternative deposition methods for these HZO/pyrochlore material systems must be explored, particularly for studies involving electrical measurements.

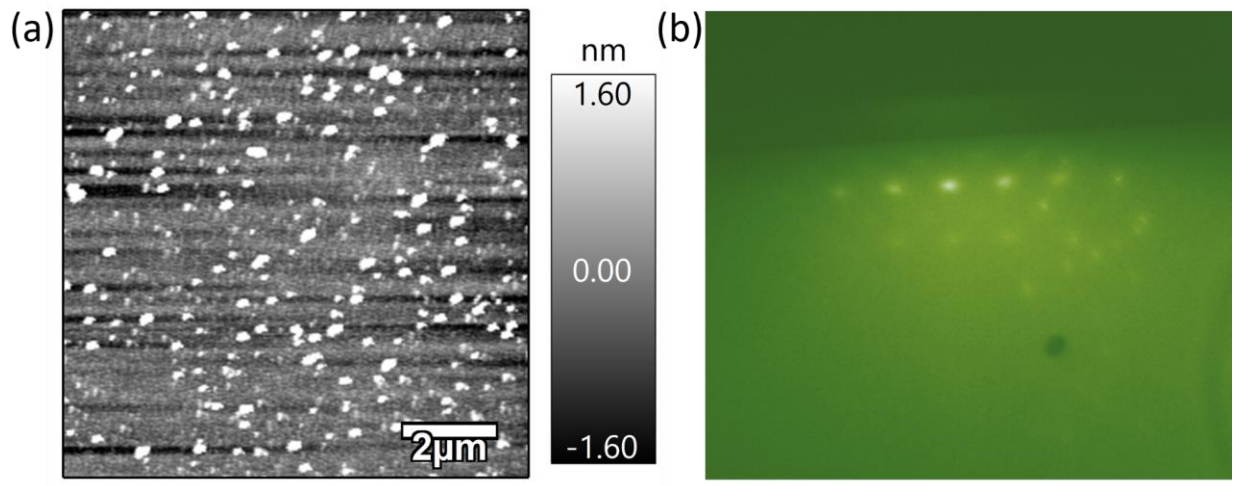

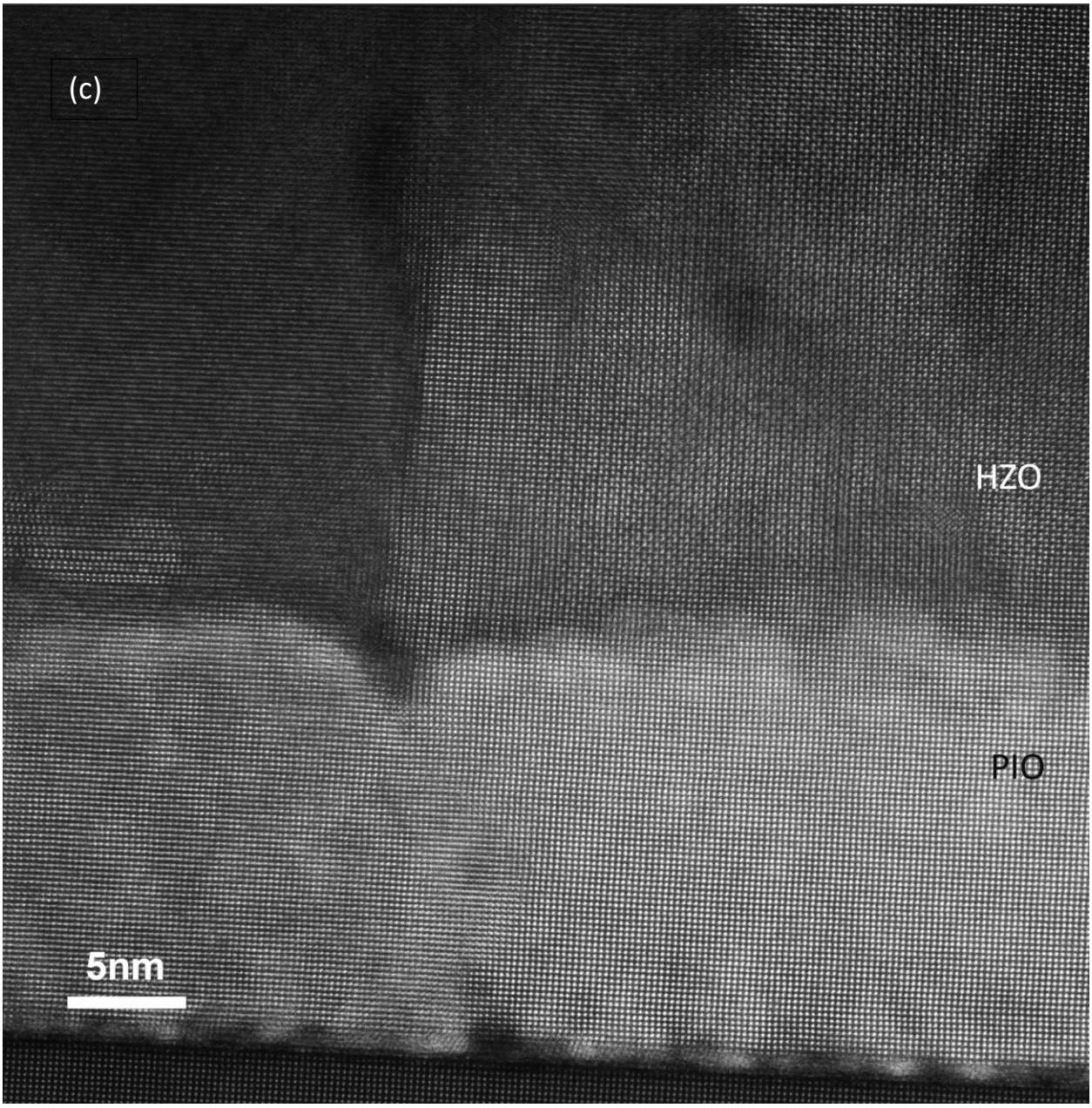

Figure 3.13. PIO surface roughness. (a) AFM image of PIO film surface. (b) RHEED pattern during PIO deposition. (c) STEM image zoom-in the interface of HZO/PIO bi-layer.

The work presented in this chapter clearly points to the role of epitaxial strain and surface energy in stabilizing the polar O-phase; relaxation of the misfit strain with film thickness emerges as a key element in destabilizing the polar-orthorhombic phase in favor of the non-polar-monoclinic phase. This also points to the possibility of further stabilizing the polar-orthorhombic phase at larger film thicknesses by epitaxial constraint, for example by using a bottom electrode that imposes a smaller lattice mismatch strain (and thus increasing the h_c value). It is equally interesting to note from the STEM images of the thicker HZO layers (i.e., > 30 nm) that the interface between the polar-orthorhombic phase and the non-polar monoclinic phase is rather diffuse (i.e., it does not

appear to be a consequence of a diffusion-less, shear transformation, as, for example, in martensites [50]). Instead, the diffuse nature of this interface indicates a possible order-disorder type of phase transition from the polar-orthorhombic phase to the non-polar-monoclinic phase. Thus, one possible pathway to prevent the formation of the non-polar-monoclinic phase could be the rate of cooling from the deposition temperature to prevent such diffusional processes.

In conclusion, we have demonstrated epitaxial stabilization of the polar orthorhombic HZO phase using a new lattice-matched bottom electrode PIO at a film thickness of ≤ 30 nm. Atomic resolution STEM images for these epitaxial films directly show the phase evolution as a function of film thickness and provide an ideal way to further study the switching pathway and the possible electric-field-induced phase transformation. Thermodynamic calculations reveal the critical role of epitaxial strain and surface energy in stabilizing the orthorhombic phase over the monoclinic phase. Thus, it appears that further tuning of the phase space through such an epitaxial stabilization process could lead to the orthorhombic phase being stable over an even larger thickness range, which may further help in reducing the switching field. The HZO/PIO material system presents an excellent opportunity for deeper exploration into the intrinsic properties of HZO, thanks to its perfect epitaxial quality. Addressing the limitations arising from interface quality, as described earlier, is crucial. We aspire that this work will stimulate further research and advancements in this material system.

References

[1] U. Schroeder, C. S. Hwang, H. Funakubo, Ferroelectricity in doped hafnium oxide: materials, properties and devices, Woodhead Publishing, 2019.

[2] P. Nukala, J. Antoja-Lleonart, Y. Wei, L. Yedra, B. Dkhil, B. Noheda, Acs Appl Electron Mater 2019, 1, 2585.

[3] Y. Wei, P. Nukala, M. Salverda, S. Matzen, H. J. Zhao, J. Momand, A. S. Everhardt, G. Agnus, G. R. Blake, P. Lecoeur, B. J. Kooi, J. Iniguez, B. Dkhil, B. Noheda, Nat Mater 2018, 17, 1095.

[4] S. Clima, S. R. C. McMitchell, K. Florent, L. Nyns, M. Popovici, N. Ronchi, L. D. Piazza, J. V. Houdt, G. Pourtois, "First-Principles Perspective on Poling Mechanisms and Ferroelectric/Antiferroelectric Behavior of Hf1-xZrxO_2 for FEFET Applications", presented at 2018 IEEE International Electron Devices Meeting (IEDM), 1-5 Dec. 2018, 2018.

[5] T. S. Böscke, J. Müller, D. Bräuhaus, U. Schröder, U. Böttger, Applied Physics Letters 2011, 99, 102903.

[6] M. H. Park, H. J. Kim, Y. J. Kim, T. Moon, C. S. Hwang, Applied Physics Letters 2014, 104, 072901.

[7] M. H. Park, Y. H. Lee, H. J. Kim, Y. J. Kim, T. Moon, K. D. Kim, S. D. Hyun, T. Mikolajick, U. Schroeder, C. S. Hwang, Nanoscale 2017, 10, 716.

[8] T. Maeda, B. Magyari-Kope, Y. Nishi, "Identifying Ferroelectric Switching Pathways in HfO_2: First Principles Calculations under Electric Fields", presented at 2017 IEEE International Memory Workshop (IMW), 14-17 May 2017, 2017.

[9] B. Johnson, J. L. Jones, Ferroelectr Doped Hafnium Oxide Mater Prop Devices 2019, 25.

[10] J. Lowther, J. Dewhurst, J. Leger, J. Haines, Physical review B 1999, 60, 14485.

[11] M. H. Park, T. Schenk, U. Schroeder, Ferroelectr Doped Hafnium Oxide Mater Prop Devices 2019, 49.

[12] E. D. Grimley, T. Schenk, T. Mikolajick, U. Schroeder, J. M. LeBeau, Advanced Materials Interfaces 2018, 5, 1701258.

[13] M. H. Park, T. Schenk, C. S. Hwang, U. Schroeder, Ferroelectr Doped Hafnium Oxide Mater Prop Devices 2019, 341.

[14] M. H. Park, Y. H. Lee, H. J. Kim, T. Schenk, W. Lee, K. D. Kim, F. P. G. Fengler, T. Mikolajick, U. Schroeder, C. S. Hwang, Nanoscale 2017, 9, 9973.

[15] T. Shimizu, K. Katayama, T. Kiguchi, A. Akama, T. J. Konno, O. Sakata, H. Funakubo, Sci Rep-uk 2016, 6, 32931.

[16] T. Shimizu, K. Katayama, T. Kiguchi, A. Akama, T. J. Konno, H. Funakubo, Applied Physics Letters 2015, 107, 032910.

[17] S. Migita, Y. Morita, W. Mizubayashi, H. Ota, "Preparation of epitaxial HfO_2 film (EOT=0.5 nm) on Si substrate using atomic-layer deposition of amorphous film and rapid thermal crystallization (RTC) in an abrupt temperature gradient", presented at 2010 International Electron Devices Meeting, 6-8 Dec. 2010, 2010.

[18] S. Migita, H. Ota, "(Invited) Epitaxial HfO", 2011.

[19] S. S. Cheema, D. Kwon, N. Shanker, R. d. Reis, S.-L. Hsu, J. Xiao, H. Zhang, R. Wagner, A. Datar, M. R. McCarter, C. R. Serrao, A. K. Yadav, G. Karbasian, C.-H. Hsu, A. J. Tan, L.-C. Wang, V. Thakare, X. Zhang, A. Mehta, E. Karapetrova, R. V. Chopdekar, P. Shafer, E. Arenholz, C. Hu, R. Proksch, R. Ramesh, J. Ciston, S. Salahuddin, Nature 2020, 580, 478.

[20] N. Tsuda, K. Nasu, A. Fujimori, K. Siratori, Electronic Conduction in Oxides, Springer Berlin Heidelberg, 2013.

[21] H. Sakai, H. Ohno, N. Oba, M. Kato, K. Yoshimura, Physica B: Condensed Matter 2003, 329-333, 1038.

[22] R. J. Bouchard, J. L. Gillson, Materials Research Bulletin 1971, 6, 669.

[23] K. Sardar, E. Petrucco, C. I. Hiley, J. D. B. Sharman, P. P. Wells, A. E. Russell, R. J. Kashtiban, J. Sloan, R. I. Walton, Angewandte Chemie International Edition 2014, 53, 10960.

[24] R. H. Wakabayashi, H. Paik, M. J. Murphy, D. G. Schlom, M. Brutzam, R. Uecker, R. B. van Dover, F. J. DiSalvo, H. D. Abruna, J. Electrochem. Soc. 2017, 164, H1154.

[25] R. Wang, A. Go, A. J. Millis, Physical Review B 2017, 95, 045133.

[26] A. Jaiswal, E. D. Wachsman, J. Electrochem. Soc. 2005, 152, A787.

[27] V. Esposito, B. H. Luong, E. Di Bartolomeo, E. D. Wachsman, E. Traversa, J. Electrochem. Soc. 2006, 153, A2232.

[28] R. Materlik, C. Künneth, A. Kersch, Journal of Applied Physics 2015, 117, 134109.

[29] M. H. Park, H. J. Kim, Y. J. Kim, W. Lee, T. Moon, C. S. Hwang, Applied Physics Letters 2013, 102, 242905.

[30] J. W. Matthews, A. E. Blakeslee, Journal of Crystal Growth 1974, 27, 118.

[31] K. Persson, Materials Project 2014.

[32] X. Sang, E. D. Grimley, T. Schenk, U. Schroeder, J. M. LeBeau, Applied Physics Letters 2015, 106, 162905.

[33] C. Ophus, Advanced Structural and Chemical Imaging 2017, 3, 13.

[34] A. Pryor, C. Ophus, J. Miao, Advanced Structural and Chemical Imaging 2017, 3, 15.

[35] R. Proksch, S. Kalinin, PFM App Note 2008.

[36] V. Janovec, Cechoslovackij fiziceskij zurnal 1958, 8, 3.

[37] H. F. Kay, J. W. Dunn, The Philosophical Magazine: A Journal of Theoretical Experimental and Applied Physics 1962, 7, 2027.

[38] S. J. Kim, D. Narayan, J.-G. Lee, J. Mohan, J. S. Lee, J. Lee, H. S. Kim, Y.-C. Byun, A. T. Lucero, C. D. Young, Applied Physics Letters 2017, 111, 242901.

[39] A. Gruverman, M. Alexe, D. Meier, Nature Communications 2019, 10, 1661.

[40] S. V. Kalinin, A. N. Morozovska, L. Q. Chen, B. J. Rodriguez, Reports on Progress in Physics 2010, 73, 056502.

[41] A. Gruverman, S. V. Kalinin, Journal of Materials Science 2006, 41, 107.

[42] D. J. Kim, J. Y. Jo, Y. S. Kim, Y. J. Chang, J. S. Lee, J.-G. Yoon, T. K. Song, T. W. Noh, Phys Rev Lett 2005, 95, 237602.

[43] R. R. Mehta, B. D. Silverman, J. T. Jacobs, Journal of Applied Physics 1973, 44, 3379.

[44] S. E. Reyes-Lillo, K. F. Garrity, K. M. Rabe, Physical Review B 2014, 90, 140103.

[45] T. D. Huan, V. Sharma, G. A. Rossetti, R. Ramprasad, Physical Review B 2014, 90, 064111.

[46] Q. Zeng, A. R. Oganov, A. O. Lyakhov, C. Xie, X. Zhang, J. Zhang, Q. Zhu, B. Wei, I. Grigorenko, L. Zhang, L. Cheng, Acta Crystallographica Section C 2014, 70, 76.

[47] W. Zhou, S. V. Ushakov, T. Wang, J. G. Ekerdt, A. A. Demkov, A. Navrotsky, Journal of Applied Physics 2010, 107, 123514.

[48] A. V. Radha, O. Bomati-Miguel, S. V. Ushakov, A. Navrotsky, P. Tartaj, Journal of the American Ceramic Society 2009, 92, 133.

[49] M. W. Pitcher, S. V. Ushakov, A. Navrotsky, B. F. Woodfield, G. Li, J. Boerio-Goates, B. M. Tissue, Journal of the American Ceramic Society 2005, 88, 160.

[50] Bhadeshia, H. K. D. H., & Wayman, C. M. (2014). Phase transformations: nondiffusive. In Physical metallurgy (pp. 1021-1072). Elsevier.

Chapter 4

Textured HZO thin films on LSMO/STO

Since the pyrochlore electrode is not suitable for electrical measurements due to current leakage caused by interface roughness, we focus on another ferroelectric HZO material system for HZO application. $La_{0.67}Sr_{0.33}MnO_3$ is a popular choice for depositing relatively epitaxial HZO films, and the material system exhibits a large polarization [1-3]. Wei *et al.* reported the HZO/LSMO/STO stack for the first time. They managed to determine a new ferroelectric phase (rhombohedral) of HZO. This new phase is a variation of the ferroelectric orthorhombic phase and the key of the phase formation is that the highly textured HZO is deposited in (111) direction on (001) oriented LSMO, the compressive in-plane strain forces the shrink of the in-plane lattice and the elongation along the (111) direction of HZO. This difference in d-spacing between the two phases is presented in Figure 4.1. In our study, we deposited r-phase ultra-thin HZO film on LSMO electrodes and single-crystal STO substrates for the FTJ study (Chapter 5). Furthermore, to push the ferroelectric HZO devices towards application, we also deposited the whole HZO/LSMO/STO stack onto Si substrates and looked into the field cycling behavior. We believe the choice of conducting perovskite electrodes helps reduce the polarization loss during cycling based on the well-established literature in perovskite ferroelectrics such as PZT [4-8]. This part will be introduced in detail in chapter 4.3.

4.1 Deposition on LSMO/STO

Ultra-thin ferroelectric HZO film on single-crystal STO substrates

For the ultra-thin HZO film deposition, LSMO films with a thickness of ≈60 nm were first deposited onto an STO (001) substrate for better conduction, and subsequently, HZO films with varying thicknesses were deposited onto the LSMO seed layer.

The XRD figure of this material is shown in Figure 4.1. The intense diffraction peak near the STO (001) peak corresponds to the (001) reflection of LSMO, which indicates epitaxial growth. Typically, the (111) reflection of the orthorhombic phase of HZO films appears around 30.5°; however, the slightly lower values of 2θ in our case for thin (<10nm) HZO films correspond to the compressive strain stabilized rhombohedral phase. This can be understood by the fact that with decreasing HZO film thickness (below 10 nm), the d-spacing for (111) planes gradually increases (see upper inset), which thereby suggests that the in-plane compressive strain increases with reducing film thickness.[1] The presence of the diffraction fringes around the (001) LSMO and (111) HZO reflections demonstrate high-quality interfaces of the deposited films. An additional peak around 34.5° for an 18 nm thin film indicates the appearance of the monoclinic phase of HZO with increasing film thickness.

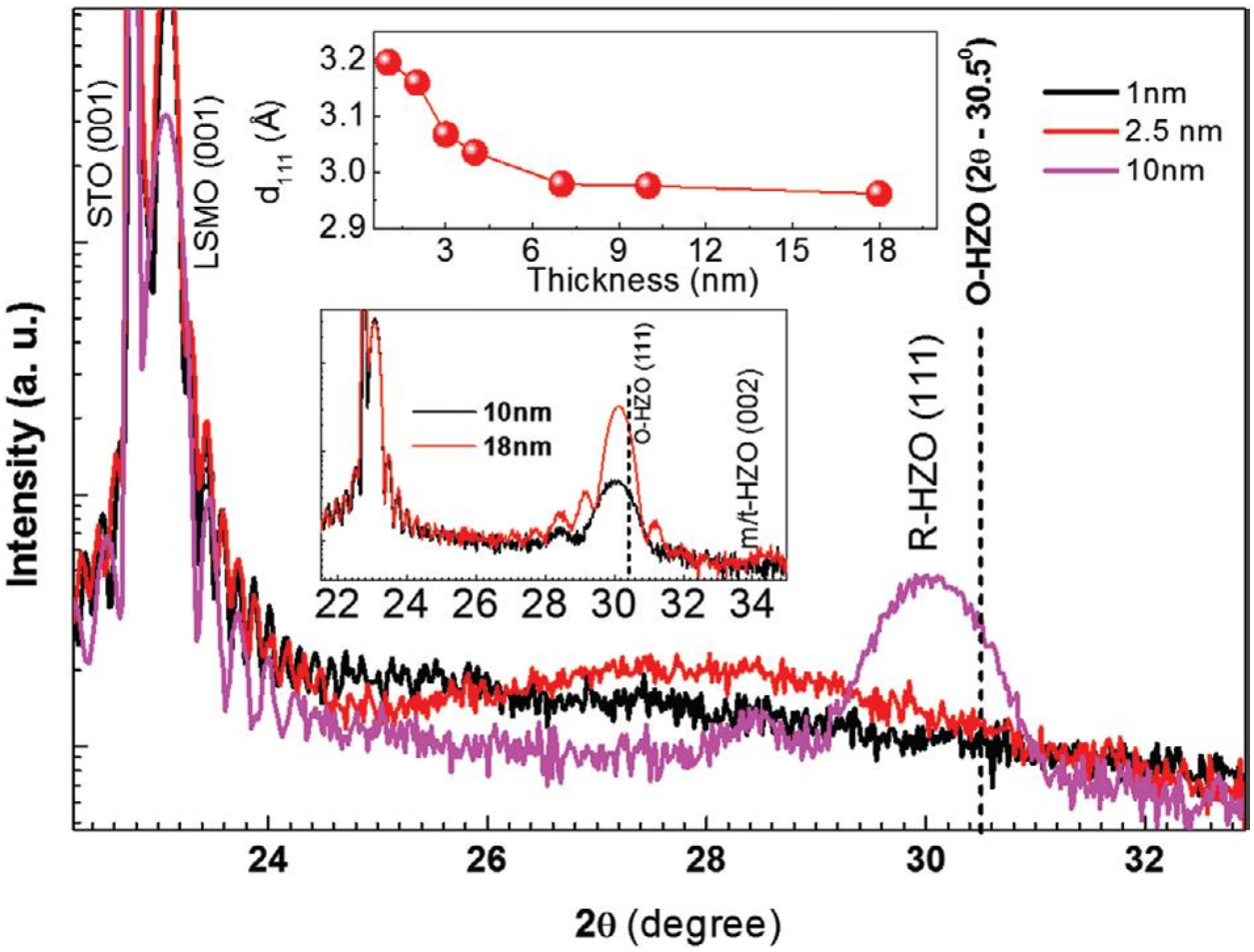

Figure 4.1. X-ray diffraction (θ–2θ) patterns of $Hf_{0.5}Zr_{0.5}O_2$ (1, 2.5, and 10 nm)/$La_{0.7}Sr_{0.3}MnO_3$ (60 nm) bilayer films, grown on a $SrTiO_3$ (001) substrate. The upper inset shows the variation of d-spacing for the 111-reflection of HZO with varying film thicknesses. The lower inset emphasizes the appearance of the nonpolar monoclinic phase of HZO for an 18 nm-thick film.

The deposition of the HZO/LSMO bilayer is further corroborated by TEM imaging (Figure 4.2). As shown in the figure, HZO deposited on LSMO is not as epitaxial as on the pyrochlore electrode, It's a highly textured film with consistent out-of-plane 111 orientation.

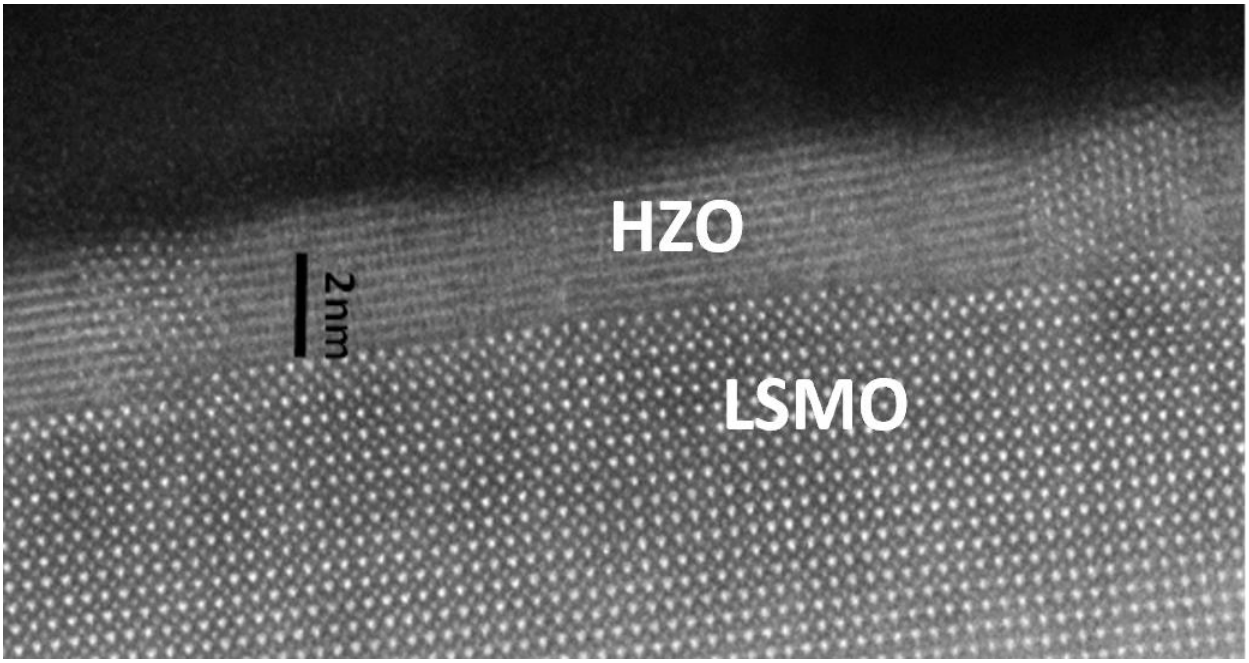

Figure 4.2. High-resolution transmission electron microscopy image of the HZO (~2.5 nm)/LSMO bilayer, epitaxially grown on STO (001) substrate.

Deposition on STO/Si substrates

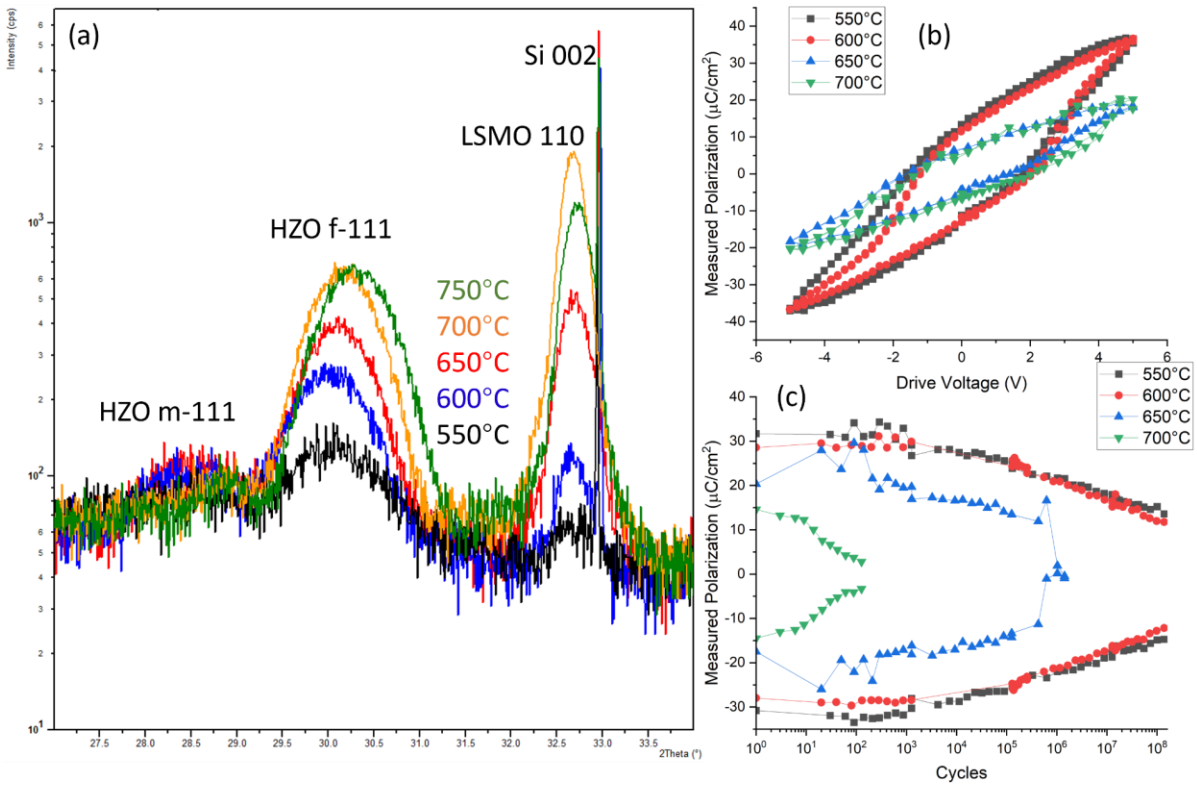

Figure 4.3. Temperature series of HZO PLD on LSMO/STO/Si. (a) XRD spectrum around HZO 111 peak, high-temperature peak shifts towards the right, which means decreasing in 111 d-spacing, indicating strain relaxation due to Si surface damage. (b) Electrical hysteresis loops of samples with different deposition temperatures. High-T ones have smaller polarization (c) Field-cycling tests for samples with different deposition temperatures. Higher temperature results in faster fatigue.

The deposition of the HZO/LSMO stack on STO-coated Si substrates is similar to that on single crystal STO, the only tuned parameter is the deposition temperature. Figure 4.3 shows the temperature series of HZO/LSMO on STO/Si substrates. The optimized temperature for deposition on single crystal substrates is 700°C, while on Si substrates, such high temperature results in the decrease of HZO d-spacing in 111 direction and further undermines the polarization of the HZO layer. The hypothesis is the surface of the Si substrate gets oxidized more easily in higher temperatures. The oxidized substrate can cause strain relaxation and affect the quality of both the LSMO and HZO deposition. Here we find a sweet spot 600°C, to help form the ferroelectric phase of HZO as well as slow down the damage to the substrates.

4.2 Ferroelectric switching behaviors of HZO on LSMO/STO system

The ferroelectric properties of ultrathin HZO films on LSMO/STO were probed by utilizing a piezoresponse force microscopy (PFM) setup. The tip was first biased with ±4V to write a box-in-box pattern and subsequently, the phase-contrast PFM image was obtained at 100 mV tip bias. Figure 4.4a shows the out-of-plane (OOP) phase contrast image of a ≈1 nm HZO film grown on an LSMO//STO substrate. The nearly 180° contrast difference between the outer and inner boxes indicates bistable remanent polarization states. Figure 4.4b shows the corresponding amplitude image of the sample. The signal at the domain walls is almost zero, which suggests the charging effects are low and thus provides further evidence of the ferroelectric character of the film. The uniform phase contrast of the unpoled and inner poled box regions demonstrates that the film is spontaneously polarized without any field cycling. Typically, a few thousand of field cycling is required to "wake up" the ferroelectricity in doped HfO_2 films.[9] Cheema *et al*.[10] have also reported the ferroelectricity in ≈1 nm HZO films grown on a silicon substrate by stabilizing the polar O-phase via strain imposed through the confinement of the film with a metallic capping layer; here, we have stabilized the ferroelectricity in the compressive strain-induced rhombohedral phase of HZO.

Further, the robust ferroelectricity with hysteretic behavior is demonstrated by the local PFM switching on the bare HZO surface with ≈1 nm (Figure 4.4c) and ≈2.5 nm (Figure 4.4d) thick films. The SNR improved with ≈2.5 nm film and hence a clear hysteresis was observed in the phase signal with a corresponding butterfly-shape amplitude (d33) loop. The coercive voltages (|VC|) extracted from piezo loops are ≈1.2 and ≈2.3 V for ≈1 and ≈2.5 nm films, respectively. The ferroelectric switching in ≈1nm HZO film is not as sharp as we see in the case of ≈2.5 nm films. Further, the ferroelectric properties of HZO films were obtained through typical polarization versus voltage and positive-up-negative-down measurements (Figure 4.5). The remanent polarization for ≈2.5 nm HZO films is around 30 μC cm^{-2}, which is within the range of the highest reported remanent polarization values.

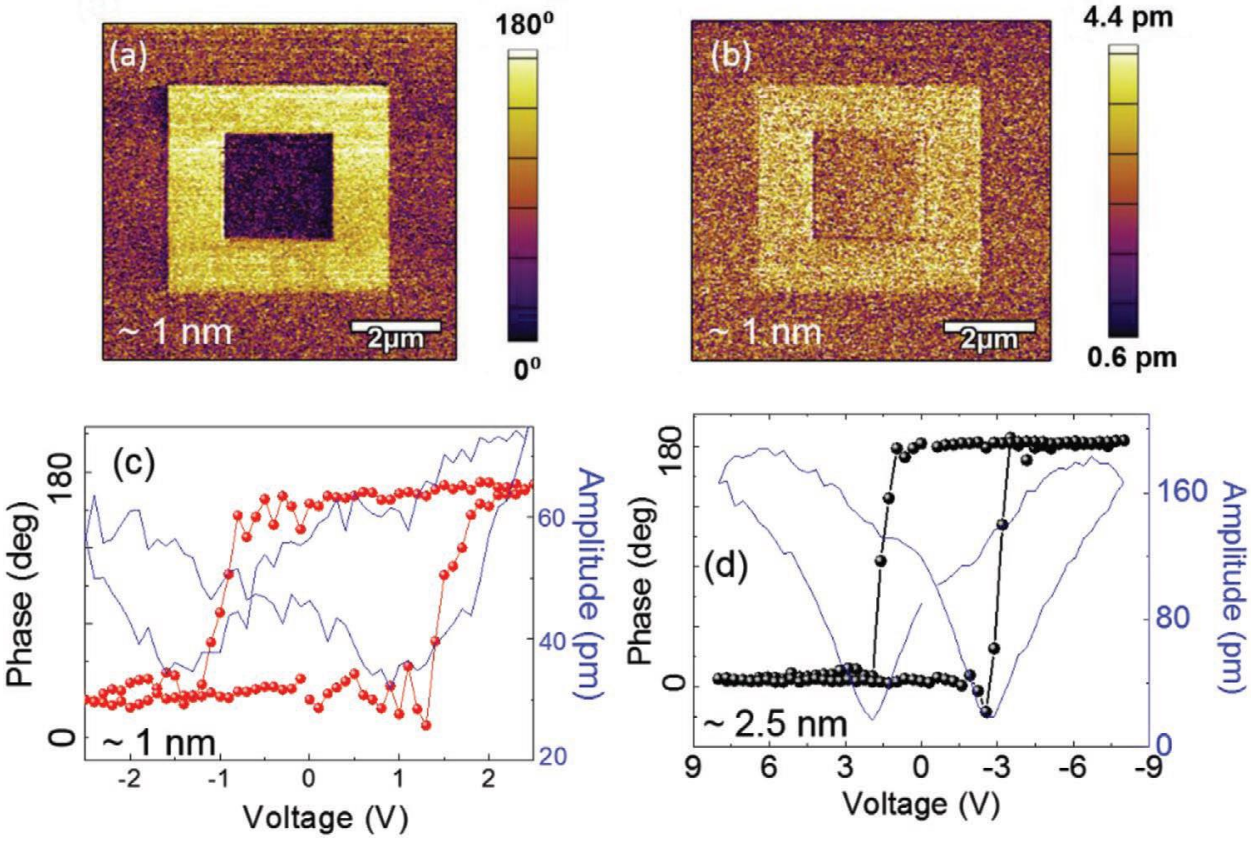

Figure 4.4. PFM (a) phase and (b) amplitude contrast images of ≈1 nm HZO film, and corresponding (c) phase (red) and amplitude (blue) signal of the local hysteresis loop. The approximate time between the writing and reading for the PFM patterns in (a,b) is few minutes. (d) The local PFM phase (black) and corresponding amplitude (blue) hysteresis loops for ≈2.5 nm HZO films.

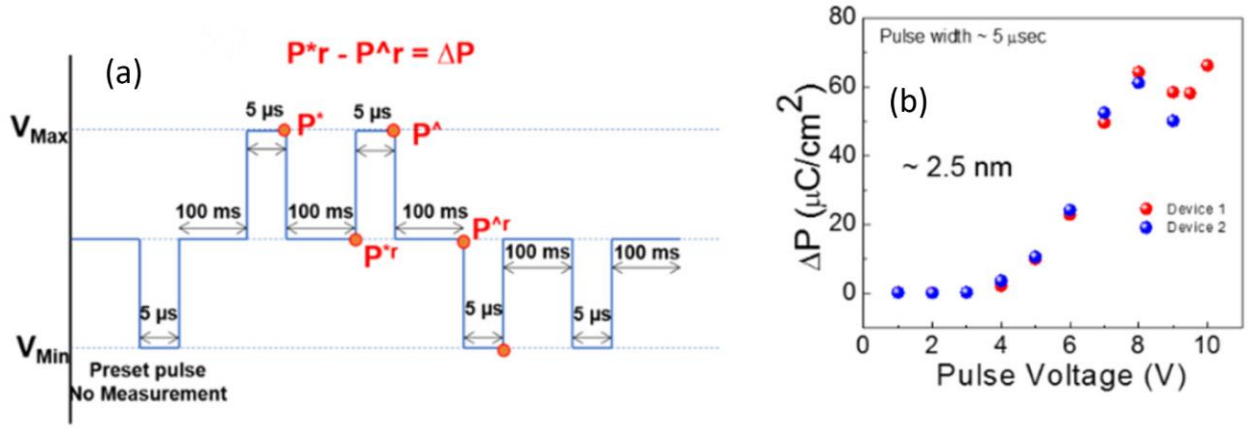

Figure 4.5. (a) Schematics of the voltage pulse for PUND measurement to extract the switched polarization, which is typically 2X the remanent polarization from the P-V loop. (b) PUND characterization of ~ 2.5 nm HZO film for two circular capacitor devices (Ø~ 10μm) showing the remanent polarization of ~ 30 μC/cm^2.

4.3 Field cycling behavior of HZO

Beside the high coercive field, the limited endurance is another potential limitation of HZO to widespread adoption. Previous studies have demonstrated a "wake-up effect" and fatigue behavior in HZO during field cycling, with an emerging consensus built around the crucial role of oxygen vacancies [11-15]. A complete understanding of endurance behavior in HZO and its microscopic origin is therefore vital to understand how they can be improved. The typical HZO films grown on TiN are polycrystalline, leading to leading to issues with switching and endurance. In particular, endurance tests on HZO devices deposited on TiN have shown a significant wake-up effect (increasing switched polarization with cycling) at the initial 10^5 cycles and noticeable fatigue (decreasing switched polarization) at ~ 10^7 cycles, presenting a significant barrier for practical applications. [14, 16]

We set out to probe the role of oxygen-related defects in influencing polarization fatigue by going back to the well-established literature in perovskite ferroelectrics such as PZT, wherein conducting oxide electrodes have been shown to significantly ameliorate the loss of switchable polarization during bipolar cycling [4-8]. With this as the background and with the hypothesis that conducting oxides may also provide a similar benefit in the case of HZO, we initiated a study of the role of conducting perovskite electrodes. Our endurance tests on capacitor structures show an endurance up to 10^{11} cycles, which, although still short of commercial requirements, is a marked improvement compared to films on TiN [14, 16]. To gain more insight into the fundamental origins of bipolar fatigue, we conducted structural measurements on fatigued devices, illustrating the intricacies of polarization switching and fatigue mechanisms in HZO. Our findings, corroborated by first-principles calculations, indicate two key mechanisms for fatigue: a reversible component due to oxygen vacancy redistribution during electronic field cycling, and an irreversible component arising from the competing phase stability of the monoclinic nonpolar phase.

In this chapter, endurance data of HZO on various electrodes, especially a comparison between TiN and oxide electrodes will be introduced; field cycling behavior and analysis will be presented around our LSMO/HZO/LSMO stack.

4.3.1 On TiN and oxide electrodes

Originally utilized as a gate oxide, hafnia's integration into CMOS technology with minimal effort led to the widespread adoption of TiN as the electrode material. Extensive testing on this material system aimed to broaden its applications. While TiN's compatibility with silicon is a significant advantage, several problems associated with this material system have been increasingly linked to the properties of the electrode.

The endurance behavior of the TiN stack presents two primary issues. First is the prolonged "wake-up" period, where the initial polarization value is low, requiring between 10^3 to 10^5 electrical cycles to reach maximum polarization. The second issue is rapid fatigue; industry standards dictate that devices should endure at least 10^{12} cycles, yet HZO/TiN devices often exhibit noticeable polarization degradation around 10^7 cycles.[26] These challenges significantly impede the advancement of hafnia-based ferroelectric devices.

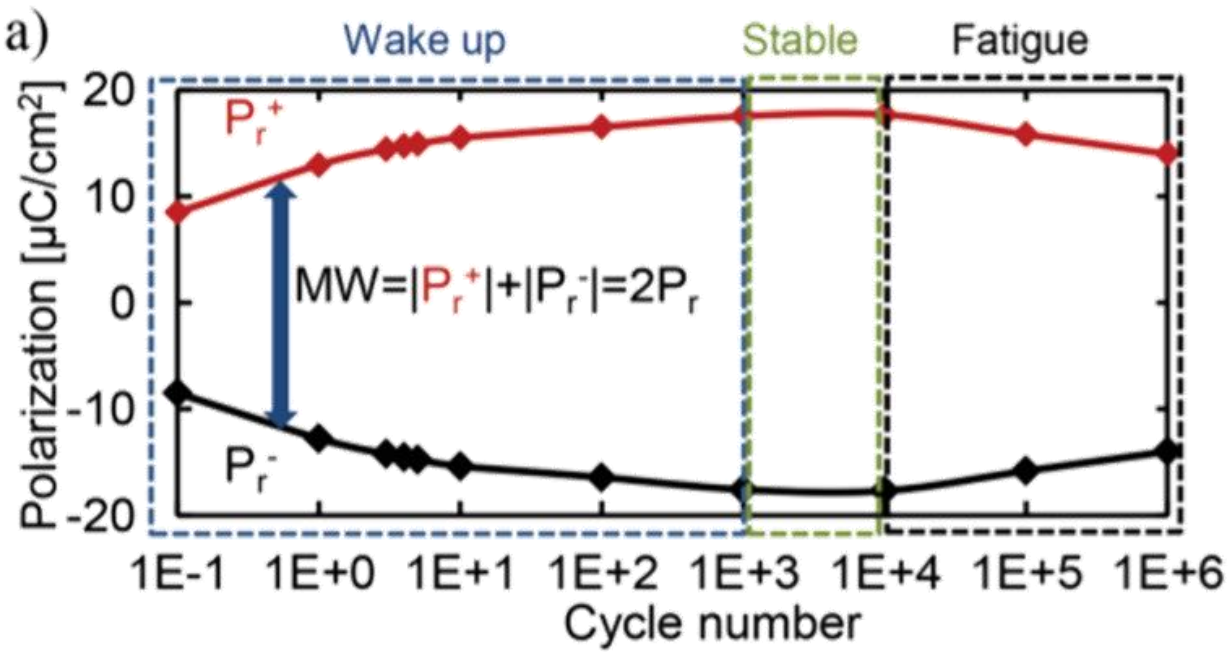

Figure 4.6. A typical hafnia field cycling behavior on TiN electrode. [26]

As research delves deeper into the root causes of these issues, the interface between the TiN and hafnia layers emerges as a likely culprit. Notably, a Ti_xO_y dielectric "dead layer" forms during field cycling, believed to contribute to both wake-up and fatigue effects. Defects in this interlayer, particularly accumulated charged oxygen vacancies, are thought to pin dipoles in the adjacent hafnia layer, leading to decreased polarization. [27]

Switching to metal oxide electrode materials can enhance chemical compatibility, potentially reducing the interfacial layer and thus mitigating the wake-up and fatigue effects. Consequently, there is a growing focus on oxide electrodes in recent studies.

Figure 4.7 below compares the field cycling behavior of TiN and RuO_2 electrodes, with the RuO_2 showing a less wavy pattern. Additionally, a previous study on the HZO/LSMO system successfully eliminated the wake-up effect (Figure 4.8), further supporting the potential benefits of alternative electrode materials.

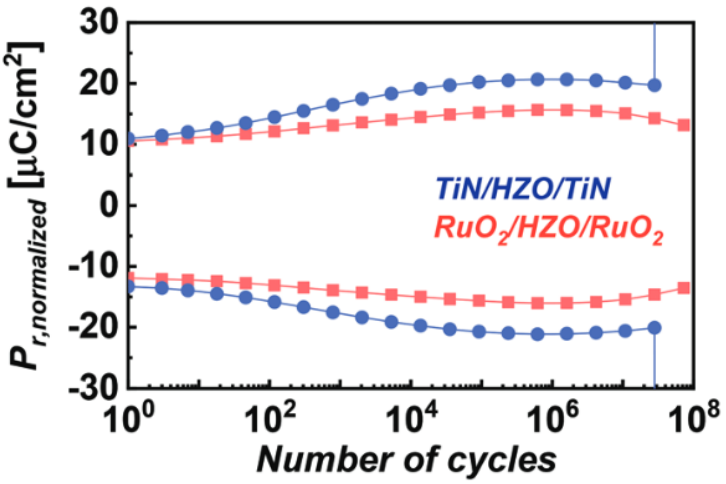

Figure 4.7. Field cycling behavior comparison of ferroelectric HZO using different electrodes. [27]

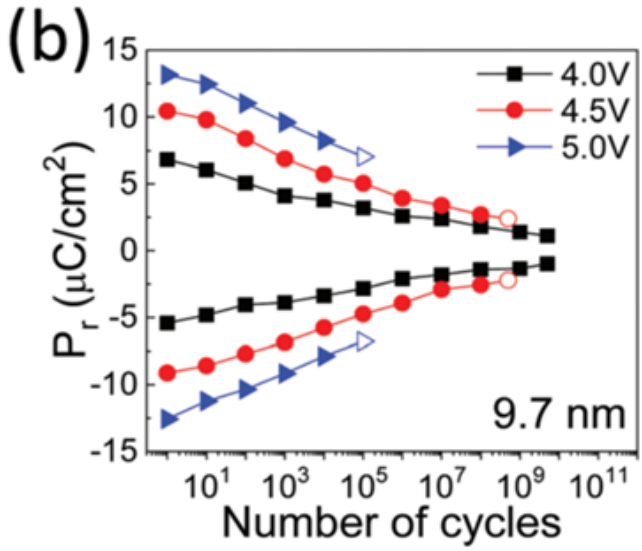

Figure 4.8. Field cycling behavior of ferroelectric HZO on LSMO electrode and single crystal STO substrates. [3]

4.3.2 On our LSMO/STO/Si

The field cycling behavior of our HZO/LSMO (Fig.4.9b) shares similarities with that of lead zirconate titanate (PZT) [17-19]. In particular, both exhibit a wake-up effect at the beginning of cycling, and their fatigued polarization can be recovered by the application of higher voltage pulses, Figure 4.9c. Such a voltage-induced recovery of switched polarization is also implicit in Figure 4.9b where larger voltage pulse amplitudes correlate to a longer endurance, indicating the recovery of polarization due to the higher voltage cycling pulses. On the surface, these similar behaviors of HZO and PZT suggest a possible common cause: such as, domain pinning/depinning caused by defects such as oxygen vacancies. The role of domain pinning in ferroelectric wake-up and fatigue has been explored in prior studies on PZT [17-19]. Given HZO's high oxygen conductivity [20, 21],

charged oxygen vacancies can migrate through the stack during electrical cycling [2] and segregate at grain boundaries and interfaces [15], resulting in pinning of the adjacent ferroelectric domains. Higher voltage pulses aid in the redistribution of oxygen vacancies and domain depinning, thus restoring polarization values. An alternative pathway could be one in which the insertion/removal of oxygen vacancies into the HZO lattice leads to changes in the thermodynamic stability of the polar phase. In order to study this further, we carried out a combination of *ab initio* theoretical calculations of the stability if the polar orthorhombic phase in conjunction with structural studies.

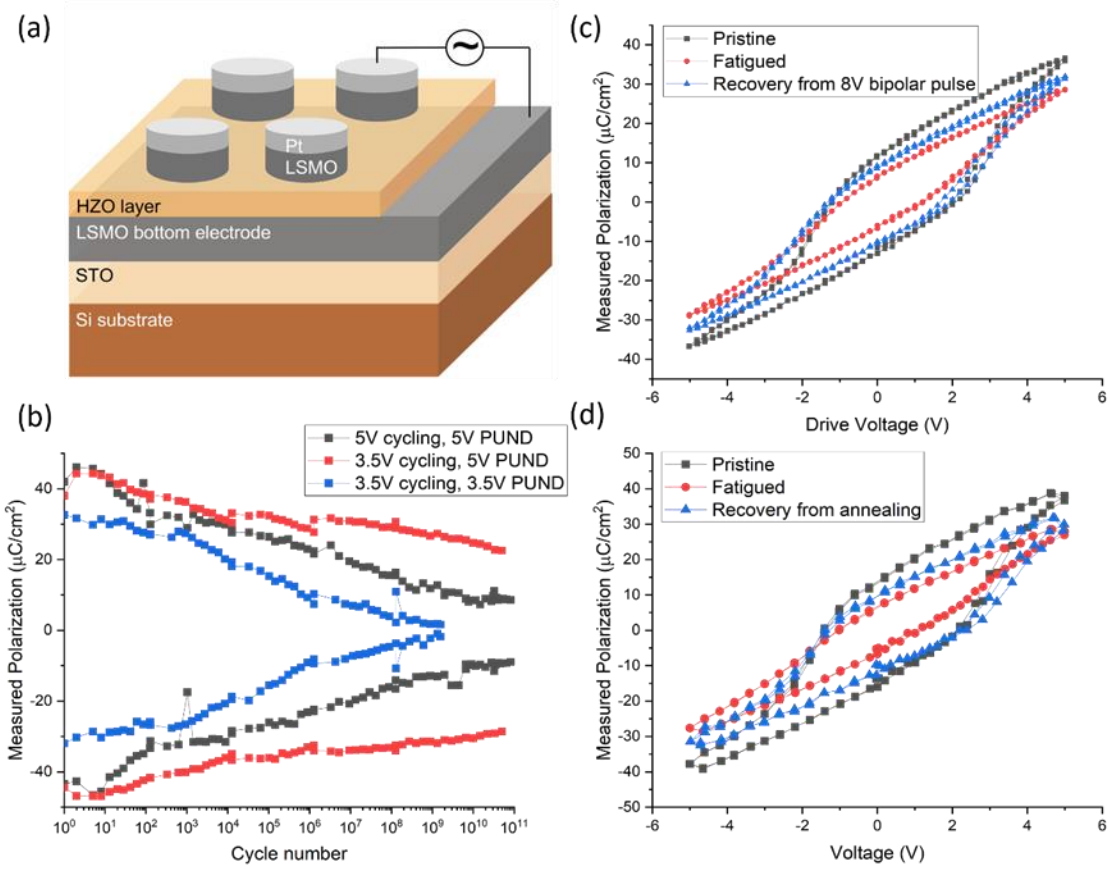

Figure 4.9. (a) Schematic of the HZO capacitor structure and the endurance test; (b) Fatigue of HZO capacitors when cycling & testing under different peak voltages; (c) The fatigued capacitor partially recovered after applying one electric pulse with higher voltage; (d) The fatigued capacitor partially recovered after annealing 1h at 400°C in Air.

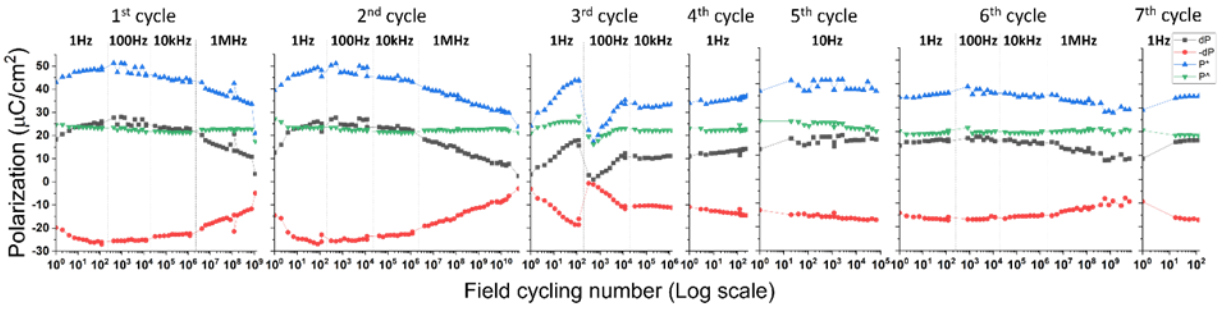

Figure 4.10. The fatigued HZO capacitor can "wake up" again when cycling at low frequency, indicating there is domain depinning due to oxygen vacancy motion. After a few wakeups and fatigues, the polarization maintains a stable value lower than the initial polarization, suggesting a fatigue mechanism beyond domain pinning.

It is noteworthy, however, that the HZO fatigue cannot be entirely attributed to domain pinning. We find that part of the polarization cannot be recovered either by electric pulses or annealing (Fig. 4.9c, d). Further evidence of this is shown with the permanent change of the HZO layer during fatigue in Figure 4.10. We subjected the system to repeated bi-polar electric field cycling, progressively increasing the frequency from 1 Hz to 1 MHz. We recorded the remnant polarization values as a function of the accumulated cycles. To investigate the fatigue recovery behavior, we initiated multiple cycles starting from the lowest frequency once the capacitor exhibited degradation of remnant polarization. Figure 4.10 illustrates the capacitor under study, which underwent seven cycles of this process, effectively demonstrating a cyclic pattern of fatigue, recovery, and subsequent fatigue. While oxygen vacancies are more responsive to low-frequency electric pulses, (allowing for polarization recovery when cycled under low frequency), the polarization eventually attains a stable value that is much lower than the initial polarization after several wake-up-fatigue cycles. This indicates a mechanism beyond domain pinning contributing to fatigue, namely an irreversible effect occurring within the HZO layer that degrades its intrinsic ferroelectricity. We, therefore proceeded to carry out theoretical calculations and structural measurements to probe the origins of this behavior.

4.3.3 Phase transformation induced by field cycling

First, we performed Density Functional Theory (DFT) calculations to explore the role of oxygen vacancies on the phase stability of the polar and nonpolar phases of HZO. We considered the antiferroelectric (o-AFE) and ferroelectric (o-FE) polymorphs with space groups Pbca and $Pca2_1$ respectively, the nonpolar monoclinic phase (m) with space group $P2_1/c$, and the presumed nonpolar parent/intermediate tetragonal (t) phase with space group P4/nmm. For this, HZO had a 50:50 Hf:Zr stoichiometry adopting a checkerboard alloy composition of the cation sublattice (that is, Hf and Zr alternating in all directions) and a unit cell comprised of 32 formula units (98 atoms) to allow for a range of low-concentration oxygen vacancies to be explored. We found that different alloy orderings have energy differences (~meV/f.u.) less than those between the different polymorphs (~10 meV/f.u.), so consider only this checkerboard ordering for this work. Consistent with prior work we find that the m-phase is the ground state structure, while other polymorphs are

accessible with strain (Fig. 4.11a). A small compressive strain favors the o-AFE phase, and the t-phase is favored at higher strain values. Interestingly, and as has been previously noted, the o-FE is never the global ground state even with applied strain.

We argue that this irreversible effect leading to the fatigue behavior of HZO arises from the phase transformation from the polar o-phase to the nonpolar m-phase. According to the density functional theory (DFT) calculations described later, while the o- to t- and o- to m-phase pathways are initially energetically competitive, the m-phase is globally far more stable and cannot be recovered once adopted. We now present experimental evidence for the increased presence of the m-phase during switching cycles, and following that, connect it to our theoretical analysis.

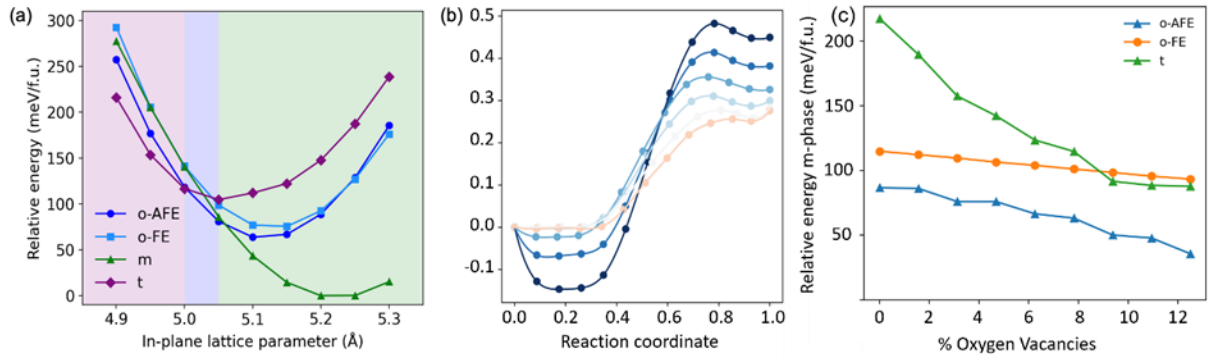

Figure 4.11. (a) Relative energies of the m-, t-, o-AFE, and o-FE phases of $Hf_{0.5}Zr_{0.5}O_2$ calculated from DFT with in-plane epitaxial strain. (b) Nudged-elastic band calculations of the o-HZO to t-HZO transition for epitaxial strain values of -1%, 0%, and +1%. (c) Relative energies of the t, o-AFE, and o-FE phases with oxygen vacancy concentration relative to that of the m phase.

The structural phase transition during the fatigue process was investigated by scanning X-ray nano-diffraction in section 26-ID-C of Advanced Photon Source, Argonne National Laboratory. Unlike other local or bulk characterization methods, the nanoscale X-ray beam, with a resolution down to ~30nm, can easily locate and map out the reciprocal space information of each device. Capacitors of three states are scanned for structural information: pristine, after wake-up, and after a fully fatigued state. The diffraction peak intensity of the nonpolar monoclinic phase and the polar orthorhombic phase are integrated to estimate the phase ratio on the capacitors. This semi-quantitative result is shown in Figure 4.12b: As more electric cycles are applied, from the pristine to the wake-up state, until the fatigue state, the m-/o-phase ratio keeps increasing, demonstrating the phase transition from o- to m-phase is a fundamental cause of the degradation of HZO ferroelectricity. We also find that the o-phase fraction is reduced in the wake-up state compared to the pristine state- evidence that domain depinning is the leading cause of the wake-up effect.

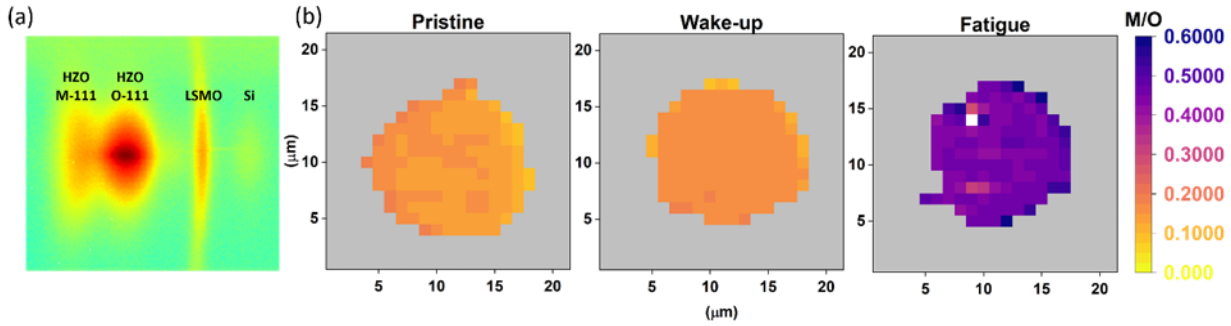

Figure 4.12. X-ray nano-diffraction of single capacitors at different fatigue states. (a) the diffraction pattern of a 1μm*1μm area. (b) Scanning of capacitors at three different states: pristine, wake-up, and fatigue. The figure shows the diffraction intensity ratio of the non-ferroelectric, monoclinic phase to the ferroelectric, orthorhombic phase. The ratio keeps increasing from the pristine to the fatigued state, indicating a phase transition from the o- to the m-phase during cycling.

To gain a more comprehensive understanding of the m/o (monoclinic/orthorhombic) ratio variation across the entire capacitors, we conducted an integration of the nano diffraction signals across real space. The data integrated and presented in Figure 4.13a,b offers a semi-quantitative analysis of the phase composition within these capacitors. In these figures, all intensity values are normalized to a single pixel, with the left and right diffraction peaks corresponding to the non-polar m-phase and the polar o-phase, respectively.

Figure 4.13a compares the intensity of different states of four capacitors: one in its pristine state, one in the wake-up state, and two in the fatigue state. The analysis reveals a discernible decrease in the o-phase peak and an increase in the m-phase peak in the fatigued capacitors, strongly supporting the hypothesis of a HZO phase change induced by field cycling.

In Figure 4.13b, the focus shifts to fatigued capacitors that underwent cycling at varying temperatures. The observed trend is unmistakable: with increasing cycling temperature, there is a noticeable rise in the m-phase formation, accompanied by a reduction in the o-phase. This observation aligns with our hypothesis that thermal activation promotes the phase transition towards the more stable phase.

Figure 4.13c further corroborates the occurrence of phase transition during field cycling through a more detailed real-space mapping of nano diffraction intensity, centered around the m and o peaks. The color coding in this figure—reddish hues indicating high intensity and bluish tones signifying low intensity—provides a clear visualization of the phase distribution. Specifically, the fatigued capacitor, highlighted by the large central circle, which underwent $5e^{10}$ electric field cycles, exhibits a pronounced diffraction intensity in the m-phase. Conversely, the two smaller areas adjacent to the capacitor (located in the upper right and lower left) remain in their pristine state, as they were not subjected to cycling. These regions display a higher intensity in the o-phase, indicating their retention of the initial phase composition.

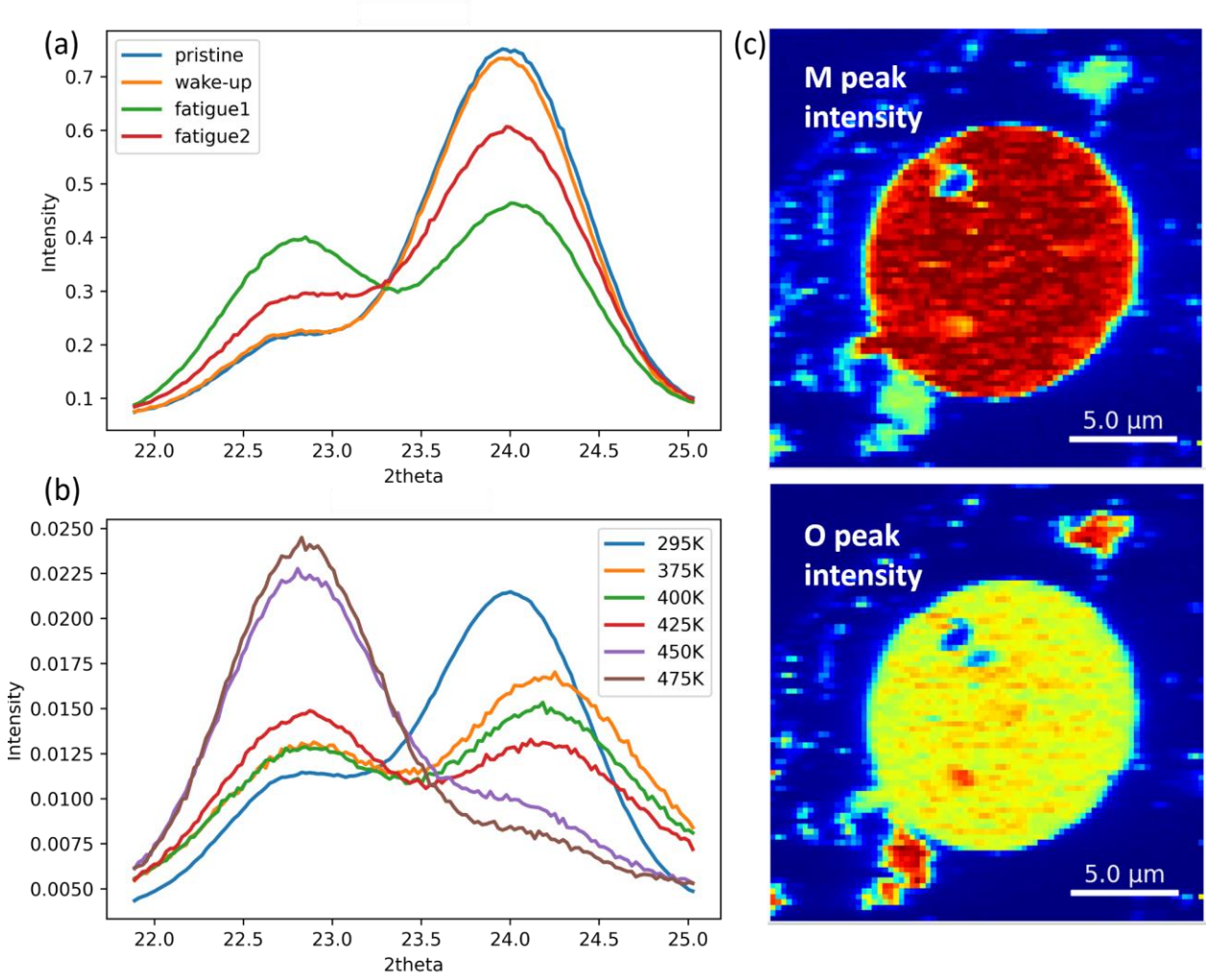

Figure 4.13. (a) Space-integration of 10keV X-ray nano diffraction data across whole HZO capacitors in pristine, wake-up, and fatigue states. The left and right peaks are from m-phase and o-phase respectively. (b) Integrated nano diffraction data of fatigue capacitors cycling under different temperatures. (c) Real-space nano diffraction mapping of the same fatigue capacitor at 2 different 2-theta angles, corresponding to the intensity of m-phase and o-phase respectively.

To investigate another possible phase switching of t- to m-phase, we consider the kinetic energy barriers for the phase transition in going from t- to m- and t- to o-phase. Prior reports of these barriers range from 208 to 315 meV per formula unit (f.u.) for the t- to m-phase transition, and 22 to 31 meV/f.u. for the t- to o-phase transition. From these observations, we can infer that the phase transition from t- to m-phase is kinetically suppressed, despite the m-phase being the global ground-state polymorph. However, while the t-phase to o-phase transition is more favorable than the t-phase to m-phase from these kinematic considerations, an interesting result emerges when we consider repeated switching cycles. Instead, for the reverse transition, the large barrier that disfavors the t- to m-phase transition, now acts as a stabilizing force for the m-phase. The result of this is that repeated cycling will gradually increase the volume fraction of the m-phase, consistent

with our experimental results. Finally, we explore the role of strain on the t- to o-phase barrier by performing nudged elastic band calculations for several values of compressive and tensile strain (Fig. 4.11b). Consistent with prior reports [22, 23], we find that strain can indeed modify the barrier heights for this phase transition. However, it does not increase it to a level such that it would be competitive with the t-phase to m-phase transition. In fact, we find that for small amounts of tensile strain, the t- to o-phase barrier is reduced, favoring a greater volume fraction of the polar phase, as has been observed in the literature.

The oxygen vacancy plays an essential role in the HZO phase transition, and as we hypothesize, in its fatigue behavior. Prior work [2] observed the structural change of the LSMO electrode between perovskite and brownmillerite with an applied electric bias to the LSMO/HZO/LSMO stack. Their findings demonstrated that a significant volume of oxygen vacancies migrate through the interface under an electric field, with the LSMO electrode concurrently functioning as both a source and sink for oxygen vacancies. Thus, there is a constant process of oxygen vacancy redistribution during field cycling. As demonstrated in prior theoretical work [24, 25], and corroborated by our own DFT calculations, oxygen vacancies reduce the barrier to obtaining the polar o-AFE and o-FE phases relative to the m-phase (Fig. 3c). Therefore, one key conclusion is that having a readily available source/sink of oxygen vacancies is crucial for obtaining and maintaining the o-phase regions. Thus, during cycling, if the HZO becomes further oxygenated (i.e., depleted of oxygen vacancies) as they migrate and are pinned at domain walls, it will result in a reduction in the volume fraction of the o-phase and consequently a reduction in the polarization.

To further explore the influence of oxygen vacancy concentration on fatigue behavior, we reduced the concentration of mobile oxygen vacancies by doping HZO with 0.7% La (corresponding to approximately 10^{20} cm^{-3} concentration). Our hypothesis of doping with La is that since the oxygen vacancies tend to bind to the La^{3+}, there will be less migration/redistribution of the oxygen vacancies in La:HZO than in pure HZO. Because of this, domain wall pinning by oxygen vacancies will be suppressed in La:HZO. After the same etching and testing process, we compare the fatigue rate of pure HZO and La:HZO in Figure 4.10. The endurance lifetime of these La:HZO capacitors (Figure 4.14) is measurably higher compared to HZO devices (Figure 4.10), consistent with our expectations. This result supports the notion that maintaining a stable oxygen vacancy concentration level is crucial in preserving ferroelectricity in HZO.

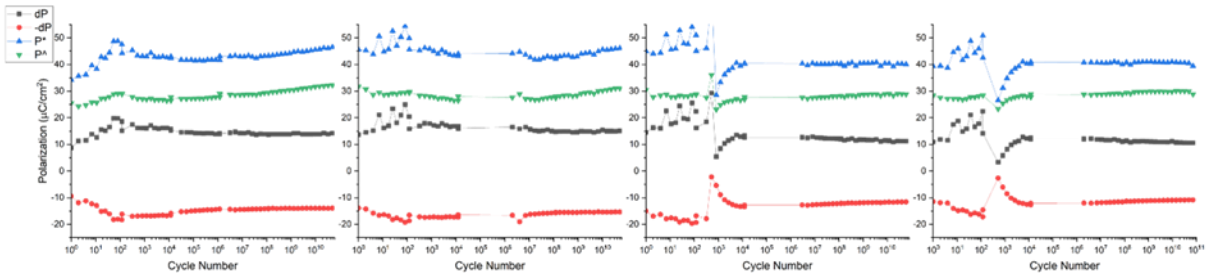

Figure 4.14. Same endurance measurements on La: HZO capacitors. The polarization is more stable compared to pure HZO capacitors in Figure 2, indicating that La dopant does help keep oxygen vacancies inside the HZO layer and slow down the fatigue process.

In summary, we present direct structural evidence, supported by *ab initio* calculations that point to the role of oxygen intercalation into the o-phase of HZO to destabilize it into the nonpolar m-phase. This mechanism is pointedly different from that in the perovskite ferroelectrics such as PZT. Thus, we surmise that a precise defect chemistry engineering leads to the trapping of the oxygen vacancies (and thus the stability of the o-phase) in the HZO structure.

References

[1] Y. Wei, P. Nukala, M. Salverda, S. Matzen, H. J. Zhao, J. Momand, A. S. Everhardt, G. Agnus, G. R. Blake, P. Lecoeur, B. J. Kooi, J. Iniguez, B. Dkhil, B. Noheda, Nat Mater 2018, 17, 1095.

[2] P. Nukala, M. Ahmadi, Y. Wei, S. de Graaf, E. Stylianidis, T. Chakrabortty, S. Matzen, H. W. Zandbergen, A. Björling, D. Mannix, D. Carbone, B. Kooi, B. Noheda, Science 2021, 372, 630.

[3] J. Lyu, T. Song, I. Fina, F. Sánchez, Nanoscale 2020, 12, 11280.

[4] F. Chen, Q. Z. Liu, H. F. Wang, F. H. Zhang, W. Wu, Applied Physics Letters 2007, 90, 192907.

[5] C. W. Law, K. Y. Tong, J. H. Li, K. Li, M. C. Poon, Thin Solid Films 1999, 354, 162.

[6] J. Lee, R. Ramesh, V. G. Keramidas, W. L. Warren, G. E. Pike, J. T. Evans, Jr., Applied Physics Letters 1995, 66, 1337.

[7] R. Ramesh, H. Gilchrist, T. Sands, V. G. Keramidas, R. Haakenaasen, D. K. Fork, Applied Physics Letters 1993, 63, 3592.

[8] J. Lee, L. Johnson, A. Safari, R. Ramesh, T. Sands, H. Gilchrist, V. G. Keramidas, Applied Physics Letters 1993, 63, 27.

[9] M. H. Park, Y. H. Lee, T. Mikolajick, U. Schroeder, C. S. Hwang, MRS Commun. 2018, 8, 795.

[10] S. S. Cheema, D. Kwon, N. Shanker, R. dos Reis, S.-L. Hsu, J. Xiao, H. Zhang, R. Wagner, A. Datar, M. R. McCarter, C. R. Serrao, A. K. Yadav, G. Karbasian, C.-H. Hsu, A. J. Tan, L.-C. Wang, V. Thakare, X. Zhang, A. Mehta, E. Karapetrova, R. V. Chopdekar, P. Shafer, E. Arenholz, C. Hu, R. Proksch, R. Ramesh, J. Ciston, S. Salahuddin, Nature 2020, 580, 478.

[11] Y. Goh, S. H. Cho, S.-H. K. Park, S. Jeon, Nanoscale 2020, 12, 9024.

[12] W. Hamouda, F. Mehmood, T. Mikolajick, U. Schroeder, T. O. Mentes, A. Locatelli, N. Barrett, Applied Physics Letters 2022, 120.

[13] M. G. Kozodaev, A. G. Chernikova, E. V. Korostylev, M. H. Park, R. R. Khakimov, C. S. Hwang, A. M. Markeev, Journal of Applied Physics 2019, 125.

[14] M. Pešić, F. P. G. Fengler, L. Larcher, A. Padovani, T. Schenk, E. D. Grimley, X. Sang, J. M. LeBeau, S. Slesazeck, U. Schroeder, T. Mikolajick, Advanced Functional Materials 2016, 26, 4601.

[15] W. Wei, W. Zhang, F. Wang, X. Ma, Q. Wang, P. Sang, X. Zhan, Y. Li, L. Tai, Q. Luo, H. Lv, J. Chen, "Deep Insights into the Failure Mechanisms in Field-cycled Ferroelectric $Hf_{0.5}Zr_{0.5}O_2$ Thin Film: TDDB Characterizations and First-Principles Calculations", presented at 2020 IEEE International Electron Devices Meeting (IEDM), 12-18 Dec. 2020, 2020.

[16] F. Fengler, M. H. Park, T. Schenk, M. Pešić, U. Schroeder, in Ferroelectr Doped Hafnium Oxide Mater Prop Devices, (Eds: U. Schroeder, C. S. Hwang, H. Funakubo), Woodhead Publishing, 2019, 381.

[17] X. J. Lou, Journal of Applied Physics 2009, 105.

[18] J. F. Scott, M. Dawber, Applied Physics Letters 2000, 76, 3801.

[19] I. K. Yoo, S. B. Desu, physica status solidi (a) 1992, 133, 565.

[20] P. Kofstad, D. J. Ruzicka, J. Electrochem. Soc. 1963, 110, 181.

[21] M. F. Trubelja, V. S. Stubican, Solid State Ionics 1991, 49, 89.

[22] B. Johnson, J. L. Jones, Ferroelectr Doped Hafnium Oxide Mater Prop Devices 2019, 25.

[23] Z. Zhang, S.-L. Hsu, V. A. Stoica, H. Paik, E. Parsonnet, A. Qualls, J. Wang, L. Xie, M. Kumari, S. Das, Z. Leng, M. McBriarty, R. Proksch, A. Gruverman, D. G. Schlom, L.-Q. Chen, S. Salahuddin, L. W. Martin, R. Ramesh, Advanced Materials 2021, 33, 2006089.

[24] M. Hoffmann, U. Schroeder, T. Schenk, T. Shimizu, H. Funakubo, O. Sakata, D. Pohl, M. Drescher, C. Adelmann, R. Materlik, A. Kersch, T. Mikolajick, Journal of Applied Physics 2015, 118.

[25] H.-J. Lee, M. Lee, K. Lee, J. Jo, H. Yang, Y. Kim, S. C. Chae, U. Waghmare, J. H. Lee, Science 2020, 369, 1343.

[26] Chouprik, A., Negrov, D., Tsymbal, E. Y., & Zenkevich, A. (2021). Defects in ferroelectric HfO 2. Nanoscale, 13(27), 11635-11678.

[27] Goh, Y., Cho, S. H., Park, S. H. K., & Jeon, S. (2020). Oxygen vacancy control as a strategy to achieve highly reliable hafnia ferroelectrics using oxide electrode. Nanoscale, 12(16), 9024-9031.

Chapter 5:

Towards future applications of ferroelectric HZO

5.1 Prototype of ferroelectric tunnel junction (FTJ) based on ferroelectric HZO

FTJ is currently vigorously explored as a candidate for next-generation computation since it gives a solution to robust nonvolatile memory as well as its low operation energy and high operation speed. In an FTJ, an ultrathin film of a ferroelectric material, sandwiched between two metallic electrodes having different electronic screening lengths, is used as a tunnel barrier that provides a route to modulate the resistance states of a tunnel device upon the application of an electric field. This so-called tunnel electroresistance (TER) effect, is created by manipulating the polarization states of the barrier layer. [1,2] In these devices, the bound charges in the form of electric dipole moments in the ferroelectric barrier layer do not fully compensate the electrode charges at the barrier/electrode interface due to the limited screening length of electrons in metals. Hence, if the two electrodes have different screening lengths, the potential profile across the barrier layer modulates asymmetrically with the polarization reversal which thereby will significantly alter the tunneling current. [2,3] More introduction to FTJ can be found in chapter 1.

Recently, doped HfO_2-based FTJs have been investigated with ≈2–4 nm thick barrier, [4-8] but the tunneling current density of these devices is too small, particularly due to the highly insulating nature of HfO_2 (bandgap ≈ 5–6 eV); hence the low signal-to-noise ratio (SNR) during the read operation is still a major issue. Therefore, reducing the thickness of the barrier layer down to 2–3 unit cells is required to enhance the tunneling current density as it depends exponentially on the thickness of the barrier layer. Moreover, obtaining single-phase ferroelectric films with ALD-grown polycrystalline samples has been challenging.[9] The presence of grain boundaries and defects in these films diminish the ferroelectricity. Therefore, single-crystalline epitaxial films are desirable for achieving ferroelectricity in ultrathin films.

In this chapter, we demonstrate FTJs with a very large OFF/ON resistance ratio and relatively low resistance area product (RA) with ≈1 nm thick Zr doped HfO_2 (HZO) ferroelectric tunnel barrier. We stabilized ferroelectricity in ultrathin films of rhombohedral HZO (R-HZO) through the substrate-induced compressive strain by growing the epitaxial films on single crystalline $SrTiO_3$ (STO) (001) substrates. The resistance area product at the bias voltage (≈300 mV) required for one-half of the zero-bias TER ratio is three orders of magnitude lower than the reported value with relatively thick ferroelectric barriers.[8] The OFF/ON resistance ratio of 135 achieved with ≈1 nm barrier, which is enhanced to 10^5 with increasing the barrier thickness to 2.5 nm, is amongst the highest reported values for HZO-based FTJs.

5.1.1 Performance of 1nm HZO FTJ devices

The extent of the modulation of the ferroelectric tunnel barrier in FTJ devices depends upon the difference in the screening lengths of electrons in the two opposing electrodes. Typically, conducting oxides show one order of magnitude higher electronic screening length than metals. Hence, a conducting oxide/ferroelectric barrier/ metal structure is commonly used for FTJ devices. In this work, we have used $La_{0.7}Sr_{0.3}MnO_3$ (LSMO) as a bottom oxide electrode for our FTJ devices. LSMO films with a thickness of ≈60 nm were first deposited onto an STO (001) substrate, and subsequently, HZO films with varying thicknesses were deposited onto the LSMO seed layer. The structural and ferroelectric properties of this material system are introduced in Chapter 4.

The schematic of our FTJ device is shown in Figure 5.1(a), Figure 5.1(b) shows the I–Vread curves of an FJT device, comprising an HZO tunnel barrier ≈1 nm, after applying the voltage pulse of ± 2.5 V with a width of ≈1 ms, which is much larger than the coercive voltage of ≈1 nm HZO film (measured by PFM in chapter 4). We see a large change in the tunneling current of the device when the ferroelectric polarization direction is switched, and hence, we can define the low and high tunneling current at a given voltage as the OFF and ON states, respectively.

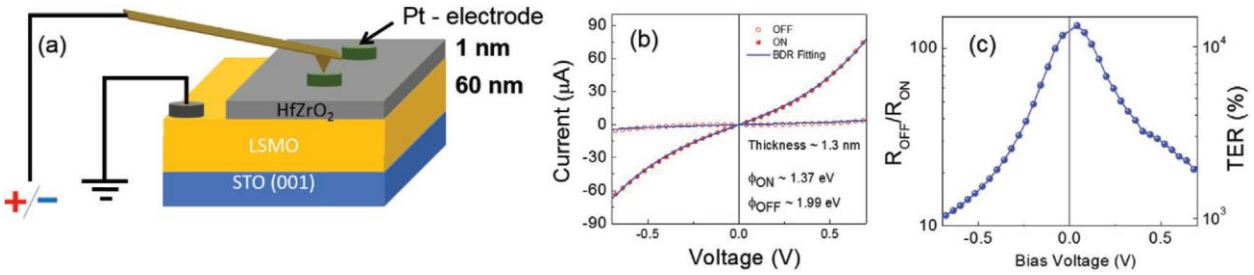

Figure 5.1. (a) Schematic setup for the tunneling transport measurements of the ultrathin HZO tunnel devices. (b) Current–voltage characteristic of a circular device (Ø ≈ 5 μm) with a ≈ 1 nm HZO FE tunnel barrier. Solid blue lines are the fitted results using pure direct tunneling-based BDR model. (c) Corresponding OFF/ON ratio (TER%) of the junction resistance with ≈1 nm barrier.

To confirm that the observed switching behavior in these devices is due to tunneling rather than another resistive switching mechanism, we fit the I–V data with a tunneling model (Brinkman–Dynes–Rowell model), based on Fermi–Dirac statistics and the Wentzel–Kramers–Brillouin approximation, across a rectangular shaped potential profile.

According to the BDR model, the tunneling current density through an insulating barrier can be expressed as:

$$J(V) = G_0 \left[V - \left(\frac{A_0 \Delta\phi}{16 \bar{\phi}^{3/2}} \right) (eV)^2 + \left(\frac{9 A_0^2}{128 \bar{\phi}} \right) (eV)^3 \right]$$

where $G_0 = 3.16 \times 10^{10} \left(\frac{\bar{\phi}^{1/2}}{t} \right) \exp\left(-1.025 t \bar{\phi}^{1/2} \right)$ and $A_0 = 4(2m)^{1/2} \frac{t}{3\hbar}$.

Here, A is the device area. We assume that the effective mass (m) of the electron is equal to the electron mass (m_0). The average barrier height ($\bar{\emptyset}$) and film thickness (t) were the free fitting parameters. The difference in the work functions of the electrodes with respect to the HZO conduction layer is accounted into the above equation by $\Delta\emptyset=\emptyset 2-\emptyset 1$.

The average barrier heights for OFF and ON states are ≈1.99 and ≈1.37 eV, respectively. The barrier thickness is 1.3nm for both OFF and ON states, with good agreement with the expected value. This consistent fitting parameter indicates a negligible piezoelectric effect in the HZO layer. Another supporting evidence is, the piezoelectric coefficient of HZO is less than 10 pm V^{-1},[10] the maximum change in the thickness of the film due to the applied electric field will be a few tens of pm, and the corresponding electroresistance will be less than 1%.

The OFF/ON junction resistance ratio of 135 was achieved at zero bias from a device with 1 nm thick barrier (see Figure 5.1c), and it gradually decreases with increasing bias voltage. The bias voltage for one-half of the zero-bias TER for these devices was observed at 200–300 mV, which is typically considered to be an appropriate read voltage for ferroelectric tunnel devices.[11] The ON and OFF states' resistance-area product (RA) for ≈1 nm barrier devices at 300 mV are ≈25 and ≈600 kΩ μm2, respectively which is nearly three orders of magnitude smaller than reported values for other HZO-based FTJs for relatively thicker barriers.[7]

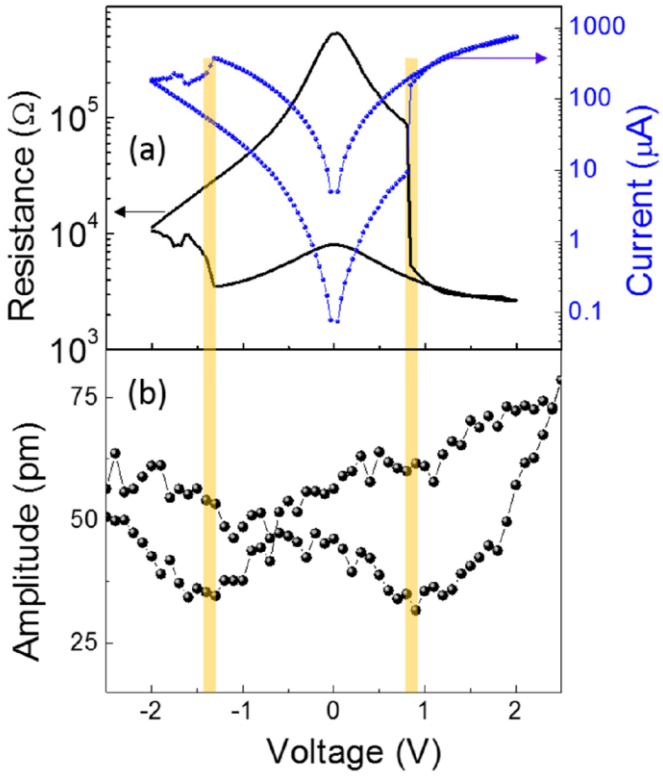

Figure 5.2. (a) Junction resistance versus write voltage pulse (black) with a width of ~ 1 ms and corresponding current-voltage (blue) characteristics of an FTJ (Ø~ 5μm) with ~ 1 nm HZO barrier layer. (b) The PFM amplitude hysteresis loop of ~ 1nm HZO film, measured with 1 ms voltage pulses, emphasizes

that the resistance switching in our FTJs is predominantly due to the ferroelectric polarization switching of the barrier layer.

Another supporting evidence of ferroelectric polarization as the predominant cause of resistance switching is the good agreement between the switching voltages of the devices, extracted from the junction resistance versus voltage plot, with the coercive voltages extracted from the PFM switching plot. This comparison is shown in Figure 5.2.

5.1.2 Scaling of HZO FTJ devices

When increasing the HZO thickness to ~2.5nm, a similar bias dependence of the TER effect is also observed. (Figure 5.3a) The OFF/ON ratio of the junction resistance for the FTJ devices with ~2.5 nm barrier, measured at 300 mV after the ferroelectric polarization switching at ±4 V, increases significantly to 10^5 (TER ratio ≈10^7%) and decreases with device area (see Figure 5.3b). This indicates that, with reducing device size, the ferroelectric polarization reversal becomes more effective and hence shows a promising trend for scalability. Reducing the size of the device also minimizes the pin holes and defects in addition to the better uniformity of the barrier layer. The TER value in our devices is among the highest reported TER values in HfO_2-based FTJs. [2,12] Recently, Wei *et al*. [12] have also reported the TER value as high as 10^6% with HZO-based FTJs. Such a large TER effect was attributed to the electric field control of the oxygen vacancy concentration at the HZO/LSMO interface. Moreover, besides interfacial engineering, the activation of Fowler–Northeim tunneling at higher bias and thermionic emission at higher barrier thicknesses cannot be ignored. [11,13] The large TER values with thicker barriers might involve these modes of transport in addition to the direct tunneling but at the cost of increasing RA values. With increasing the barrier thickness from ≈1 to ≈2.5 nm, we see nearly three orders of magnitude enhancement in the RA values of our FTJs (see inset of Figure 5.3c).

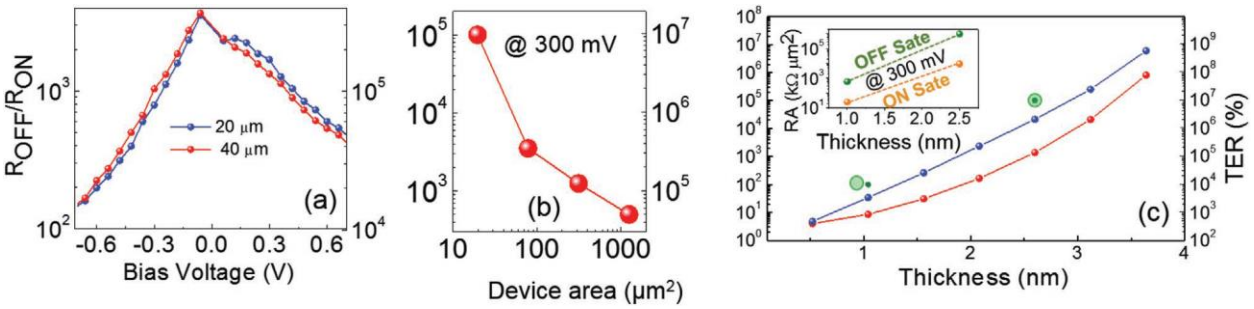

Figure 5.3. TER versus device scale. (a) OFF/ON ratio (TER%) of an FTJ with ≈2.5 nm HZO barrier as a function of reading voltage for the circular devices with diameters of 20 and 40 μm. (b) OFF/ON ratio (TER%) of the tunnel devices with ≈2.5 nm tunnel barrier as a function of the junction area. (c) Calculated OFF/ON ratio (TER%) without (red) and with (blue) n-type semiconductor interface between HZO and LSMO layers, of the tunnel device with varying ferroelectric barrier thickness, using the tight-binding model. The Schottky barrier results in an increase of the electric resistance for the OFF state leading to a higher TER ratio. Experimental data (green data points) follows a theoretically predicted trend. The inset shows the RA values for the OFF and ON states of the FTJ devices increase by 2–3 orders of magnitude with changing the barrier thickness from ≈1 to ≈2.5 nm. Solid and dotted lines are guides to the eye.

Various physical mechanisms at the interfaces between the HZO and electrodes could potentially play roles for such large values of the OFF/ON ratio in our HZO-based FTJs. The presence of oxygen vacancies at the interfaces of metal and HZO layers has been reported and thereby the possibility of the modification of the interfacial layer cannot be ignored.[14] Thus if we assume the existence of a thin n-type semiconductor region at the interface between HZO and LSMO, the tight binding model predicts an enhancement of the OFF/ON ratio of junction resistance (Figure 5.3c) close to the experimental values. The details are shown in Figure 5.4. We assume that the thickness of this semiconductor region is a single atomic monolayer, and we model this material in the same way as proposed in the reference.[15] In particular, we align the bottom of its conduction band with the Fermi level for the case of the paraelectric barrier. However, since HZO is ferroelectric, electron accumulation/depletion is formed within the semiconductor region depending on the direction of the ferroelectric polarization. For instance, when the ferroelectric polarization is pointing away from the semiconductor region, electron depletion leads to a Schottky barrier resulting in additional enhancement of the electric resistance (OFF state). In contrast, electron accumulation is formed when the polarization is pointing towards the semiconductor region and overall resistance is relatively small (ON state).

Enhancement of the TER effect due to the presence of non-polar interlayer at the barrier/electrode interface in HZO-based tunnel junctions has recently been theoretically as well as experimentally realized. [16,17]

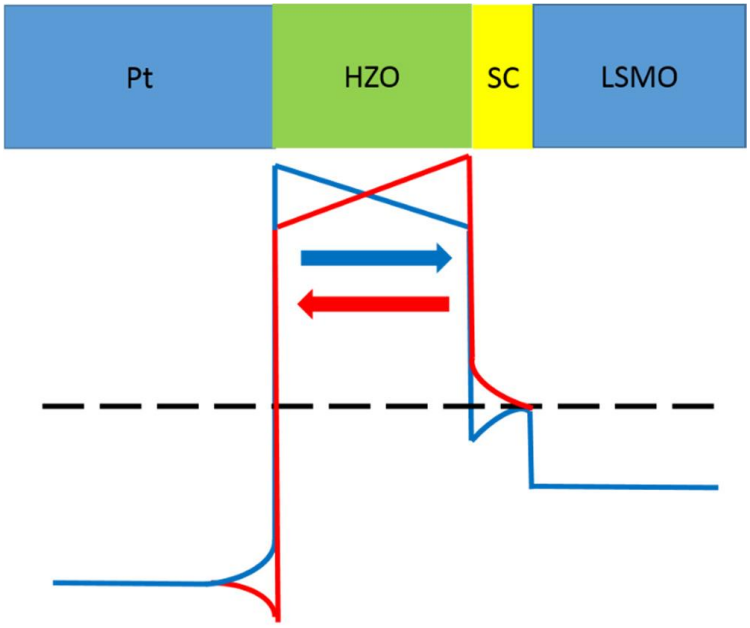

Figure 5.4. Schematic of the potential profile of Pt/HZO/LSMO ferroelectric tunnel junctions with an ultrathin semiconductor region at the HZO/LSMO interface for the two opposite directions of ferroelectric polarization.

In summary, we have demonstrated large TER effects in ultrathin HZO-based FTJs with significantly lower RA products. The TER ratio increases exponentially with decreasing the junction area. We have observed an OFF/ON junction resistance ratio as high as 10^5 with the

devices of 5 μm diameter. The TER effects can be observed even when the thickness of HZO films is reduced to ≈1 nm with an OFF/ON junction resistance ratio of ≈30 and the ON-state RA product of ≈25 kΩ μm2 at 300 mV. These results are promising in terms of scalability, better SNR, and OFF/ON junction resistance ratio, which has so far rarely been achieved in HfO_2-based FTJs, and therefore show the potential for high-density nonvolatile memory applications.

5.2 Scaling of ferroelectric HZO thin films

The scale-free nature of ferroelectric hafnia has been a subject of discussion for quite some time, with numerous studies [18-21] documenting the existence of ultra-thin ferroelectric hafnia films. From a theoretical perspective, HJ Lee *et al.* [22] have shown that hafnia's flat phonon band is the key to its scale-free property. This feature enables each unit cell to switch independently, with a consistent energy barrier for domain wall hopping across each cell, contributing to hafnia's high coercive field.

Past experimental research, however, predominantly concentrated on scaling the film thickness rather than its in-plane dimensions. In practical applications, the lateral size is vital for energy efficiency and information density. Therefore, we embarked on lateral scaling experiments using the LSMO/HZO/LSMO stack on STO/Si substrates, in collaboration with Western Digital. At Western Digital, the bare films were patterned and subjected to e-beam etching to create the small capacitors illustrated in Figure 5.5, with diameters ranging from 50nm to 5um. Due to the limitations of our probe station, which cannot handle capacitors smaller than 5um, we evaluated all switching behaviors using Piezoresponse Force Microscopy (PFM).

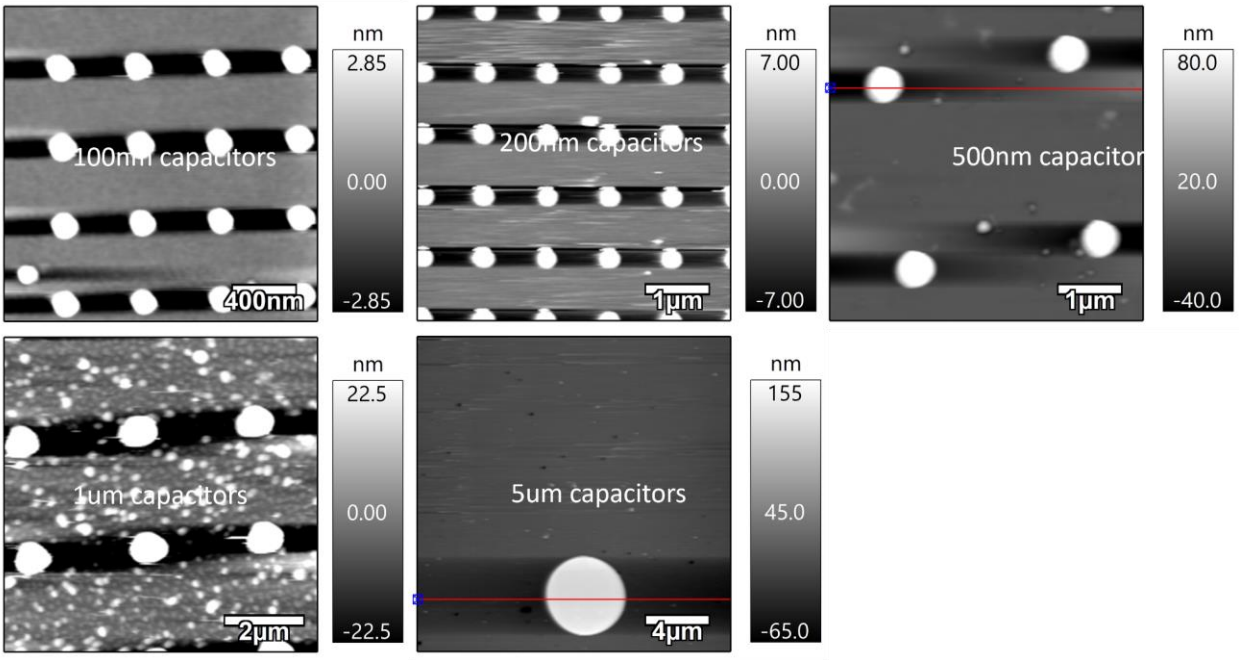

Figure 5.5. E-beam patterned Pt/LSMO/HZO/LSMO capacitors, captured using AFM.

The piezoelectric response of capacitors of various sizes is summarized in Figure 5.6a, with their respective switching fields presented in Figure 5.6b. The results indicate no significant difference in switching behaviors across capacitors of different sizes. Remarkably, the HZO layer functions efficiently in devices as small as 50nm in width and 10nm in thickness. This finding is encouraging for the future development of Ferroelectric Tunnel Junction (FTJ) devices smaller than 100nm using HZO. The observed switching field is approximately ~MV/cm, aligning with both previous experimental findings in different electrode/substrate material systems [23, 24] and theoretical assertions suggesting the high coercive field is an inherent characteristic of HZO. [22] The pronounced ferroelectricity and elevated switching field in films thinner than or equal to 5 nm, possibly attributable to the combined effects of depolarization field and the presence of an interfacial dead layer, imply promising retention capabilities for use in non-volatile memory devices.

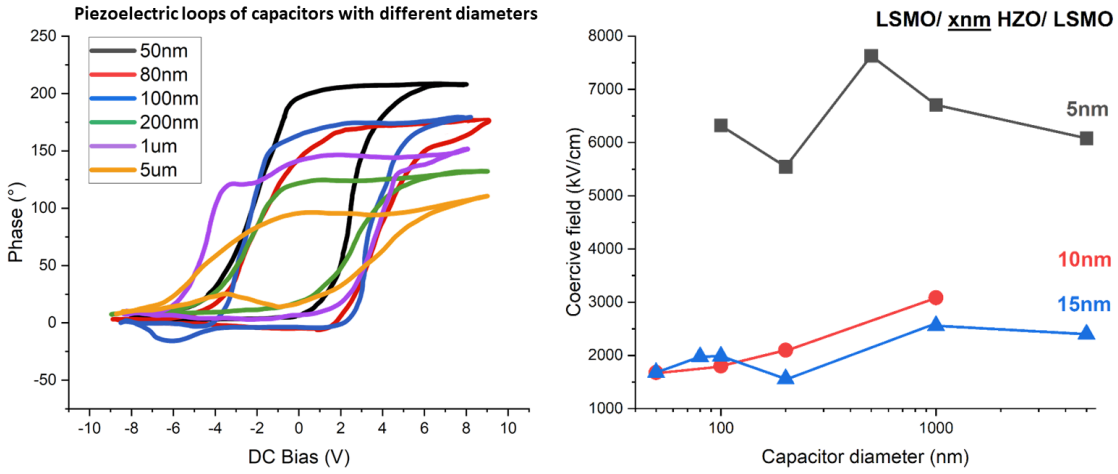

Figure 5.6. (a) Piezoelectric loops of LSMO/HZO/LSMO capacitors with 10nm HZO thickness and diameters from 50nm to 5um. (b) Coercive field extracted from the piezoelectric loops OF LSMO/HZO/LSMO devices with various diameters and HZO thicknesses.

References:

[1] P. Maksymovych, S. Jesse, P. Yu, R. Ramesh, A. P. Baddorf, S. V. Kalininl, Science 2009, 324, 1421.

[2] Z. Wen, D. Wu, Adv. Mater. 2019, 7, 1904123.

[3] R. Guo, W. Lin, X. Yan, T. Venkatesan, J. Chen, Appl. Phys. Rev. 2020, 7, 011304.

[4] Z. Chen, Z. Chen, C. Y. Kuo, Y. Tang, L. R. Dedon, Q. Li, L. Zhang, C. Klewe, Y. L. Huang, B. Prasad, A. Farhan, M. Yang, J. D. Clarkson, S. Das, S. Manipatruni, A. Tanaka, P. Shafer, E. Arenholz, A. Scholl, Y. H. Chu, Z. Q. Qiu, Z. Hu, L. H. Tjeng, R. Ramesh, L. W. Wang, L. W. Martin, Nat. Commun. 2018, 9, 3764.

[5] F. Ambriz-Vargas, G. Kolhatkar, R. Thomas, R. Nouar, A. Sarkissian, C. Gomez-Yáñez, M. A. Gauthier, A. Ruediger, Appl. Phys. Lett. 2017, 110, 093106.

[6] X. Tian, A. Toriumi, Proc. EDTM, IEEE, Piscataway, NJ 2017, p. 63.

[7] Y. Wei, S. Matzen, T. Maroutian, G. Agnus, M. Salverda, P. Nukala, Q. Chen, J. Ye, P. Lecoeur, B. Noheda, Phys. Rev. Appl. 2019, 12, 031001.

[8] F. Ambriz-Vargas, G. Kolhatkar, M. Broyer, A. Hadj-Youssef, R. Nouar, A. Sarkissian, R. Thomas, C. Gomez-Yáñez, M. A. Gauthier, A. Ruediger, ACS Appl. Mater. Interfaces 2017, 9, 13262.

[9] M. H. Park, Y. H. Lee, T. Mikolajick, U. Schroeder, C. S. Hwang, MRS Commun. 2018, 8, 795.

[10] S. Starschich, T. Schenk, U. Schroeder, U. Boettger, Appl. Phys. Lett. 2017, 110, 182905.

[11] V. Garcia, M. Bibes, Nat. Commun. 2014, 5, 4289.

[12] Y. Wei, S. Matzen, C. P. Quinteros, T. Maroutian, G. Agnus, P. Lecoeur, B. Noheda, npj Quantum Mater. 2019, 4, 62.

[13] H. Y. Yoong, H. Wu, J. Zhao, H. Wang, R. Guo, J. Xiao, B. Zhang, P. Yang, S. J. Pennycook, N. Deng, X. Yan, J. Chen, Adv. Funct. Mater. 2018, 28, 1806037.

[14] M. Mineshima, IEEE Trans. Electron Devices 2020, 67, 515.

[15] Velev, J. P., Burton, J. D., Zhuravlev, M. Y., & Tsymbal, E. Y. (2016). Predictive modelling of ferroelectric tunnel junctions. npj Computational Materials, 2(1), 1-13.

[16] C. Richter, T. Schenk, M. H. Park, F. A. Tscharntke, E. D. Grimley, J. M. LeBeau, C. Zhou, C. M. Fancher, J. L. Jones, T. Mikolajick, U. Schroeder, Adv. Electron. Mater. 2017, 3, 1700131.

[17] Y. Goh, S. Jeon, Appl. Phys. Lett. 2018, 113, 052905.

[18] Cheema, S. S., Kwon, D., Shanker, N., Dos Reis, R., Hsu, S. L., Xiao, J., ... & Salahuddin, S. (2020). Enhanced ferroelectricity in ultrathin films grown directly on silicon. Nature, 580(7804), 478-482.

[19] Yap, W. C., Jiang, H., Liu, J., Xia, Q., & Zhu, W. (2017). Ferroelectric transistors with monolayer molybdenum disulfide and ultra-thin aluminum-doped hafnium oxide. Applied Physics Letters, 111(1).

[20] Yuan, Z. L., Sun, Y., Wang, D., Chen, K. Q., & Tang, L. M. (2021). A review of ultra-thin ferroelectric films. Journal of Physics: Condensed Matter, 33(40), 403003.

[21] Goh, Y., Hwang, J., Lee, Y., Kim, M., & Jeon, S. (2020). Ultra-thin $Hf_{0.5}Zr_{0.5}O_2$ thin-film-based ferroelectric tunnel junction via stress induced crystallization. Applied Physics Letters, 117(24).

[22] Lee, H. J., Lee, M., Lee, K., Jo, J., Yang, H., Kim, Y., ... & Lee, J. H. (2020). Scale-free ferroelectricity induced by flat phonon bands in HfO_2. Science, 369(6509), 1343-1347.

[23] U. Schroeder, C. S. Hwang, H. Funakubo, Ferroelectricity in doped hafnium oxide: materials, properties and devices, Woodhead Publishing, 2019.

[24] Y. Wei, P. Nukala, M. Salverda, S. Matzen, H. J. Zhao, J. Momand, A. S. Everhardt, G. Agnus, G. R. Blake, P. Lecoeur, B. J. Kooi, J. Iniguez, B. Dkhil, B. Noheda, Nat Mater 2018, 17, 1095.

Chapter 6

Summary of Findings and Directions for Future Research

In this thesis, our primary focus is on thin film ferroelectric hafnia, spanning from the deposition process to the study of switching and fatigue behavior. We have employed two main material systems, one for fundamental investigations and the other for exploring practical applications.

Our comprehensive examination has delved into the stabilization mechanisms, phase transitions, and potential applications of ferroelectric thin films based on HZO (Hafnium Zirconium Oxide). These findings have made significant contributions to the advancement of ferroelectric materials, particularly in the context of modern technological applications, such as memory storage and electronic devices.

Chapter 3: This chapter extensively explored a highly epitaxial HZO system employing pyrochlore electrodes. It emphasized the pivotal role of epitaxial strain and surface energy in stabilizing HZO's polar orthorhombic phase. The study unveiled that the relaxation of misfit strain with increasing film thickness significantly impacts the phase transition from polar-orthorhombic to non-polar-monoclinic. Furthermore, the investigation demonstrated that the switching field of a pure epitaxial HZO thin film remains notably high at approximately ~MV/cm, indicating the intrinsic ferroelectric property of hafnia. Additionally, the research offered insights into the diffuse nature of the interface between these phases within HZO, suggesting a phase transition of the order-disorder type. This chapter also introduced a single-crystal ferroelectric epitaxial HZO material system, setting the stage for future exploration of the intrinsic properties of ferroelectric hafnia.

Chapter 4: This chapter presented novel insights into the stabilization of the o-phase through oxygen intercalation and defect chemistry. The fatigue behavior was investigated along with microstructure characterization, uncovering phase transformations during field cycling. These transformations highlight the critical role of oxygen vacancies in ferroelectric hafnia. The chapter sets a foundational understanding for advanced defect chemistry engineering, aimed at augmenting the stability of ferroelectric phases in HZO, thereby improving endurance behavior.

Chapter 5: The chapter observed significant Tunnel Electro-Resistance effects in ultra-thin HZO-based Ferroelectric Tunnel Junctions. Scale-free ferroelectric switching was also demonstrated experimentally, confirming its consistent switching performance across a wide range of lateral scales from 50 nm to 5 μm. These results show great promise for developing high-density, energy-efficient, nonvolatile memory applications.

Future Research Directions:

Enhancement of Pyrochlore Electrodes: Future research should focus on improving the deposition quality of pyrochlore electrodes, particularly addressing the interface roughness between pyrochlore and hafnia. Enhancements in this area could facilitate more electrical measurements on the highly epitaxial ferroelectric HZO system.

Detailed Phase Transition Analysis: A more in-depth examination of phase transition dynamics, especially during fatigue behavior, is necessary. In-situ structural measurements could provide further evidence of phase transformations and track the migration of oxygen vacancies. Understanding these dynamics could refine the material's performance and stability.

Advanced Defect Chemistry Research: Continued research in defect chemistry, specifically targeting the manipulation of oxygen vacancy trapping, is needed. This could lead to increased stability and improved performance of ferroelectric materials.

Optimization of FTJs for Memory Storage: Ongoing development and optimization of HZO-based FTJs for memory storage applications are crucial. Efforts should be directed towards enhancing scalability, efficiency, and junction resistance ratios. Translating these academic findings into commercial technologies also presents a significant challenge. Future research should therefore focus on addressing scalability and manufacturability issues to integrate these advanced materials into mainstream technology.

In summary, the research conducted in this thesis significantly enhances the understanding of HZO-based ferroelectric materials and lays a solid foundation for future investigations aimed at fully harnessing the potential of HZO-based technologies in the fields of advanced computing and memory systems.

Appendix A

PLD conditions for epitaxial ferroelectric HZO thin film deposition

Film	*Substrate*	*Fluence (J/cm^2)*	*Laser Frequency (Hz)*	*O_2 pressure (mTorr)*	*Cooldown Pressure*	*Temperature (°C)*	*Thickness (nm)*	*Growth rate (pulses/nm)*
HZO	YSZ (001)	1.4	2	100	Atm	600	5-30	100
PIO	YSZ (001)	1.7	1	100	Atm	600	30	10
SRO	YSZ (001)	1.4	2	100	Atm	600	30	34
HZO	STO (001)	1.1	1	100	500mTorr	700	1-10	120
LSMO	STO (001)	1.5	10	200	500mTorr	700	60	60
HZO	STO/Si(001)	1.1	2	100	Flexible	600	10	138
LSMO	STO/Si(001)	1.1	4	100	Flexible	600	45	80